FRESH GROUNDWATER LENS DEVELOPMENT IN SMALL ISLANDS UNDER A CHANGING CLIMATE

A Dissertation
Presented to
The Academic Faculty

by

Yuening Tang

In Partial Fulfillment
of the Requirements for the Degree
Doctor of Philosophy in the
School of Civil and Environmental Engineering

Georgia Institute of Technology
May 2021

FRESH GROUNDWATER LENS DEVELOPMENT IN SMALL ISLANDS UNDER A CHANGING CLIMATE

Approved by:

Dr. Jian Luo, Advisor
School of Civil and Environmental Engineering
Georgia Institute of Technology

Dr. Yi Deng
School of Earth and Atmospheric Science
Georgia Institute of Technology

Dr. Jingfeng Wang
School of Civil and Environmental Engineering
Georgia Institute of Technology

Dr. Chunhui Lu
College of Water Conservancy and Hydropower Engineering
Hohai University

Dr. Kevin A. Haas
School of Civil and Environmental Engineering
Georgia Institute of Technology

Date Approved: May 2021

ACKNOWLEDGEMENTS

I would like to express my deepest appreciation to my supervisor Dr. Jian Luo for his invaluable guidance and continuous support during my Ph.D. study. It's extremely lucky and a great honor for me to have such a kind and knowledgeable supervisor in my Ph.D. career. His endless pursuit of knowledge and the patient yet serious attitude to student will enlighten my future career and be my lifetime fortune. My gratitude to Dr. Jian Luo would never come to an end.

I would also like to thank my committee members: Dr. Jingfeng Wang, Dr. Kevin A. Haas, Dr. Yi Deng and Dr. Chunhui Lu for their constructive and insightful suggestions which help me to complete the thesis. I gratefully acknowledge the partial financial support from China Scholarship Council.

My gratitude also goes to the colleagues in our office, Yue Zhao, Saubhagya Singh Rathore, Tongtong Xu for their help and advice to my research, and the friendship in my daily life.

Finally, I would like to express sincerest gratitude to my parents: Xiaozhi Tang and Zhilan Tian for their unconditional support and love. They are always my strongest backing, which makes me fearless in regard of hardness. The sincerest gratitude extends to my boyfriend Yunlong Wang for his encouragement and company throughout my entire Ph. D career.

TABLE OF CONTENTS

LIST OF TABLES

LIST OF FIGURES

LIST OF SYMBOLS AND ABBREVIATIONS

ρ_s [M/L^3]	density of seawater
ρ_f [M/L^3]	density of freshwater
ρ [M/L^3]	density of fluid
δ[-]	$(\rho_s - \rho_f)/\rho_f$
W [L]	half width of the island
H [L]	the thickness of lens
K [L/T]	hydraulic conductivity
ω [L/T]	recharge rate
h [L]	water table head
ε [-]	porosity
t [T]	time
$\bar{H}$ [L]	average of the areal distribution of the depth
A[L^2]	volume
ζ[-]	damping ratio
ω_n[-]	undamped natural frequency
L[L]	width of the island
L_c[-]	correlation length
σ_ω^2[-]	variance of recharge
D[-]	the distance between two points
d[L]	the depth of partially penetrating well
q[L^2/T]	pumping rate
W_s[L]	inundated coastal line

L_s[L]	the distance that sea water enters the island
Q_x, Q_z[L/T]	Darcy's velocities *x*-direction and *z*-direction
h_{out}, h_{in}[[L]	specified-head at the left side and the right side
Q[L/T]	specified-flux
W_T [L]	thickness of the sand tank
k [L^2]	permeability
μ [M/L/T]	dynamic viscosity
g [L/T^2]	acceleration of gravity
p [$M/L/T^2$]	pressure
c [M/L^3]	concentration
c_s, c_0 [M/L^3]	normalized concentrations of seawater and freshwater
p_s, p_0 [$M/L/T^2$]	normalized pressures of seawater and freshwater
θ_s[-]	fluid's volume fraction
D_L [L^2/T]	dispersion coefficient

SUMMARY

Groundwater is stored in surficial coastal aquifers in small islands in the form of freshwater lens floating on the seawater due to density difference. In many small islands, groundwater lenses are important freshwater supplies to island inhabitants due to the lack of sufficient surface water reservoirs. The shape and volume of a groundwater lens is sensitive to changing environmental and climate conditions, including recharge from precipitation, sea-level rise, and anthropogenic activities such as groundwater withdrawal. This thesis research implements a systematic research plan to investigate the dynamic spatiotemporal behavior of a groundwater lens under a changing climate and anthropogenic activities. A series of analytical solutions and numerical models have been developed to describe the transient change of the freshwater-seawater interface profile that delineates the geometry of a groundwater lens in a small strip island. Laboratory visualization experiments were also designed and conducted to validate the solutions, models and scientific findings. Fundamental scientific questions addressed include (1) how the lens interface changes in response to spatially and temporally variable recharge rates in a changing climate; (2) how high the groundwater withdrawal rate can be for a sustainable groundwater management in small islands with the prevention of saltwater upconing; and (3) how short-term and long-term sea level changes will impact the shape and volume of a groundwater lens. The developed modeling tools and findings have the potential to render significant social and economic impact for groundwater resources management in small islands.

CHAPTER 1. INTRODUCTION

1.1 Freshwater Lens in Small Islands

In the past decades, more frequent climate-change related, changing environmental conditions have emerged, potentially affecting many vulnerable human groups. Among these groups, island inhabitants are of concern in the present study because of their vulnerability to lack of freshwater resources (Campbell and Barnett, 2010; Pelling and Uitto, 2001). There are over 100,000 islands on the oceans of the world and around 500 million people living on them (Dose et al., 2014). Constantly growing population combined with rapid commercial and tourism development demands high freshwater supply. However, freshwater is scarce on many small islands because they are surrounded by seawater and rarely have natural surface water reservoirs, i.e., lakes and rivers (Dose et al., 2014; Stoeckl et al., 2015). Groundwater in surficial aquifers, stored in the form of freshwater lenses floating on the seawater due to density differences, is often the primary source of freshwater supply for inhabitants on small islands (Post et al., 2019). Figure 1 shows the schematic plot of a symmetric lens under uniform recharge in an aquifer with homogeneous hydrogeological properties, i.e., hydraulic conductivity.

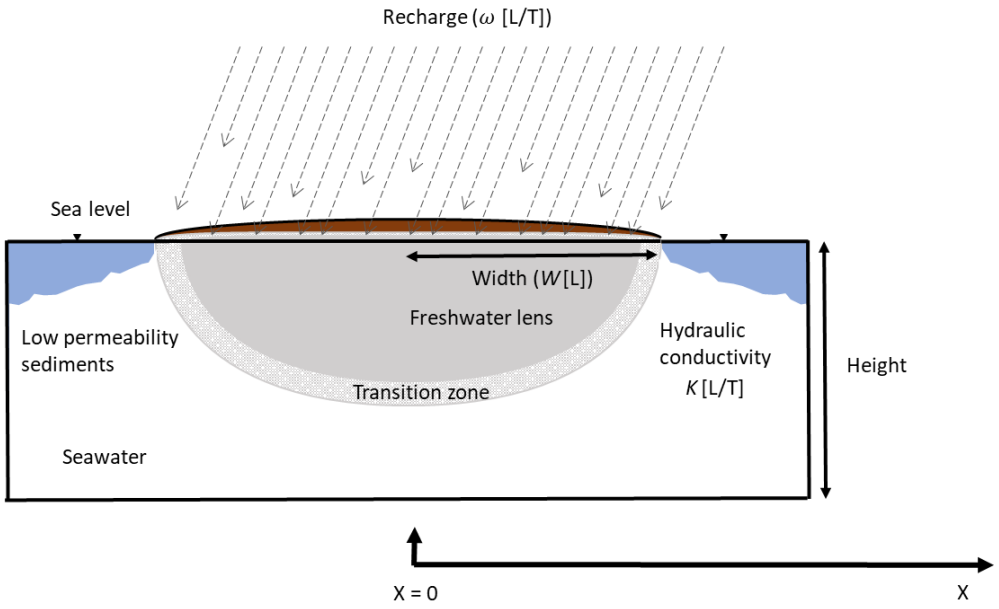

Figure 1. Cross section of a symmetric freshwater lens structure in small strip islands.

The shape and volume of groundwater lenses can be influenced by numerous factors including hydrologic conditions of aquifer formations, climate change (e.g., storm surges and precipitation), sea-level rise, human activities and others (Alsumaiei and Bailey, 2018; Chui and Terry, 2012; Chui and Terry, 2015; Post et al., 2019; Sulzbacher et al., 2012; Terry and Falkland, 2010):

(1) Among the factors mentioned above, variable climate change, particularly the fluctuations in rainfall precipitation, is considered to be a significant factor because recharge of groundwater lenses may largely rely on infiltration from precipitation on small islands. Climate change of specific weather patterns may cause highly variable rainfall precipitation. For example, on Pacific Ocean, precipitation is strongly influenced by El Niño–Southern Oscillation (ENSO) which may lead to long-term drought events (Werner et al., 2017). During extended drought, the

replenishment from infiltration is not adequate and freshwater lenses become thinner. A depleted lens may need years to recover to the original volume (Chui and Terry, 2013).

(2) Freshwater lens suffers from the sea-level rise and extreme climate events such as storm surge and land-surface inundation (LSI). LSI can lead to a considerable seawater intrusion into costal aquifers through downward convection. Consequently, coastal erosion reduces the island size and thereby reducing the volume of freshwater lens contained within the body of the island. Gradually rising sea levels due to global warming over the past decades has become a great threat to small islands. The sea level rise is expected to be 0.5 to 1.8m (Ketabchi et al. 2014), which will result in a significant LSI. Previous research on the effect of sea-level rise assumed either a pure sea level rise without inundation or a severe sea level rise with an entire inundation of the whole coastal line. In the real world, both are unrealistic. In fact, the existence of low-lying depression (such as creek, stream) along the coastal line leads to a preferential path of seawater intrusion into the island.

(3) Another major concern to groundwater resources on small islands is anthropogenic activities such as over-exploitation. Freshwater lens is floating above the seawater. A transition zone exists between the freshwater and seawater, and can be approximated as a sharp interface when it is relatively thin compared with the aquifer thickness (Muskat, 1938). The equilibrium between freshwater and seawater can be disturbed and broken when excessive freshwater is withdrawn from water supply wells, causing upward movement of the interface toward the pumping

well, commonly referred as upconing (Asghar et al., 2002; Bear, 2012). Thus, the key to sustainable groundwater resources management on small islands is the determination of optimal pumping rate to prevent seawater upconing into supply wells.

1.2 Research Motivation

Better understanding of the behavior of such coastal groundwater lenses is necessary for designing sustainable groundwater use strategies to meet the increasing water needs of growing population and economic development on islands. However, many important questions about groundwater lens in small islands remain unclear:

(1) Previous research on the impact of time-dependent recharge on groundwater lens either assumes steady-state recharge or relies on numerical modeling. The former is more efficient and faster but ignores fluctuations of recharge in the real world. The latter is easy to handle transient recharge but hard to draw general conclusions because they are often computationally expensive and site-specific. How the lens interface changes in response to temporally variable recharge rates in a changing climate is not answered.

(2) Limited research has considered spatially variable recharge rates for modeling the groundwater lens development. Vacher (1988) developed an analytical solution to describe the steady state, asymmetric lens profile caused by a simple spatial recharge pattern, in which there are only two different recharge rates for the left and right half of a strip island. The results showed that the lens shape became skewed toward the larger recharge rate side. Comte et al. (2010) simulated a

combined model of geoelectrical data and water head to investigate groundwater lens recharge. Their model showed that on densely vegetated areas, evapotranspiration exceeds replenishing of lens, leading to occurrence of seawater intrusion. To the best of our knowledge, there is no study to explore how spatially variable recharge in general affects the freshwater lens profile.

(3) Previous studies can not be directly applied to upconing problem in small islands because there are two main differences. Firstly, a typical assumption in previous studies is that the initial interface is horizontally infinite or semi-infinite, which may only be valid for describing local upconing behavior on top of a large-scale seawater intrusion wedge or lens interface in large islands. In our study, the sea boundary has significant impact to shape the lens interface. The interface moves towards the well under pumping, forming a ω shape in small islands, as shown in figure 2. Secondly, the water flux balance is different. Previous studies assumed horizontal inflow to supply the pumping well, while in islands it is the vertical recharge. To the best of our knowledge, even for the simplest case with a single pumping well, the simple but important question is still unanswered. That is, how high can the groundwater withdrawal rate be for a sustainable groundwater management in small islands with the prevention of saltwater upconing;

(4) The impact of sea-level changes was investigated by steady-state assumptions or surface inundation. It remains unknown how short-term and long-term sea level changes will impact the shape and volume of a groundwater lens though preferential flooding paths.

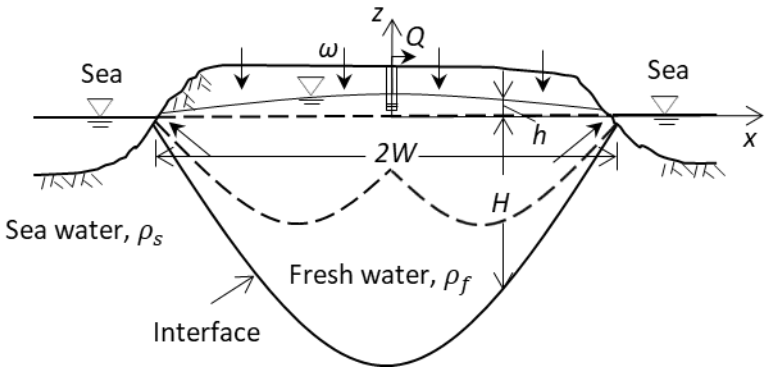

Figure 2. Two-dimensional conceptual model for the groundwater lens under pumping at the center.

In summary, there are significant knowledge gaps regarding the impact of climate-related hydrogeologic conditions and anthropogenic activities on the development of groundwater lenses in small islands. Also, there lacks effective mathematical modeling tools to generalize previous site-specific findings and to improve the general understanding of the spatiotemporal behavior of the lens interface under a changing climate in small islands.

1.3 Research Objective

Objectives of the thesis research include:

(1) We aim to develop an efficient, approximate analytical solution to describe the transient behavior of the seawater-freshwater interface and groundwater lens volume. The analytical solution can be used to efficiently and systematically explore the transient behavior of interface shape and volume of groundwater lenses for time-dependent, fluctuating recharge and to effectively improve the understanding of the effects of inherent controlling mechanisms and hydrogeologic conditions to help predict groundwater resources on small islands under varying

climate-change related environmental conditions. Moreover, we plan to approximate the solution by an underdamped two-order system, which can act as a low-pass filter and provide general insights and an efficient tool to investigate the effects of the transient recharge on groundwater lenses.

(2) We aim to derive an analytical solution of groundwater lens profiles that can account for the impact of both time-dependent and spatially variable recharge rates. This solution can be applied to describe completely spatially heterogeneous recharge patterns. Both numerical and laboratory models are implemented to validate the analytical solutions. The derived solution will be used to analyze how spatial distribution of recharge affects the lens shape and volume.

(3) We aim to derive an analytical solution to describe the interface upconing in a small strip island and to determine the critical groundwater withdrawal rate in a recharging groundwater lens.

(4) We aim to develop a numerical model with low-lying depressions to study how single path or multiple flooding paths of sea-level rise under varying sea level such as short-term tidal activities and long-term sea-level rise affects the lens shape and volume in small islands.

In summary, the thesis research is to conduct analytical, numerical and stochastic modeling integrated with laboratory studies and field data analysis to investigate the impacts of multiple factors, including recharge variations, sea level rise, and pumping, on the spatiotemporal behavior of fresh groundwater lens, and to provide insights, tools and methods for sustainable groundwater management in small islands. For the laboratory work, we will cooperate with Dr. Lu's research group at Hohai University. We are responsible

for designing and providing specific experimental scenarios and conditions for Hohai University to implement the experiments.

1.4 Organization of This Thesis

This thesis consists of 10 chapters. Chapter 1 gives a brief introduction to the problem, motivations and the objectives of our study. Chapter 2 gives a comprehensive literature review of the research. Chapter 3-Chapter 5 provides the theoretical analysis of impact of time-dependent recharge on the freshwater lens, the impact of spatially variable recharge on the freshwater lens and critical pumping rate for sustainable usage of freshwater lens, respectively. Chapter 6 and Chapter 7 provide the laboratory validation and numerical validation of theoretical analysis from Chapter 3 to Chapter 5, respectively. Chapter 8 discusses the influences of sea-level rise on the freshwater lens. A field case investigation is given in Chapter 9. Chapter 10 summarizes conclusions and future work.

CHAPTER 2. LITERATURE REVIEW

2.1 Freshwater Lens and Impact Factors

Residential and commercial activities on small islands are often constrained by the growing stress and needs of freshwater resources due to the lack of natural reservoirs. Such situations have exacerbated in the past decades due to climate change and more frequent extreme weather events. Groundwater in the surficial coastal aquifers provides valuable and sometimes primary freshwater supplies as a reliable source more susceptible to climate change. Due to density differences, fresh groundwater usually floats as a lens above the seawater in the island aquifers. Under natural conditions, the shape of lens is often distorted and asymmetric due to heterogeneity of recharge and aquifer formation properties. Freshwater and seawater are miscible, and therefore a transition zone forms. The density varies from seawater to freshwater across the transition zone. The thickness of the transition zone is typically determined by the magnitude of dispersivity. The occurrence of seawater intrusion can also enhance the transition zone (Werner et al., 2017). In many cases, the transition zone can be approximated as a sharp interface assumption. The assumption is valid when the thickness of the transition zone is small compared with the thickness of the lens. Based on the sharp interface assumption, Fetter (1972) provided a classical equation to describe the steady-state lens profile in strip islands with homogeneous hydrogeological conditions:

$$H = \delta \sqrt{\frac{\delta\omega(W^2 - x^2)}{K(1 + \delta)}} \tag{1}$$

where $\delta = (\rho_s - \rho_f)/\rho_f$. ρ_s [M/L^3] is density of seawater; ρ_f [M/L^3] is density of freshwater; H [L] is the thickness of lens, typically defined as the vertical distance from the sea level to the interface. W [L] is the half width of the island. K [L/T] is hydraulic conductivity. The equation along with its circular island solution is frequently cited by many researchers and served as the most fundamental analytical equation, providing useful insights to understand the impact of hydrogeologic conditions on the steady-state lens profile. For example, Eq. (1) indicates that the thickness grows linearly with the squared root of the recharge rate and a high hydraulic conductivity yields a smaller lens given the same recharge. In addition, based on this classical solution, many other solutions for more complex conditions were derived, such as the solutions to describe a vertically or horizontally layered heterogeneous aquifers and the effect of sea-level rise (Lu et al., 2019; Ketabchi et al. 2014).

As shown in Figure 1 and Eq. (1), groundwater lenses can be influenced by recharge, hydrological conditions of aquifer formations (e.g., hydraulic conductivity and island width), and sea-level rise. Among these factors, recharge is critical for the development of a freshwater lens. Ketabchi et al. (2014) conducted sensitivity analysis of different factors and found the profound impact of recharge on the steady-state volume of groundwater lenses based on a steady-state analytical solution for two-layered small island aquifers. Bailey et al. (2009) showed that the maximum steady-state lens thickness grows exponentially with the increasing recharge. Temporal and spatial recharge distribution depends on precipitation and evapotranspiration. Precipitation varies in different seasons and the rainfall season pattern also differs between islands. Drought events lasting for months or years can tremendously reduce the thickness and volume of lens. The amount of

evapotranspiration is also greatly related to seasons. Summer's evapotranspiration is largely higher than winter'. On St. George island (Schneider and Kruse, 2006), recharge is highest during winter due to high evapotranspiration in summer although summer has the highest rainfall.

According to Eq. (1), hydraulic conductivity and island width have equally inverse effect on the extent of lens. Islands with smaller hydraulic conductivities and wider extent tend to have a larger lens volume. Hydraulic conductivity is inherently heterogeneously distributed in natural aquifers. Holocene aquifer is of much lower hydraulic conductivity by one to two magnitude than Pleistocene sediments (Werner et al., 2017). A reef flat plate is often present in atoll island, acting as a confining layer for freshwater lens (Ketabchi et al. 2014). Hydraulic conductivity heterogeneity has key impact on freshwater lens shape. Lu et al. (2019) proposed a concept model that decreases the hydraulic conductivity of a slice along the shoreline to increase the freshwater lens volume. Ketabchi et al. (2014) studied the effect of a two-layer geologic formation on the lens and found the upper layer controls lens volume when base layer is of low hydraulic conductivity. According to Werner et al., (2017), high hydraulic conductivity of low aquifer tends to enhance the mixing zone because seawater is more likely to invade landward in such a condition.

Freshwater lens is vulnerable to sea-level rise, which can cause seawater intrusion (SWI). The extent of sea-level rise sourced SWI is from tens of meters to thousands of meters landward for head-controlled systems while flux-controlled aquifers are more resistant to sea-level rise (Werner and Simmons, 2009). Chui and Terry (2013) studied how islands of different sizes (400m, 600m, 800m) respond to a sea-level rise of 40cm and found smaller islands have significant less freshwater lens volume and more vulnerable to threat by sea-

level rise. Terry and Chui (2012) designed a small island with a topographic depression on the center area. In their model, sea-level rise of 10cm, 20cm and 40cm were simulated and a 40cm sea-level rise can induce a major threat, reducing the lens thickness to half. Masterson and Garabedian (2007) also pointed out that sea-level rise leads to a freshwater thickness decrease and net decline. One important factor to enhance the impact of the sea-level rise is the occurrence of LSI. Sea-level rise combining with LSI involves both vertical and horizontal movements of seawater. A pure sea-level rise mostly occurs for confined aquifers(Ataie-Ashtiani et al., 2013; FALKLAND and Custodio, 1991). But for unconfined aquifers, models with LSI are more applicable, especially in the typical low topography in small islands (Bricker and Hughes, 2007; Ketabchi et al., 2014; Werner et al., 2009).

Another major concern is human activities which are likely to alter the lens structure. Freshwater demand increases largely due to developing population and growing tourism recently on small islands. The development may be greatly variable in different regions within one island. On St. George (Schneider and Kruse, 2006), central area has heaviest development including road and bridge building therefore the infiltration alters. Pumping is one of the most threatened human activities to lens on small islands. Under pumping, seawater is rising towards the pumping well, forming an upconing shape. There exists a critical pumping rate that is the maximum rate to maintain equilibrium. That is, the cone apex can remain stable under the critical condition, but any increase in the pumping rate from the critical condition will lead to an unstable cone, driving saltwater into the pumping well. Correspondingly, critical upconing position or rising ratio can be defined as the rise of stable interface at the critical pumping rate normalized by the original spacing between the interface and the pumping well (Bower et al., 1999; Motz, 1992; Werner et al., 2009).

Over-exploitation of freshwater decreases the aquifer water head and thus leads to seawater intrusion (Abd-Elhamid and Javadi, 2011). Determining the critical pumping ratio is essential in freshwater management in small islands to prevent seawater pumped into wells and guarantee a sustainable usage of freshwater.

2.2 Mathematical Modeling

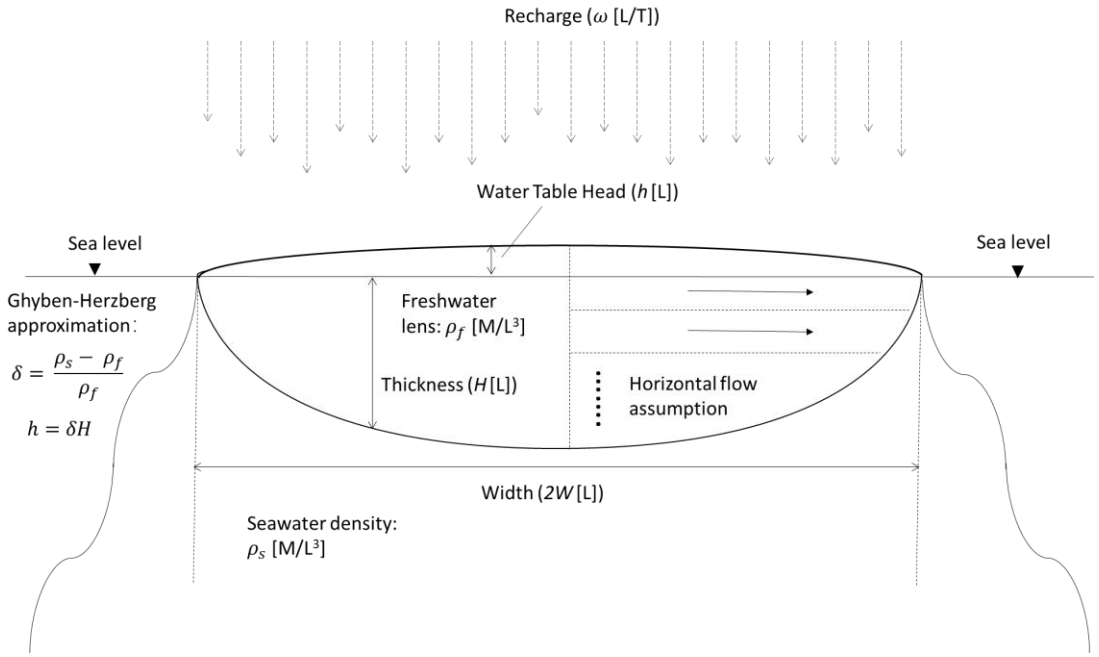

Figure 3. Sharp-interface based mathematical model of freshwater lens

There are typically two mathematical models available to simulate the groundwater lens in coastal aquifers. One is based on the sharp-interface assumption, which ignores the mixing of freshwater and seawater, and the other considers a mixing zone with variable-density flow and transport. Sharp-interface assumption is to consider seawater and freshwater is completely immiscible and can be separated by a sharp interface, as shown in figure 3. The thickness of groundwater lens, *H*, is defined as the distance from the interface to the sea

level. Water table, h, is defined as the distance from the water surface to the sea level. Seawater and freshwater are handled as two different domains and each single fluid can not transport through domain boundary (Bear, 2012; Reilly and Goodman, 1987). The sharp-interface assumption is considered reasonable to estimate lens shape and structure when the transition zone is thin compared with the whole aquifer thickness. The sharp-interface approximation may not describe the dispersive mixing between freshwater and seawater, but can provide important insights of the growth and decay of the groundwater lens and has been widely used to quantify seawater intrusion and saltwater upconing Ghyben-Herzberg approximation and horizontal flow assumption are often made along with sharp-interface assumption. Ghyben-Herzberg approximation is to determine the lens position and shape by assuming the thickness of lens is proportional to water table:

$$h = \delta H \tag{2}$$

Ghyben-Herzberg approximation itself is to assume a static equilibrium and pressure distribution (Bear, 2012). Here we use it as dynamic equilibrium and assume a horizontal flow in freshwater domain. Based on above assumptions, a series of analytical solutions have been derived to provide good approximation and very useful insights for understanding the behavior of groundwater lens development. Current analytical solutions are mainly to describe steady-state interface profile of the groundwater lens. Such analytical solutions were developed in homogeneous circular islands (Fetter Jr, 1972), strip islands (Vacher, 1988), and two-layered islands (Ketabchi et al., 2014) and two-vertically-sliced islands (Lu et al., 2019) for a given constant recharge rate. The analytical solution to describe transient development is rarely seen because it largely complexes the

computational and derivation process. Only Hantush (1968) provided a transient analytical solution for lens growth for a constant recharge in an infinite domain.

The analytical models charactering the effect of sea-level rise on freshwater lens are limited studied. Only Ketabchi et al., (2014) provided an analytical model derived from Fetter (1972) solution to describe the steady freshwater lens thickness and volume under sea-level rise. Analogous research focuses on freshwater-seawater interface along coastal aquifers. Strack (1976) applied the potential theory to solve three-dimensional coastal interface problems in different costal aquifers (i.e., confined, unconfined, semiconfined). His studies show that the sea-level rise has significant effect on costal aquifer if LSI occurs.

As for pumping from groundwater, analytical solutions have also been employed to investigate the interface movement and determine the critical pumping rate. Muskat (1938) first provided an approximate solution for steady flow to a pumping well above a freshwater-seawater interface, given the assumption that the interface moves only a small distance compared with the original spacing between the well and interface. He also assumed that the interface is impervious, and the rise of the interface does not change the potential distribution. Based on Muskat's model, Dagan and Bear (1968) derived an analytical solution for a time-dependent upconing interface using the method of small perturbation. Strack (1972) provided analytical solutions for the interface upconing under a drain by the method of conformal mappling and the hodograph. Zhang et al. (1996) provided an analytical solution for critical and supercritical withdrawal from a two-layer fluid through a line sink in porous media, which was extended to a partially bounded aquifer (Zhang et al., 2009). Dagan and Zeitoun (1998) derived an approximate analytical solution for the interface upconing in stratified aquifers of random conductivity. Bower et

al. (1999) obtained an analytical solution for determining the critical condition in an aquifer overlain by a leaky confining unit.

Another general mathematical model is numerical models which involves variable-density transport by solving following equations of fluid and transport of solution:

$$\frac{\partial \varepsilon \rho}{\partial t} + \nabla \cdot \rho u = 0 \tag{3}$$

$$\frac{\partial \theta_s c}{\partial t} + u \cdot \nabla c - \nabla \cdot \theta_s D_L \nabla c = 0 \tag{4}$$

where u [L/T] is Darcy velocity:

$$u = -\frac{k}{\mu}(\nabla p + \rho g \nabla D) \tag{5}$$

ρ [M/L^3] fluid density is linearly increasing with concentration:

$$\rho = \rho_0 + \frac{\rho_s - \rho_0}{c_s - c_0} c \tag{6}$$

ε [-] is porosity; t [T] is time; k [L^2] is permeability; μ [M/L/T] is dynamic viscosity; g [L/T^2] is acceleration of gravity; p [M/L/T^2] is pressure; c [M/L^3] is concentration; c_s [M/L^3] and c_0 [M/L^3] are the normalized concentrations of seawater and freshwater; p_s [M/L/T^2] and p_0 [M/L/T^2] are the normalized pressures of seawater and freshwater; θ_s[-] is fluid's volume fraction; D_L [L^2/T] is dispersion coefficient.

The most popular computer codes to solve above equations are SEAWAT and SUTRA, both developed by U.S. Geological Survey (Guo and Langevin, 2002; Voss and Provost,

2002). The major difference between numerical simulations and sharp-interface analytical solutions is the effects of hydrodynamic dispersion, which yields a variable-density transition zone between freshwater and seawater (Rubin and Pinder, 1977; Wirojanagud and Charbeneau, 1985; Reilly and Goodman, 1987; Ma et al., 1997; Zhou et al., 2005). Numerical models have less limitations than analytical approach regarding geometry of islands, boundary condition and hydrogeologic heterogeneity therefore they are extensively applied by researchers. Stoeckl et al. (2016) developed a numerical benchmark to test variable-density lens modeling. We may notice a complex numerical setting is usually time expensive. Researchers have to make a trade-off between a complex and realistic model and required prolonged time. A two-dimensional model is often made to represent three-dimensional model to reduce code running time (Comte et al.2010; Tang et al., 2020). Another important role of numerical models is that they often used as validation for analytical solutions, laboratory and site investigations. Ketabchi et al., (2104) conducted a numerical model to validate their derived analytical solutions for a layered aquifer with a sea-level rise. Post et.al (2017) studied the effect of the storm flood on the island of Baltrum (Germany) by density-driven flow model and field data. Stoeckl and Houben (2012) used numerical models and physical experiments to simulate the growth and degradation of groundwater lenses and found that lenses immediately decayed after terminating recharge and recovered to almost the surface level corresponding to zero recharge.

2.3 Laboratory and Field Observations

Laboratory models are an important tool to explore the dynamics of freshwater lens. Stoeckl and Houben (2012, 2015) performed a series of experiments to study the growth

and decay of lenses in single-layer homogeneous and layered heterogenous systems. Rapid responses to changing recharge were demonstrated by a recent laboratory tank experiment (Bedekar et al., 2019). Freshwater lens up-coning is also studied by laboratory experiments. Oswald et al. (2002) visualized saltwater upconing via nuclear magnetic resonance imaging. Abdoulhalik and Ahmed (2018) simulated a laboratory-scale costal aquifer to investigate the transient upconing process. Physical models are applied to validate the analytical solutions. Lu et al., (2019) designed tank laboratory experiments to verify their developed analytical solutions of the freshwater-seawater interface location in vertically layered aquifers. The difference between analytical and physical models is discussed by Werner et al. (2009). He compared laboratory observations with the analytical solution derived by Dagan and Bear (1968), and found obvious discrepancy at a high freshwater-seawater density difference and a low pumping rate.

Field studies are largely resources required. Installing monitoring infrastructures can be challenging in isolated islands (Falkland, et al., 1991; Werner et al., 2017). Monitoring wells are essential component in network systems. The monitoring time is often up to be decades (Post et.al, 2018). However, comprehensive monitoring systems have been estimated on multiple islands to evaluate freshwater lens behavior. On the island of Bonriki, South Tarawa, Kirribati, one of the largest islands in the Pacific (Post et.al, 2018), researchers collected monitoring data for more than three decades to comprehensively study the influence of variable rainfall and pumping activity on freshwater lens. They also used a numerical model to calibrate their observed groundwater salinities. The combination of mathematical model and field investigations is common seen in research of groundwater lens. Bailey et al., (2013) developed an algebraic model based on filed data to calculate the

maximum lens thickness on the atolls of the Federated States of Micronesia. In this model, a drought factor was established to account for the effect of intense drought conditions on groundwater lenses. Alsumaiei and Bailey (2018) conducted numerical simulations to evaluate the fluctuation of the lens volume for four representative islands in the Republic of Maldives. Their results showed that changing recharge patterns considerably influenced the volume of lenses on small islands. Motevalli et al., (2018) conducted a field study on the Ghaemsgagr-jutbar aquifer, producing a map of vulnerability using comprehensive salinity index (saltwater upconing and seawater intrusion combined) for this region. Similar field study also were conducted on Rottnest Island, Western Australia (Bryan et al., 2016), Marshall Islands (Barkey and Bailey, 2017) and Bonriki Island, Kiribati (Post et al., 2018).

Most field investigations were site specific, and the validity of generalizing those findings to other islands with different hydrogeologic and climate conditions is unclear. For example, numerous filed studies have been implemented to explore the effect of time-dependent recharge on lens on small islands. Some found changing recharge significantly alter the structure of lens. Huizer et al., (2018) examined the effect of actual recharge on the growth of lens on Dutch coast between 2011-2016. Their simulation showed that the changing recharge rate led to considerable reconstruction of groundwater lens. But some researchers have different observations. Schneider and Kruse (2006) showed that the depth of lenses had no response to seasonally varying recharge based on numerical simulations and field data. Alrashidi and Baily (2019) also found the lens has extremely slow response to reduced recharge in an arid region, i.e., 50% reduction in annual recharge for 100 years corresponding to 9% reduction of lens volume for water quality threshold of 2000 mg/l.

CHAPTER 3. IMPACT OF TIME-DEPENDENT RECHARGE ON FRESH GROUNDWATER LENS DEVELOPMENT

In the twenty-first century, climate change has become a huge concern due to the increasing emission of greenhouse gas (Hsiang et al., 2017). Climate change is associated with severe weather events such as long-term droughts or elongated rain seasons (Bergquist et al., 2019; Dai et al., 2018; Mukherjee et al., 2018; Ohba and Sugimoto, 2019), which particularly affect residents on small islands. In this chapter, we derive an approximate analytical solution to describe the transient change of groundwater lens for time-dependent, fluctuating recharge rates by the method of linear convolution. Using this analytical solution, we investigate the impact of periodic recharge, extended drought events and random time-series recharge on the changing behavior of lens thickness and volume. We further analyze the approximate analytical solution using the method of low-pass filter. The complex physical process of the lens movement is fitted into a second-order system on the frequency domain.

3.1 Conceptual Model

Figure 1 represents a typical two-dimensional conceptual model of the fresh groundwater lens on small islands. For simplicity, we consider strip islands and linear flow equations. The length of the island is considered much longer than its width, $2W$ [L]. For circular islands, W is the island radius and radial flow equations should be applied. The aquifer is homogeneous, isotropic and unconfined. Saltwater with a constant sea level invades from

both sides of the island. A specific recharge rate, ω [L/T] is assumed time-dependent and uniformly distributed at the surface. A groundwater lens is formed floating above the seawater due to density difference, creating a sharp interface between freshwater and seawater. The thickness of groundwater lens, *H*, is defined as the distance from the interface to the sea level, which is a function of the distance to the island center. The aquifer thickness is assumed to be greater than the maximum thickness of the groundwater lens.

3.2 Approximate Analytical Solution

3.2.1 Hantush Solution (1968)

Hantush (1968) provided an approximate analytical solution to describe the interface growth to the steady state profile given a constant recharge rate for a strip island without sea boundaries. This solution neglects the storage effects of water expansion and aquifer compression, i.e., all recharged water causes the increase of the lens thickness and the expansion of the lens volume. In addition to the Ghyben-Herzberg approximation and Dupuit assumption, the solution assumes that the groundwater lens thickness is proportional to the average hydraulic head between the water table and interface, analogous to the typical assumption used to estimate the water table of single-density flow in an unconfined aquifer. Moreover, the solution only considers the recharge to the saturated zone and neglects the change of the unsaturated zone, which was confirmed to be accurate for long-term behavior by variable-saturation numerical simulations (Ketabchi et al., 2014).

For the conceptual model shown in Figure 3, we assume that in the surficial aquifer the storage change from water expansion and aquifer compression is neglected (Hantush,

1968). Thus, the lens growth and decay are fully controlled by the net recharge rate into the aquifer, and the groundwater flow equation can be described by the continuity equation:

$$\frac{\partial q_x}{\partial x} + \frac{\partial q_z}{\partial z} = 0 \tag{7}$$

where q_x and q_z are specific or Darcy's velocities at x and z-direction, respectively. By applying the Dupuit assumption of horizontal flow in the lens, at the freshwater table, we have:

$$q_z(h) = -\omega + \frac{\varepsilon dh}{dt} \tag{8}$$

where ε is the porosity. It describes the net inflow rate into the lens due to recharge and water table change rate.

At the interface,

$$q_z(-H) = -\frac{\varepsilon dH}{dt} \tag{9}$$

which implies that the change of the interface thickness is controlled by the flow rate. We can integrate Eq.(7) along the z direction and apply Leibnitz's rule:

$$\frac{\partial \left(\int_{-H}^{h} q_x dz\right)}{\partial x} - \frac{q_x(-H)\partial H}{\partial x} - \frac{q_x(h)\partial h}{\partial x} + q_z(h) - q_z(-H) = 0 \tag{10}$$

Substituting Darcy's law $q_x = -K\frac{\partial h}{\partial x}$ and $h = \delta H$ into Eq. (10), the governing equation is derived as:

$$\frac{K\delta H}{\varepsilon}\frac{\partial^2 H^2}{\partial x^2} + \frac{2H\omega}{\varepsilon(1+\ \delta)} = \frac{\partial H^2}{\partial t} \tag{11}$$

Eq. (11) can become linear in term of H^2 by applying the method of linearization of the Boussinesq equation (Bear, 2012). H is replaced by the areal average thickness $\bar{H}$. Eq.(11) is rearranged as:

$$\frac{K\delta\bar{H}}{\varepsilon}\frac{\partial^2(H^2)}{\partial x^2} + \frac{2\bar{H}\omega}{\varepsilon(\delta+1)} = \frac{\partial H^2}{\partial t} \tag{12}$$

where K [L/T] is the hydraulic conductivity and $\bar{H}$ [L] is the average of the areal distribution of the depth, which is estimated using a trial method provided in a series of papers (Hantush, 1964, 1967, 1968). The detailed procedure to get the estimated value of $\bar{H}$ for the specific condition in our study is shown in Hantush (1968).

The initial and boundary conditions are:

$$H^2(-\infty, t) = 0 \tag{13}$$

$$H^2(+\infty, t) = 0 \tag{14}$$

$$H^2(x, 0) = 0 \tag{15}$$

Hantush (1968) provides a solution to solve the above equations. The solution describing the time-dependent squared thickness from the initial condition of zero lens thickness, i.e., the water table at the sea level, is given by:

$$H^2(x,t) = \frac{\omega\bar{H}t}{(1+\ \delta)\varepsilon}[S^*(n) + S^*(\bar{n})] \tag{16}$$

$$n = \frac{W + x}{\sqrt{\frac{4K\delta\bar{H}t}{\varepsilon}}} \tag{17}$$

$$\bar{n} = \frac{W - x}{\sqrt{\frac{4K\delta\bar{H}t}{\varepsilon}}} \tag{18}$$

$$S^*(\alpha) = \int_0^1 \mathrm{erf}\left(\frac{\alpha}{\sqrt{\tau}}\right) d\tau \tag{19}$$

To extend Hantush solution for describing the conceptual model with constant sea-level boundaries, we can apply the method of image boundary to evaluate the interface profile:

$$H^2(x) = Z(x) + \sum_{i=1}^{\infty} (-1)^i [Z(-2iW + x) + Z(2iW + x)] \tag{20}$$

where $Z(x)$ is Hantush solution given by Eq. (16).

$Z(x)$ will decay dramatically with increasing x. In our experiment, we use four terms for the infinite series and our practice shows that the truncation error is smaller than 0.1%. Figure 4 shows the growth of groundwater lens thickness at different distances for a specific case given a set of typical hydrogeologic and geometric parameters. The thickness increases from zero rapidly and gradually approaches its steady-state thickness. Typically, a long period up to years is needed for the lens to reach its steady state. At the island center, x = 0, the lens thickness is the maximum over the whole domain. The thickness of the

groundwater lens or the depth of the interface decreases with the distance from the center, forming the lens shape schematically shown in Figure 1.

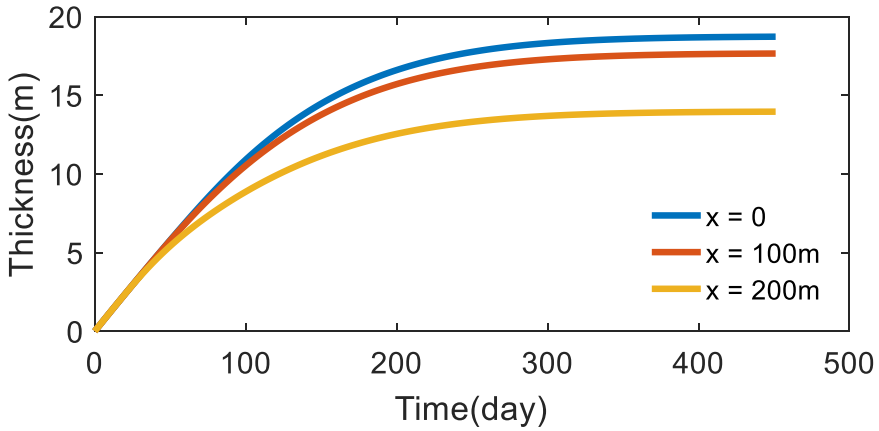

Figure 4. Growth of groundwater lens thickness to the steady state at different locations on an island with the width 600m, hydraulic conductivity 10^{-3} m/s, recharge rate 10^{-7} m/s, and porosity 0.1.

3.2.2 Dimensional Analysis

To generalize the solution, we normalize the coordinate by the island width and define the following dimensionless variables:

$$H^* = \frac{H}{W}, \quad \omega^* = \frac{\omega}{K}, \quad \bar{H}^* = \frac{\bar{H}}{W}, \quad t^* = \frac{Kt}{W\varepsilon}, \quad x^* = \frac{x}{W} \tag{21}$$

The solution, Eqs. (16) – (18), can then be written as:

$$H^{*2}(x^*, t^*) = \frac{\omega^* \bar{H}^* t^*}{1 + \delta}[S^*(n^*) + S^*(\bar{n})] \tag{22}$$

$$n^* = \frac{1 + x^*}{\sqrt{4\delta \bar{H}^* t^*}} \tag{23}$$

$$\bar{n}^* = \frac{1 - x^*}{\sqrt{4\delta \bar{H}^* t^*}} \tag{24}$$

Similar dimensionless variables are defined in previous studies (Ketabchi et al., 2014).

3.2.3 Linear System Approach for Time-Dependent Recharge

The approximate analytical solution for the simplified system is linear in terms of the squared thickness H^{*2}. Thus, the development of lenses at each location can be described by a linear convolution for a time-dependent recharge rate:

$$H^{*2}(x^*, t^*) = \int_{-\infty}^{+\infty} \omega(\tau) h(x^*, t^* - \tau) d\tau \tag{25}$$

where h is known as the unit impulse response or transfer function of the squared thickness corresponding to a unit impulse recharge. In such a system, the recharge rate is considered as the input signal, which triggers the system to generate the output signal H^{*2}. A time-dependent recharge to the system is decomposed into impulses of different magnitudes, and the output is the sum of the responses for all impulse inputs. The effects of all the other hydrogeologic parameters are described by the unit impulse response function, which characterizes the inherent property of the system.

The dimensionless impulse response function, h, at a certain location can be derived as the following:

$$h(x^*, t^*) = \frac{\partial H^{*2}}{\partial t^*} = \frac{\omega^* \bar{H}^*}{1 + \delta}[S^*(n^*) + S^*(\bar{n})] + \frac{\omega^* \bar{H}^* t^*}{1 + \delta}\left[\frac{\partial S^*(n^*)}{\partial t^*} + \frac{\partial S^*(\bar{n}^*)}{\partial t^*}\right] \tag{26}$$

where

$$\frac{\partial S^*(n^*)}{\partial t^*} = \frac{\partial S^*(n^*)}{\partial n^*}\frac{\partial n^*}{\partial t^*} \tag{27}$$

$$\frac{\partial S^*(\bar{n}^*)}{\partial t^*} = \frac{\partial S^*(\bar{n}^*)}{\partial \bar{n}^*}\frac{\partial \bar{n}^*}{\partial t^*} \tag{28}$$

and

$$\frac{\partial S^*(n^*)}{\partial n^*} = \int_0^1 \frac{2}{\sqrt{\pi\tau}} exp\left(-\frac{n^{*2}}{\tau}\right) d\tau \tag{29}$$

$$\frac{\partial S^*(\bar{n}^*)}{\partial n^*} = \int_0^1 \frac{2}{\sqrt{\pi\tau}} exp\left(-\frac{\bar{n}^{*2}}{\tau}\right) d\tau \tag{30}$$

$$\frac{\partial n^*}{\partial t^*} = -\frac{1 + x^*}{4\sqrt{\delta \bar{H}^*}} t^{*-\frac{3}{2}} \tag{31}$$

$$\frac{\partial \bar{n}^*}{\partial t^*} = -\frac{1 - x^*}{4\sqrt{\delta \bar{H}^*}} t^{*-\frac{3}{2}} \tag{32}$$

Figure 5 shows the impulse responses of the system at different locations of the domain corresponding to a unit delta function of recharge. All the curves rapidly increase from zero, indicating a prompt response to the recharge. The peak values and times to reach the peak vary with the distance to the center. At the center, $x = 0$, it has the highest peak value and needs the longest time to reach because the interface has the maximum thickness at this point. After the peak, the thickness gradually deceases to zero, representing the system recovers to its initial state. Eventually, the impulse recharge exerts no influence on the system after $t^* = 1300$. Since the unit impulse represents an unrealistic large recharge

rate, we scale the unit impulse $\delta(t)$ to $10^{-4}\delta(t)$ and use the scaled impulse response functions to allow the model to be conveniently applied to physical systems.

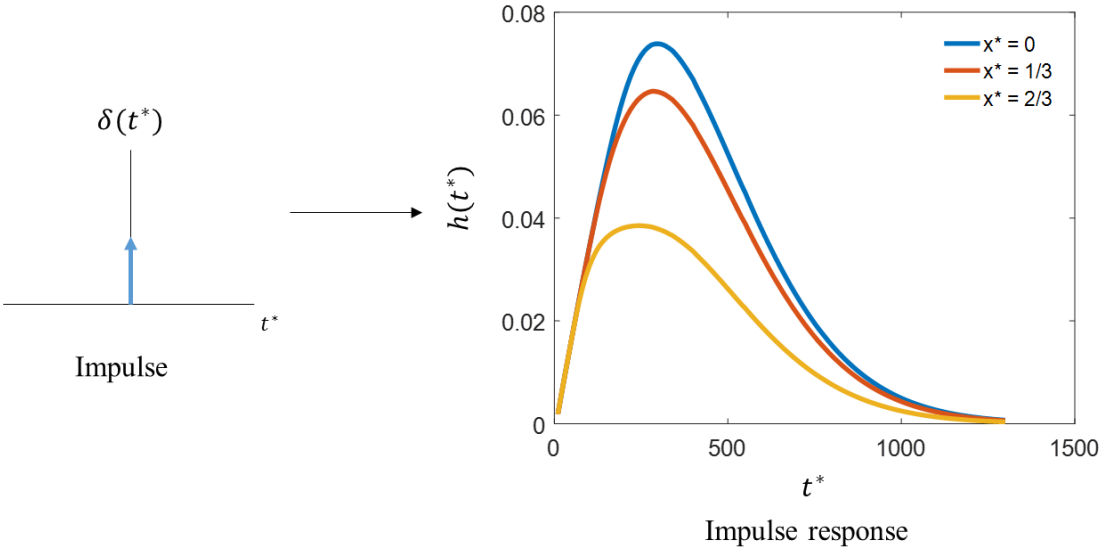

Figure 5. Dimensionless impulse response functions of squared lens thickness at different distances to the domain center in response to a unit impulse recharge function. $x^* = 0$ represents the island center.

The transient lens volume or area can be obtained by integrating the lens thickness over the domain:

$$A^*(t^*) = \frac{A}{W^2} = 2\int_0^1 h^{1/2}(x^*, t^*)dx^* \tag{33}$$

We shall notice that the transfer function *h* describes the squared thickness. Thus, the lens volume or area is a nonlinear function.

3.3 Application

In this section, we use the approximate analytical solution to conduct numerical experiments to examine the transient behavior of the interface profile and total lens volume for three types of time-dependent recharge rates: periodic recharge, extended drought events, and random time series. The interface profile behavior is represented by the lens thickness at the island center, i.e., $x = 0$.

3.3.1 Periodic Recharge Function

We consider a periodic stepwise function as the recharge rate, which switches between a high and low rate (Figure 6a):

$$\omega^*(t^*) = \begin{cases} 2 \times 10^{-4}, & 2(i-1)T^* < t^* \leq (2i-1)T^*, i = 1,2,3,\dots \\ 1 \times 10^{-4}, & (2i-1)T^* < t^* \leq 2iT^*, i = 1,2,3,\dots \end{cases} \quad (34)$$

where T^* is the dimensionless half period, and i is the number of periodic cycle.

We shall notice that within a long period of many recharge cycles the total durations of high and low recharge are equal and independent of the period, and the average recharge rate is constant. Figure 6(b) shows the response of the groundwater lens volume and thickness at the center for recharges with different periods. The patterns for volume and thickness varying are extremely close, indicating the thickness at the center effectively represents the whole volume of the lens. The three black dashed lines represent cases with a constant recharge of high value 2×10^{-4}, low value 1×10^{-4} and the average value 1.5×10^{-4}, respectively. For all cases, the lens volume or thickness initially grows along the high recharge curve because the periodic function starts at the high value, and then fluctuates around the curve with the average recharge. All curves are bounded by the high-recharge and low-recharge curves. For longer periods, i.e., larger T^* values, the lens development

shows more obvious periodic fluctuations. In fact, the curve of $T^* = 800$ fluctuates down and up to both bounding curves. For short periods, such as $T^* = 100$, only slight fluctuations can be observed. Thus, for short recharge periods, one may assume that the system is almost steady state at late time and it is reasonable to use the average recharge rate to describe the lens shape and estimate the lens volume.

Figure 7 shows the volume fluctuation normalized by the difference between two bounding curves versus T^*. The fluctuation is calculated as the difference between the maximum and minimum of each curve for its stable fluctuation period, ignoring the initial rising part. The volume fluctuation is increasing with larger T^*. Fluctuations of 10%, 50% and 100% are corresponding to about $T^* = 200$, 500 and 1300 (their dimensional form $t = 69$ days, 174 days and 451 days given our parameters), demonstrating typically seasonal or yearly varying recharge is capable to cause apparent fluctuation of lens volume.

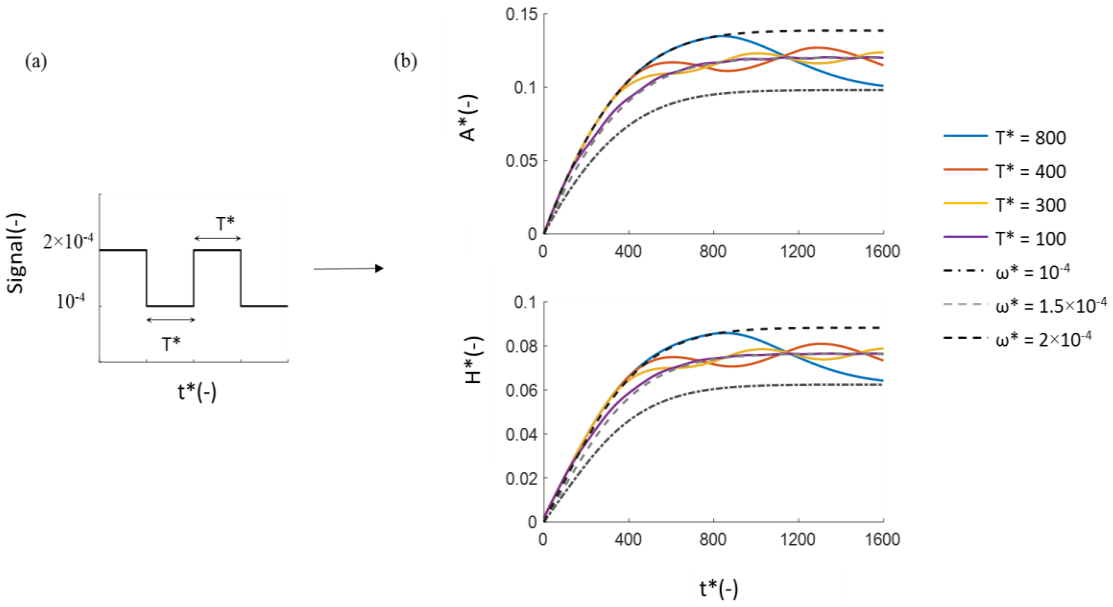

Figure 6. Groundwater lens shape and volume in response to periodic recharge. (a) Recharges with different cycle periods; (b) corresponding responses of the lens's volume and thickness at the center.

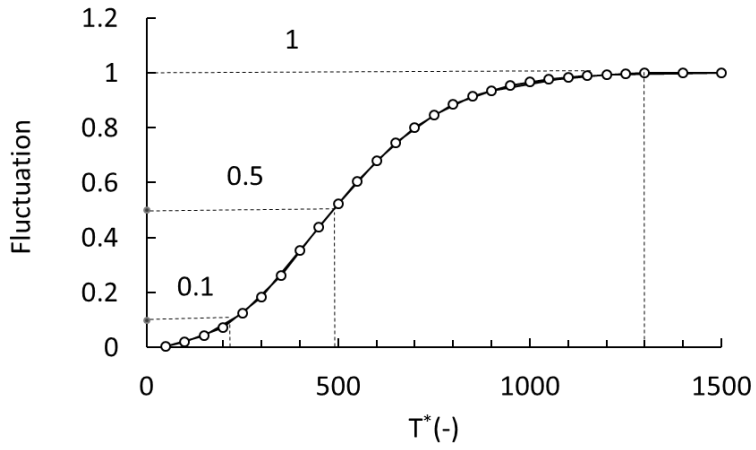

Figure 7. Increasing normalized fluctuation versus T^*. Fluctuations of 10%, 50% and 100% are corresponding to about $T^* = 200$, 500 and 1300.

3.3.2 Extended Drought Events

For simulating extended drought events, we assume that the total yearly recharge is constant but there is a period of drought with no recharge. We define an average monthly recharge rate at $\omega = 10^{-8}\ \mathrm{m/s}$. Three scenarios are considered: the average recharge through a year, the total recharge occurring in half a year, and in a month. The later two represent a drought period of half a year and 11 months, respectively. Correspondingly, the recharge intensity is increased within the wet season to keep the total recharge constant. Figure 8 shows the periodic change of the lens volume and thickness at the center. Since the total yearly recharge is constant, both drought events fluctuate about the average recharge case. However, the longer drought event, i.e., the one-month rainfall case, has a larger fluctuation amplitude with a higher peak and lower minimum because the recharge rate is higher during the rainfall season and longer drought period, indicating that elongated droughts have more substantial impact on the groundwater lens. For the selected parameters, the volume and thickness change ratios compared with the average value are about 60% and 25% for the scenarios with one-month and six-month recharge, respectively.

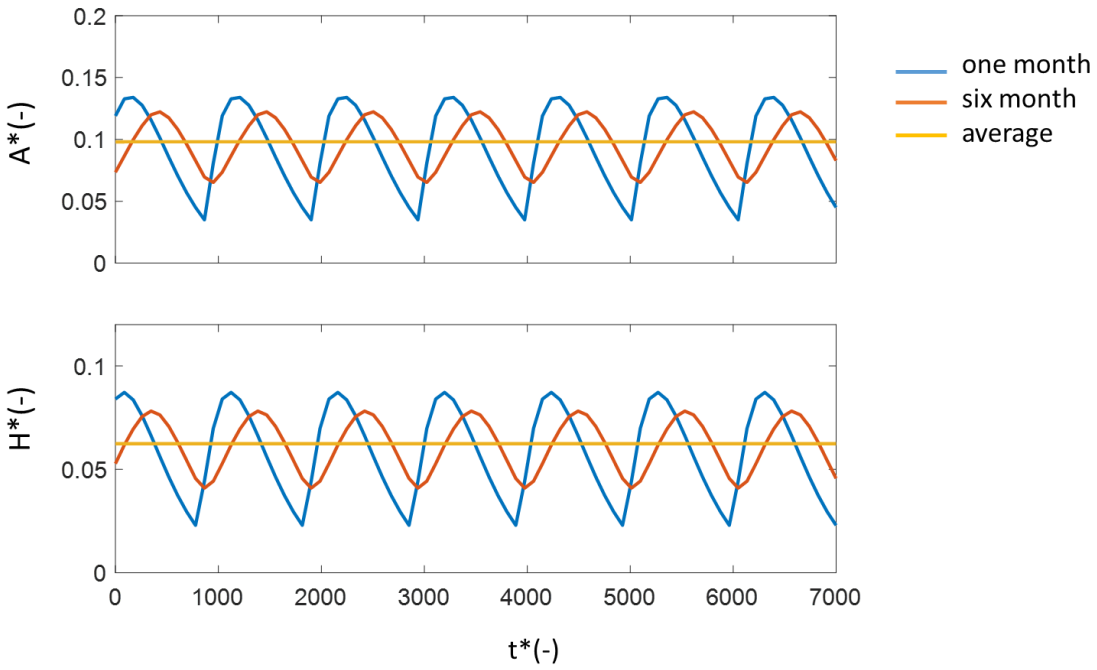

Figure 8. Groundwater lens dimensionless volume (a) and thickness (b) for one month, six month and a constant average rainfall each year.

3.3.3 Random Time-series Recharge

Both previous two cases describe constant deterministic recharge patterns. Since precipitation is typically a changing time series, the recharge rate is correspondingly considered as a time series random function. In this case study, we generate random time series of monthly recharge rates. The total yearly recharge is constant, and the monthly recharge is sampled by methods of fragments (Srikanthan and McMahon, 2001). Twelve fragments are selected randomly from n sets of fragments generated by n-year history data. Here we used rainfall data of St. Georgia Island in Florida, USA (data retrieved from Florida Climate Center). The total recharge of each year was set as the same value as that in section 3.4.2. Figure 9 shows the fluctuating lens volume (a) and thickness (b) for one

realization of random monthly recharge (Figure 9c). Similar to Figure 6, the volume and thickness have greatly similar varying pattern. It shows that the lens volume or thickness has a much slower varying frequency than the recharge because the change of volume or thickness is based on the superposition of all previous recharge, which smooths the fluctuations. In addition, the mean case based on 5000 realizations of random monthly recharge is of a smaller fluctuation than one realization. The periodicity of mean cases for both volume and thickness are similar to Figure 8, indicating that the mean of random recharge reflects the pattern of rainfall seasonal changing.

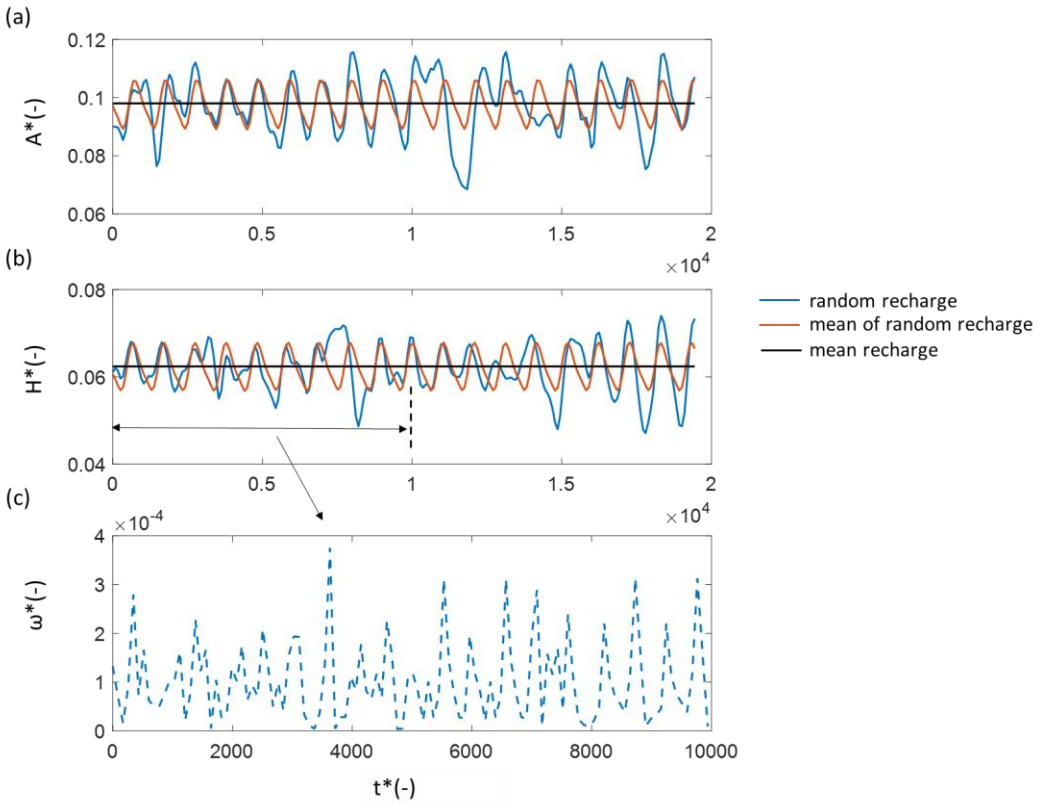

Figure 9. Groundwater lens volume corresponding to random time-series recharge. Dimensionless volume (a) and dimensionless thickness (b) for a random monthly recharge, the mean of 5000 realizations of random recharges, and a constant mean recharge; (c) the random monthly recharge over a period time of t* = 10000.

3.4 Low-pass Filter Analysis

As discussed above, the lens interface profile is considered a system response to the input signal, i.e., the recharge rate. To facilitate the understanding of this complex high-order system behavior, we simplify the impulse response by fitting a second-order model for the frequency response (Oppenheim et al., 1996):

$$H(j\omega_f) = \frac{1}{(j\omega_f/\omega_n)^2 + 2\zeta(j\omega_f/\omega_n) + 1} \tag{35}$$

where ζ is damping ratio; ω_n is undamped natural frequency; ω_f is variable frequency. Damping ratio is to describe how the system reduces its oscillation caused by disturbance, and natural frequency is the rate of the oscillation with no force disturbing. Impulse and step response can be conveniently derived from frequency response. As ζ decreases, the oscillatory behavior becomes more obvious for both impulse and step response, while as ζ increases to one, oscillatory behavior disappears and step responses becomes slower, indicating more time required for the system to approach its steady state. ω_n controls the scale of time and frequency because frequency response is a function of ω_f/ω_n (Oppenheim et al., 1996).

The step responses at two locations, the domain center and the edge, are chosen to fit the second-order frequency response model to represent the behavior of the system. Figure 10 shows that the lens development process is successfully described by a second-order frequency response model. The fitted parameters are summarized in Table 1. The damping ratio ζ is less than but very close to 1, indicating that the system is underdamped with considerably damped oscillatory behavior, corresponding to the non-vibrant physical system. In the real case, the thickness development is a pure non-vibrant process because the thickness of the lens will not exceed the final values in the process. The natural frequency ω_n is small, implying a slow process to reach the final state. In fact, the response timescale of t^* takes as high as 1300 to reach its final state. This timescale value is consistent with that of the impulse response (Figure 5), in which the impulse input has

no influence on the system after t^* = 1300, i.e., the impulse completely passes the system, and the system is back to stable.

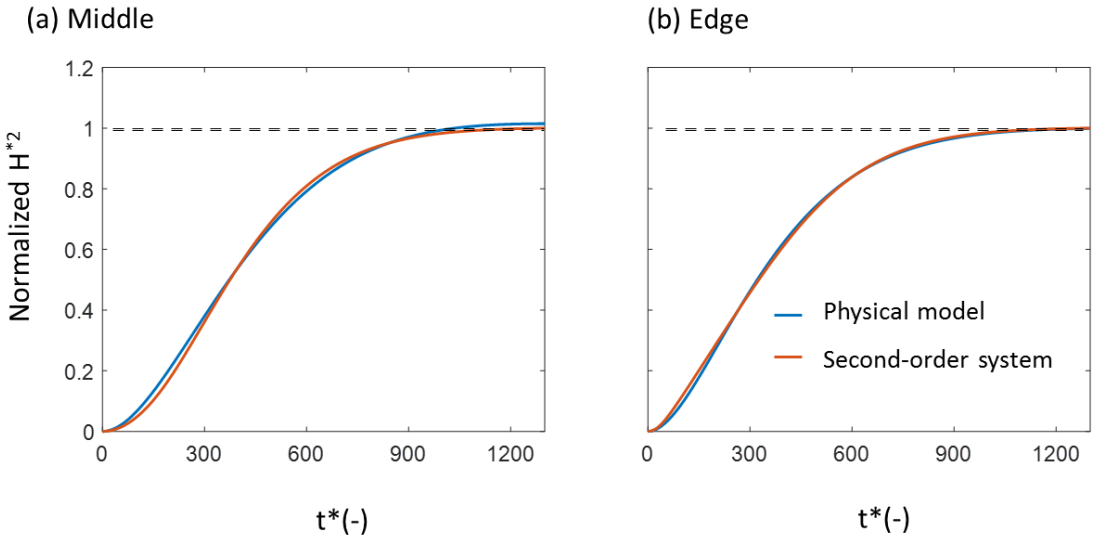

Figure 10. Fitting of the physical model to the second-order system at the domain center (a) and edge (b).

Table 1. Fitted parameters for the second-order frequency response model.

Parameter	**Domain center**	**Domain edge**
ζ	0.8220	0.9611
ω_n	0.004	0.005

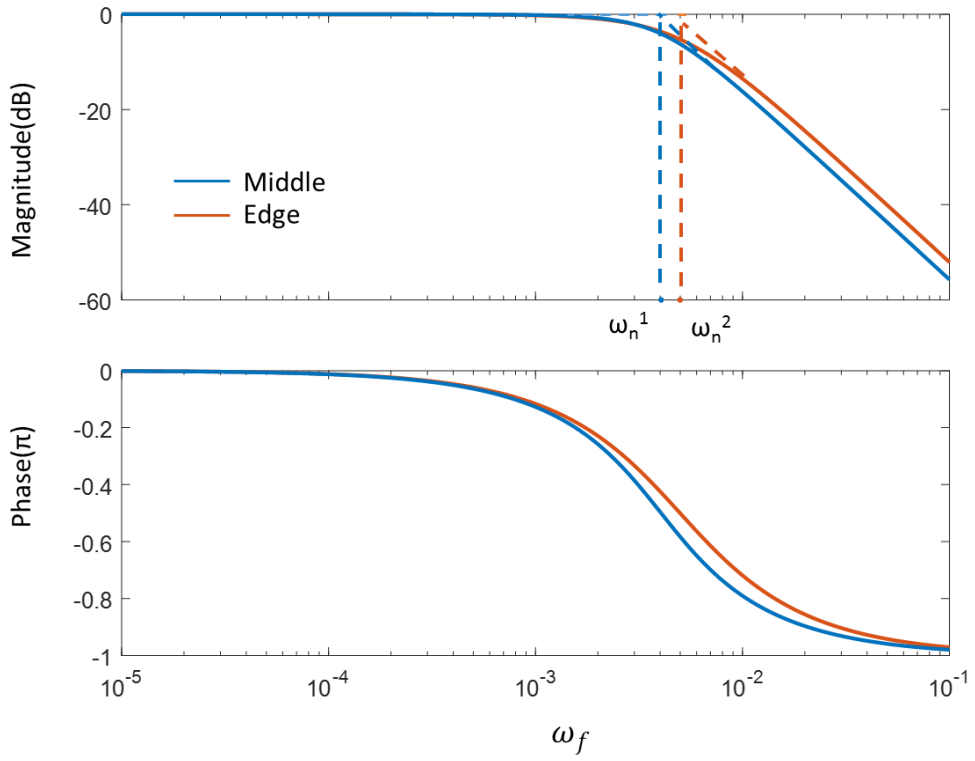

Figure 11. Bode plot of system frequency response. $1\ \text{dB} = 20\log_{10}|H(\omega_f)|$ and $\text{Phase} = -\tan^{-1}(\frac{2\zeta(\omega_f/\omega_n)}{1-(\omega_f/\omega_n)^2})$.

Figure 11 shows the bode plots of frequency responses at the two locations. Bode plots shows the magnitude attenuation and phase shift for a sine wave as it passes the system. The system with the kind of Bode plots shown in Figure 11 is considered as a low-pass filter, which only passes low frequency sine-wave signals and rejects those with high frequencies. There are two asymptotes in the magnitude plot for each curve. One is at low frequency and parallel to *x* axis, and the other asymptotically approaches the decreasing part of the curve. Both low and high frequency asymptotes are approximately straight lines and they meet at ω_n. The straight-line approximation suggests that the magnitude of the frequency response is 0 dB for $\omega_f < \omega_n$ and almost linearly decreases with frequency for

$\omega_f > \omega_n$. ω_n is referred to as the break frequency. For input sine-waves with $\omega_f < \omega_n$, their magnitudes will stay exactly the same after passing the system. For those with the frequency larger than the break frequency, magnitudes are reduced. We notice that the high frequency asymptotes at the two locations are parallel with a slope of -40 dB per decade, that is, the magnitude of $H(\omega_f)$ decreases 40 dB for each increase of ω_f by 10 times. This slope suggests that this system attenuates steeply at high frequencies. When the frequency of sine waves is larger than 0.1, the magnitude is reduced to nearly 0.001 of original magnitude. That is, these sine-wave signals are rejected by the system. Additionally, the Bode plots (magnitude and phase) for two points (center and edge) are very similar, indicating that the capacity for the system to attenuate magnitude and shift phase is greatly similar over the whole domain.

Figure 12 shows the application of the spectrum analysis for the groundwater lens development with a periodic recharge time series. The recharge rate signals with T* = 100 and T* = 800 are presented on the spectrum space based on Fourier series analysis. Recharge with the longer periodic cycle is mostly decomposed into lower frequency sine-waves. As we discussed above, frequency smaller than the break frequency can entirely pass the system with no reduction. Frequency between 0.1 and break frequency is attenuated to some degree. Frequencies higher than 0.1 can be considered as rejected. For T* = 100, more sine-wave components are distributed on the frequencies higher than 0.1, suggesting that more components are rejected. That is why Figure 6 shows that more frequent recharge pattern leads to weaker periodic outputs because most periodic components are blocked. Moreover, the average recharge is the first term of Fourier series, representing the average value of the input over one periodic cycle. Thus, given a constant

average recharge, all recharge cases in Figure 6 have the same average value on their spectrums. Because the average point is of no frequency and is not be attenuated by the system, all the curves in Figure 6 grow around the curve of the average recharge rate. If the recharge rate frequency is high enough, all the components of this input will be rejected expect the average signal, resulting in the smooth average lens volume curve without any fluctuation.

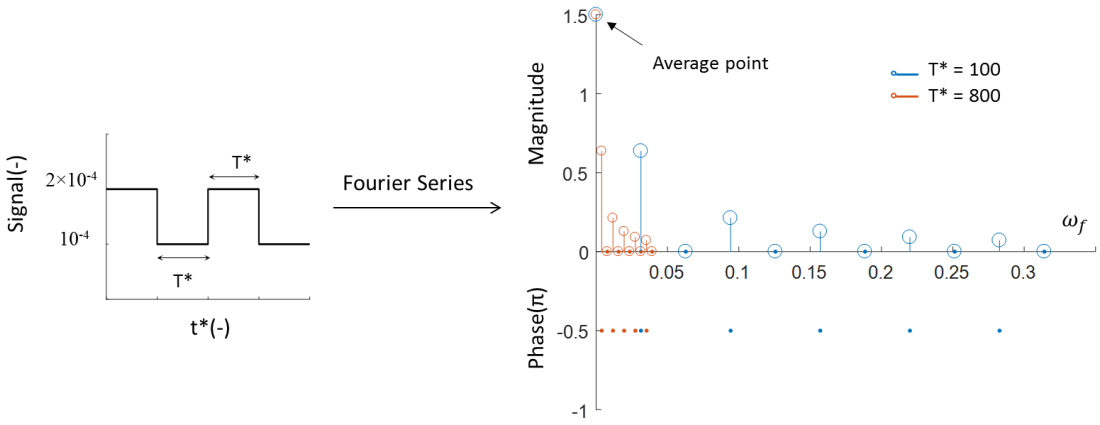

Figure 12. Periodic recharge with different cycle length and corresponding spectrum

By contrast, for the periodic recharge rate with T* = 800, obvious fluctuations of the lens volume can be observed since the input recharge signal is decomposed into sine-waves with frequencies less than the break frequency. In Figure 10, T* = 1300 is the time when the system approaches the steady state. The recharge needs to have a period comparable to such a timescale to cause significant fluctuations of the lens thickness. Realistically, long changing timescale recharge represents long-term drought or rainfall events. By defining the timescale for the system to reach steady state as the responding timescale, we may approximate the break frequency as: $\omega_n = 2\pi/\text{responding timescale}$. In our case, the

responding timescale is around 1300 and thus the estimated break frequency is around 0.0048, close to the actual value shown in Figure 11.

3.5 Conclusion

In this paper, we derive an approximate analytical solution for transient movement of groundwater lens interface on small strip islands for time-dependent, fluctuating recharge. The system is approximated as a linear, time-invariant in terms of the squared lens thickness, and described by the method of convolution, where the transient recharge is considered as the input signal. This analytical solution is validated by numerical simulations of variable density flow and transport. We also derive a dimensionless formula for the solution, which makes it convenient to evaluate the groundwater lens changing pattern for arbitrarily time-dependent recharge.

We apply the approximate solution to study the effects of three different recharge patterns on the lens change: periodic recharge, extended drought events and random time-series recharge. For periodic recharge, the lens thickness and volume changes are bounded by those corresponding to the high and low recharge rates, and the amplitude of lens fluctuations is controlled by the magnitude of period. In general, longer period yields large fluctuations. For drought events, the duration of drought events affects the lens fluctuations. Also, longer drought events yields large lens fluctuations. For random time-series recharge, the approximate analytical solution can provide fast evaluation of the ensemble mean and variance for uncertainty quantification, which will be particularly useful to predict the lens change in future climate change scenarios with uncertainties.

By analyzing the impulse response function based on signal processing, the inherent mechanism is explained on the frequency domain by the method of low-pass filter. The complex physical process of movement of lens is successfully fitted by a second-order system. This filter has the capacity to pass sine-wave inputs with frequency lower than the break frequency while attenuate high-frequency ones. Fourier series or Fourier transformation is applied to decompose the time-dependent recharge into sine-wave components. Long changing time-scale recharge can be decomposed into sine-wave components lower than the break frequency and thus they are not blocked by the filter. Their changing pattern is able to pass the system and then cause the fluctuation of the lens. One field case and laboratory experiment are analyzed by the concept of low-pass filter. Their different behavior can be explained successfully by comparing their spectrums with the break frequency.

Our approach may not be used to accurately calculate the lens volume if a salty concentration is selected as the criterion for determining the freshwater quantity because the approach assumes sharp interface and neglects dispersion. However, it provides us an efficient tool such as frequency analysis to investigate the transient lens change pattern as a result of time-dependent, fluctuating recharge rates. More importantly, it provides many useful insights to improve understanding of lens behavior, as summarized above. By substituting site parameters, the dimensionless solutions can be used to analyze specific site conditions and predict potential behavior in future climate change scenarios.

CHAPTER 4. IMPACT OF SPATIALLY VARIABLE RECHARGE ON FRESH GROUNDWATER LENS DEVELOPMENT

The lens shape, thickness and volume are sensitive to spatially variable recharge caused by topography, soil type, land cover, evapotranspiration and human activities. We derive an analytical solution to describe transient and steady-state lens profiles for spatially variable recharge rates in a small strip island. The derived solutions are validated by a published steady-state solution for simple recharge patterns, laboratory results and numerical simulations. A Green's function is derived based on the analytical solution to quantify the temporal and spatial effect of impulse recharge. Uncertainty analysis is implemented based on the derived analytical solution to investigate the lens behavior under randomly spatially variable recharge.

4.1 Conceptual Model

Figure 3 represents the cross section of a typical two-dimensional freshwater lens in surficial aquifers in a small strip island. The length of the strip island is much longer than the width, L [L]. The aquifer is homogeneous and isotropic. Sea level is assumed constant. The recharge rate, ω [L/T], is heterogeneously distributed along the top of the domain. The fresh groundwater is separated from the seawater by a sharp interface. The thickness of the lens is defined as the distance from the sea level to the interface, which is a function of the distance to the origin, $x = 0$. The height of the aquifer is assumed much thicker than the maximum thickness of the lens so that the lens profile is fully developed.

At the freshwater table, the hydraulic head is defined by $\varphi(x, y, h, t) = h$. Based on Ghyben-Herzberg approximation and the assumption of zero hydraulic gradient along the vertical direction, the head φ is constant along a vertical line: $h = \varphi(x, y, -H, t) = \delta H$, where $\delta = (\rho_s - \rho_f)/\rho_f$ and ρ_f and ρ_s are the freshwater and seawater density, respectively.

4.2 Mathematical Modeling

4.2.1 Governing Equation

For the conceptual model shown in Figure 3, we assume that in the surficial aquifer the storage change from water expansion and aquifer compression is neglected (Hantush, 1968). Thus, the lens growth and decay are fully controlled by the net recharge rate into the aquifer, and the groundwater flow equation can be described by the continuity equation:

$$\frac{\partial q_x}{\partial x} + \frac{\partial q_z}{\partial z} = 0 \tag{36}$$

where q_x and q_z are specific or Darcy's velocities at x and z-direction, respectively. By applying the Dupuit assumption of horizontal flow in the lens, at the freshwater table, we have:

$$q_z(h) = -\omega(x) + \frac{\varepsilon dh}{dt} \tag{37}$$

where ε is the porosity. It describes the net inflow rate into the lens due to recharge and water table change rate.

At the interface,

$$q_z(-H) = -\frac{\varepsilon dH}{dt} \tag{38}$$

which implies that the change of the interface thickness is controlled by the flow rate. We can integrate Eq.(36) along the z direction and apply Leibnitz's rule:

$$\frac{\partial\left(\int_{-H}^{h} q_x dz\right)}{\partial x} - \frac{q_x(-H)\partial H}{\partial x} - \frac{q_x(h)\partial h}{\partial x} + q_z(h) - q_z(-H) = 0 \tag{39}$$

Substituting Darcy's law $q_x = -K\frac{\partial h}{\partial x}$ and $h = \delta H$ into Eq. (39), the governing equation is derived as:

$$\bar{v}\frac{\partial^2 H^2}{\partial x^2} + Q(x) = \frac{\partial H^2}{\partial t} \tag{40}$$

with

$$\bar{v} = \frac{K\delta\bar{H}}{\varepsilon} \tag{41}$$

$$Q(x) = \frac{2\omega(x)\bar{v}}{\delta(1+\delta)K} \tag{42}$$

where K [L/T] is the hydraulic conductivity and $\bar{H}$ [L] is the mean of the areal depth distribution, estimated using a trial method provided in a series of papers (Hantush, 1964, 1967, 1968). Eq. (40) becomes linear in term of H^2 by applying the method of linearization of the Boussinesq equation (Bear, 2012).

The initial and boundary conditions are:

$$H^2(0,t) = 0 \tag{43}$$

$$H^2(L,t) = 0 \tag{44}$$

$$H^2(x,0) = 0 \tag{45}$$

4.2.2 Analytical Solution

Using the method of eigenfunction expansion (Haberman, 2003), the solution can be expanded in a series of the eigenfunction of the related homogeneous problem.

$$H^2(x,t) = \sum_{n=1}^{\infty} a_n(t)\phi_n(x) \tag{46}$$

where $\phi_n(x) = \sin\frac{n\pi x}{L}$ is the eigenfunction. The coefficients $a_n(t)$ can be determined by direct substitution of $\frac{\partial H^2}{\partial t}$ and $\frac{\partial^2 H^2}{x^2}$:

$$a_n(t) = e^{-\lambda_n \bar{\nu} t} \int_0^t q_n \; e^{\lambda_n \bar{\nu} \tau} d\tau = \frac{q_n(\,1 - e^{-\lambda_n \bar{\nu} t})}{\lambda_n \bar{\nu}} \tag{47}$$

where

$$\lambda_n = \left(\frac{n\pi}{L}\right)^2 \tag{48}$$

$$q_n = \frac{\int_0^L Q(x)\phi_n(x)dx}{\int_0^L \phi_n^2(x)dx} \tag{49}$$

$$\int_0^L \phi_n^2(x)dx = \int_0^L (sin\frac{n\pi x}{L})^2 dx = \frac{L}{2} \tag{50}$$

We can derive the steady solution from Eq. (46) by letting $t \to \infty$,

$$H^2(x) = \lim_{t\to\infty} \sum_{n=1}^{\infty} \frac{q_n(\,1 - e^{-\lambda_n \bar{v} t})}{\lambda_n \bar{v}} \sin\frac{n\pi x}{L} \tag{51}$$

which yields

$$H^2(x) = \sum_{n=1}^{\infty} \frac{q_n}{\lambda_n \bar{v}} \sin\frac{n\pi x}{L} = \sum_{n=1}^{\infty} \frac{4\,L \sin\frac{n\pi x}{L}}{(n\pi)^2 \delta(1+\,\delta)K} \int_0^L \omega(x_0) \sin\frac{n\pi x_0}{L}\, dx_0 \tag{52}$$

4.2.3 Dimensional Analysis

To generalize the solution and make it conveniently applied to other sites, we normalize the coordinate by the island width and define the following dimensionless variables:

$$H^* = \frac{H}{L}, \quad \omega^* = \frac{\omega}{K}, \quad \bar{H}^* = \frac{\bar{H}}{L}, \; t^* = \frac{Kt}{L\varepsilon}, \; x^* = \frac{x}{L} \tag{53}$$

Similar dimensionless variables are defined in previous studies (Ketabchi et al., 2014).

The transient solution, Eq. (46), can then be written as:

$$H^{*2}(x^*, t^*) = \sum_{n=1}^{\infty} a_n^*(t^*)\phi_n^*(x^*) \tag{54}$$

$$\phi_n^*(x^*) = sin\,(n\pi x^*) \tag{55}$$

$$a_n^*(t^*) = \frac{4\int_0^1 \omega^*(x^*) sin\,(n\pi x^*) dx^*\,(\,1 - e^{-(n\pi)^2\,\bar{H}^* t^* \delta})}{\delta(1+\,\delta)(n\pi)^2} \tag{56}$$

The steady solution, Eq. (52), can then be written as:

$$H^{*2}(x^*) = \sum_{n=1}^{\infty} \frac{4\sin(n\pi x^*)}{(n\pi)^2\delta(1+\ \delta)} \int_0^1 \omega^*(x_0^*)\sin(n\pi x_0^*)\, dx_0^* \tag{57}$$

4.2.4 Green's Function Solution

In the conceptual model and derived analytical solution, the recharge rate is spatially variable but constant with time. For both spatially- and time-dependent recharge rates, $\omega(x,t)$, we also derive a Green's function solution for describing the impulse response of recharge. The Green's function describes the lens interface change corresponding to a momentary local recharge. Eq. (54) can be considered as the integration of these impulse responses over the spatial domain. The Green's function solution is shown below:

$$H^{*2}(x^*,t^*) = \int_0^1 \int_0^{t^*} \omega^*(x_0^*)\, G(x^*,t^*,x_0^*,t_0^*) dt_0^* dx_0^* \tag{58}$$

$$G(x^*,t^*,x_0^*,t_0^*) = \sum_{n=1}^{\infty} \frac{4\ \bar{H}^*}{1+\delta} \sin(n\pi x_0^*)\sin(n\pi x^*) e^{-(n\pi)^2\ \bar{H}^*(t^*-t_0^*)\delta} \tag{59}$$

We shall notice in Eq. (58), spatially dependent recharge $\omega^*(x_0^*)$ can be replaced by $\omega^*(x_0^*, t_0^*)$, extending the original solution to solving problems with spatially and temporally dependent recharge.

The same approach is applied for steady solution. Eq. (57) can be written as:

$$H^{*2}(x^*) = \int_0^1 \omega(x_0^*) G(x^*, x_0^*)\ dx_0^* \tag{60}$$

$$G(x^*, x_0^*) = \sum_{n=1}^{\infty} \frac{4\sin(n\pi x^*)\sin(n\pi x_0^*)}{\delta(1+\ \delta)(n\pi)^2} \tag{61}$$

4.2.5 Comparison with a Reported Analytical Solution

Vacher (1988) provided a steady-state solution based on Fetter's (1972) homogeneous model for a strip island with a recharge rate following the spatially distributed pattern:

$$\omega(\mathrm{x}) = \begin{cases} \omega_1, & \mathrm{x} < \mathrm{c} \\ \omega_2, & \mathrm{x} \geq \mathrm{c} \end{cases} \tag{62}$$

c is the dividing point of two regions. Eq. (62) describes a simple spatially heterogeneous pattern, which can be considered as a special case of our solution, Eq. (52). Figure 13 shows the comparison between our solution and Vacher's solution for the recharge pattern given by Eq. (62). It clearly shows that these two solutions are essentially identical for this specific recharge pattern. In Figure 13, the lengths of two parts are identical and the ratio between two recharge rates varies from 0 to 1, in which the zero ratio represents that only one part of the domain has recharge. The interface is symmetric with the ratio of 1, i.e., the recharge is uniform. The right half of the interface shrinks when ω_2 decreases with ω_1 fixed. The apex of the interface moves from the center to the left boundary with the decreasing ratio and thus the interface becomes asymmetric under the non-uniform recharge.

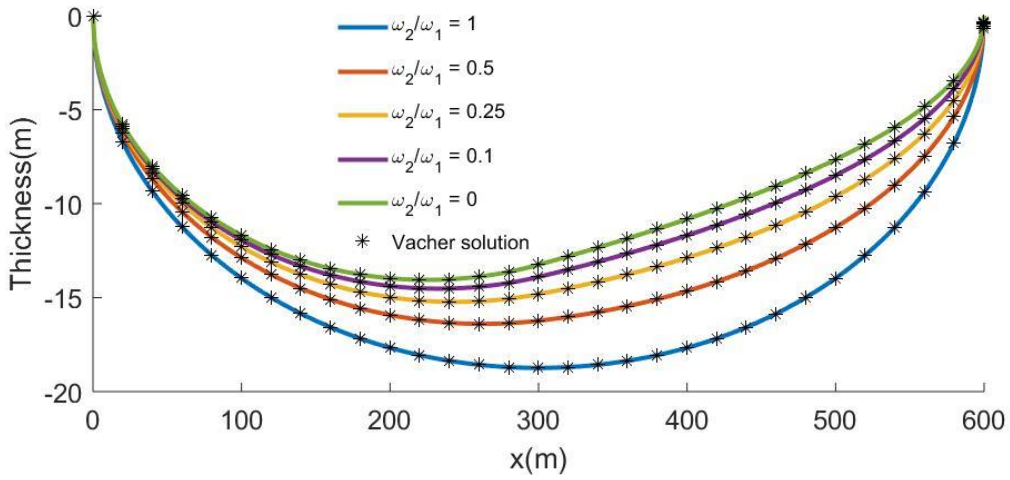

Figure 13. Comparison between the derived analytical solution and a published steady-state analytical solution for two recharge rates. The domain is divided into two halves with the recharge rate ω_1 and ω_2, respectively. The ratio between ω_2 and ω_1 varies from 0 to 1.

4.3 Application

4.3.1 Concentrated Recharge at the Domain Center

We investigate the effect of concentrated recharge by applying a same amount of total recharge to the center areas with different area or length ratio, i.e., the ratio of the area with recharge to the total domain area. Figure 14 shows the lens shape and volume (normalized by the lens volume in the uniform recharge case) for different length ratio. Lens thickness increases with the centralized, intensified recharge. When the recharge area length is approaching zero, there is a limit for the lens volume increase of about 20% compared with the homogeneous recharge distribution over the whole domain.

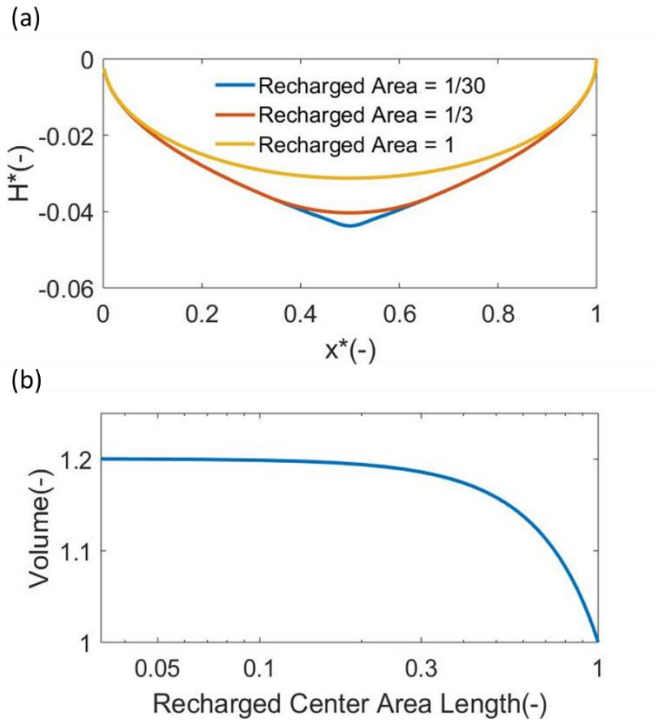

Figure 14. Groundwater lens profile and volume for centralized, intensified recharge for a given total recharge. The recharge area is represented by the recharge length normalized by the total island width. (a) Lens shape, and (b) lens volume increase.

Figure 15(a) shows the Green function $G(x^*, t^*, 0.5, 0)$ or the impulse response of the squared lens thickness at different locations. $x_0^* = 0.5$ represents that the impulse recharge is applied at the center at $t_0^* = 0$. The impulse has the strongest and quickest impact at the recharging location, $x^* = 0.5$. The effect on other points is delayed and weakened with the distance away from the center.

Figure 15(b) shows the Green's function for the steady-state solution, $G(x^*, x_0^*)$ of Eq. (61), corresponding to a unit constant recharge at a specific point x_0^*. The squared lens thickness to the point recharge shrinks to a triangle shape with the peak at the recharge location and

linearly decreases with the distance away from the recharge location. The peak value is the highest for the case with recharge at the domain center and declines as the recharge approaching the domain boundaries, implying that the recharge has more influence over the whole domain when it is closer to the center. This explains the larger lens volume caused by the more concentrated recharge at the domain center shown in Figures 14 and 15.

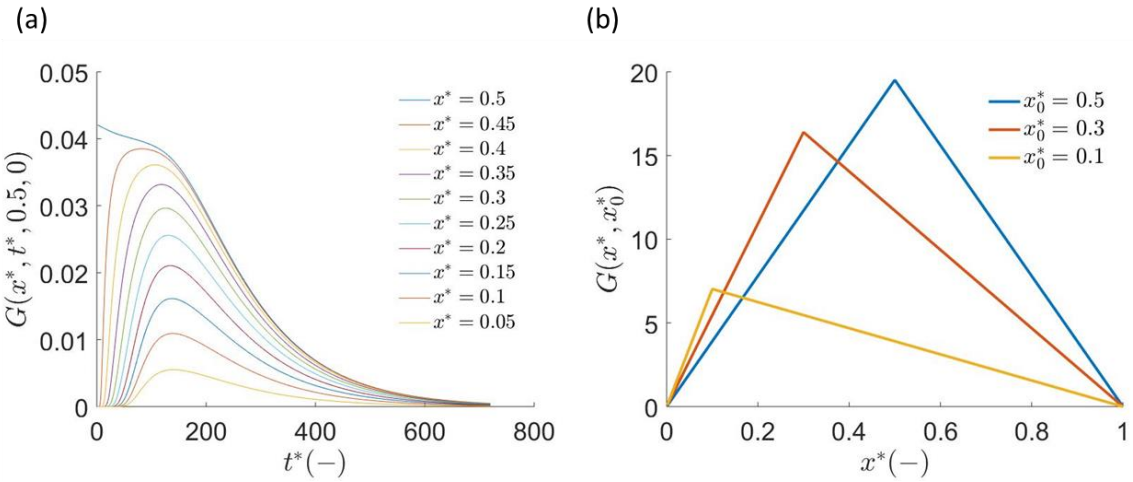

Figure 15. (a) Green function for transient solution for parameters given in Figure 4. The influence of impulse recharge at the center $x_0^* = 0.5$ at the beginning moment $t_0^* = 0$ on the whole domain. (b) Green's function for steady solution. The influence of impulse recharge at x_0^* on the whole domain.

4.3.2 Uncertainty Analysis of Randomly Distributed Recharge

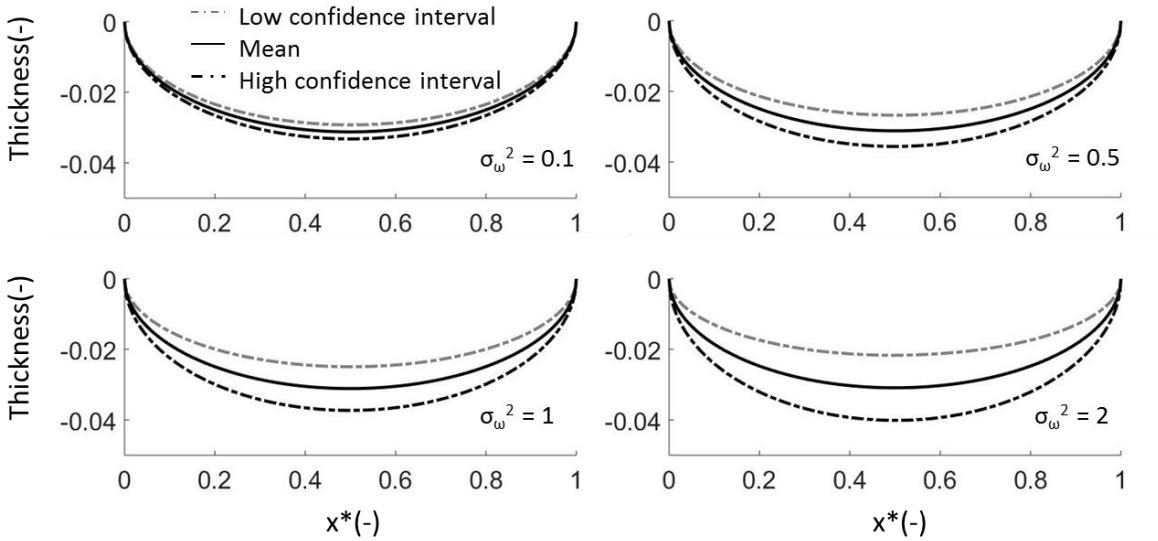

Figure 16. Mean and confidence intervals of the lens profile for different variances of recharge, σ_ω^2, from 0.1 to 2, and correlation length of 1/60 and mean recharge of 1.

For spatially variable recharge due to topography, soil type, vegetation and human activity, the recharge may be modelled as a spatially correlated random field. The derived analytical solution can be conveniently used to quantify the uncertainties of lens thickness and volume caused by spatially correlated recharge. For simplicity, the random field is assumed as a multivariate normal vector and the covariance matrix is determined by a Gaussian model:

$$R(d) = \sigma_\omega^2 \exp\left(-\frac{D^2}{L_c^2}\right) \tag{63}$$

D[-]is the distance between two points. σ_ω^2[-] is variance of recharge. L_c[-] is correlation length. We define the recharge of 10^{-4} as unit one to allow more convenient expression.

Because we directly model the recharge rate as the random function, negative values may be generated for recharge rate realizations at some locations. We consider that the negative recharge is caused by densely vegetated zone where evapotranspiration exceeds replenishment. If non-negative values are preferred, logarithm recharge rates may be used as the random function.

Figure 16 shows the low confidence level, mean and high confidence level of the lens shape under a random recharge function for variance σ_ω^2 from 0.1 to 2, correlation length of 1/60 and mean recharge of 1. The dimensionless mean volume of 10000 random realizations is 0.0242, which is close to the volume under the mean recharge, 0.0245. The confidence interval increases with σ_ω^2. The volume difference between the confidence interval and the mean profile reaches 30% for $\sigma_\omega^2 = 2$, indicating that the lens shape and volume can vary largely for a spatially variable recharge.

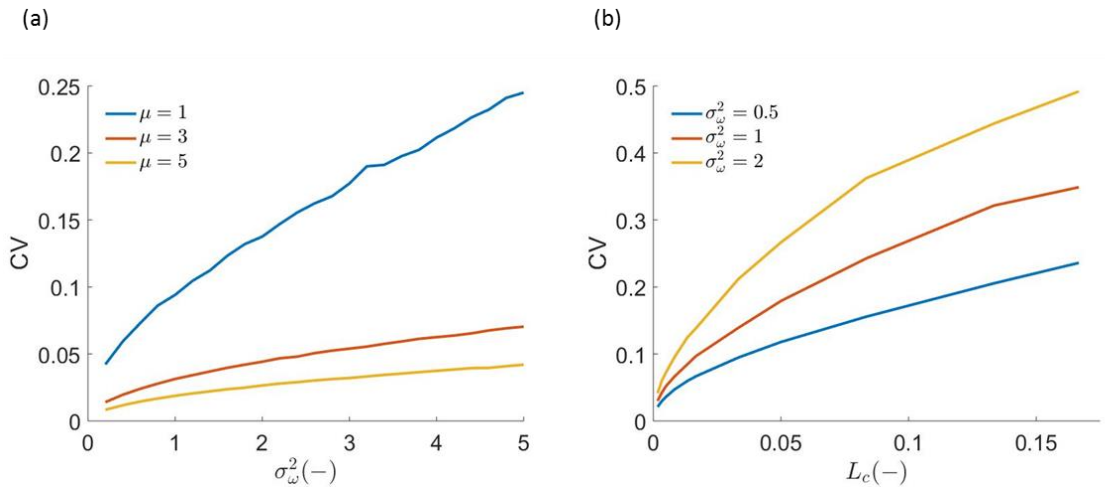

Figure 17. Lens volume change as a function of the random function coefficients. (a) Coefficient of variation (CV) versus σ_ω^2 for different mean recharge μ with correlation length of 1/60. (b) CV versus correlation length L_c for different σ_ω^2 with mean recharge μ = 1.

Figure 17(a) shows coefficient of variation (CV) of lens volume versus σ_ω^2 for mean recharge μ = 1, 3, 5 with correlation length of 1/60. In all experiments, the mean volume of multiple random realizations is close to the volume under mean recharge. The lens tends to be more stable with larger mean recharge μ. CV increases as mean recharge μ decreases. When $\sigma_\omega^2 = 5$, the lens can fluctuate 4% for μ = 5 while 25% for μ = 1, indicating that the thinner lens is more sensitive to recharge variance and thus more vulnerable to changing environment. The effect of correlation length on the lens volume's CV is shown in Figure 17(b). A highly correlated domain leads to a more fluctuated lens. When σ_ω^2 = 2 and correlation length is 1/6 of the domain size, CV is as high as 0.5, i.e., the lens fluctuates 50% compared with the volume corresponding to the mean recharge μ = 1,

4.4 Conclusion

Spatially variable recharge into aquifers is common at the field. However, very limited research has been conducted to investigate the impact of spatially variable recharge on the development of fresh groundwater lenses in small islands. In this study, we derive transient and steady-state analytical solutions of groundwater lens profiles in small strip islands with spatially variable recharge. A Green's function solution is provided for both time-dependent and spatially variable recharge. The derived solutions are validated by a published steady-state solution for simple recharge patterns, laboratory experiments and numerical simulations. Dimensionless forms of the analytical solutions are provided for general applications on different sites.

Numerical experiments based on the derived solutions show that the recharge at the domain center has the most significant impact on the whole lens. For a given constant total recharge, a smaller recharge area or a more intensified recharge rate can result in a larger lens volume by over 20% compared with the lens volume of a uniformly distributed recharge. The Green function shows that the impulse response delays and weakens with the distance away from the recharge location. More interestingly, the steady-state profile for the squared lens thickness corresponding to the recharge at a single location simplifies to a triangle function with the peak located at the recharge location and a linear decrease to zero at the domain boundaries. Moreover, the recharge at the domain center has the greatest influence over the whole domain than recharge applied at other locations, explaining the significant effect of concentrated recharge at the domain center. The derived analytical solutions can be conveniently used to quantify uncertainties introduced by spatially variable recharge. By assuming a multivariate Gaussian distribution and a specific

spatial covariance function, the uncertainty analysis based on the analytical solutions shows that the groundwater lens volume has a larger variance for a higher variance and correlation length of the spatial recharge function. The thinner lens is expected to be more vulnerable and sensitive to recharge change.

We shall notice the limitations of our developed model, including the assumption of homogeneous aquifers. That is, the spatially variable recharge is caused by the surface processes such as topography and land cover. Hydraulic conductivity heterogeneity may also contribute to the spatially variable recharge, but it impact on the flow is neglected. For general setup of heterogeneous aquifers, analytical solutions may not be available. The present study provides an effective tool to understand the temporal and spatial effect of spatially variable recharge on the lens development and useful insights for improving engineering design such as artificial recharge. The research combining both spatially variable recharge and heterogeneous aquifers such as stratified aquifers is underway.

CHAPTER 5. CRITICAL PUMPING RATE FOR SUSTAINABLE USE OF GROUNDWATER LENS

Facing the great challenge of climate change, it is extremely important to have a sustainable groundwater resources management on small islands. This chapter addresses an unanswered, simple but most important question for groundwater resources management in small islands: how much freshwater can be sustainably withdrawn from a groundwater leans in small islands.

5.1 Conceptual Model

Figure 2 shows the vertical cross section of a typical fresh groundwater lens in a small island under pumping. Strip islands are considered here for simplicity. The island length is assumed much longer than its width, $2W$ [L], allowing us to simplify the problem to the two-dimensional vertical section. The aquifer is homogeneous, isotropic and unconfined with a freshwater hydraulic conductivity, K [L/T]. Seawater boundaries at both domain sides are assumed constant-head. The impact of tidal activities is not considered by assuming that the interface fluctuations due to high-frequency tidal activities are negligible (Tang et al., 2020). A constant and uniformly distributed recharge rate, ω [L/T], is applied along the surface. The transition zone between the seawater and freshwater is approximated as a sharp interface. This simplification was initially validated by Muskat (1938) and has been widely used by numerous researchers in coastal aquifers without high heterogeneity and large dispersion (Lu et al., 2009; Lu and Luo, 2014). Freshwater is separated by this interface and floats above the seawater in the form of lens.

We define the thickness of lens as the distance from the interface to the sea level, H. We shall notice that the actual freshwater thickness is the distance from the interface to the water table, i.e., $H + h$, shown in Figure 1. A simple relationship can be established between H and h according to the Ghyben-Herzberg relationship. The interface is symmetric with the maximum thickness at the center, $x = 0$. The aquifer is assumed much thicker than the maximum thickness of the lens so that the lens is fully developed. Figure 1 schematically shows the shape of the lens under groundwater withdrawal from a single well. The pumping well is placed at the center of the lens with a penetration depth of d [L] to achieve the maximum pumping rate. Since the conceptual model is two-dimensional, the pumping well actually represents a drain or a line sink (Strack, 1972; Zhang et al., 1996, 2009). The lens interface beneath the well rises in response to pumping, changing the interface to an 'ω' shape. With the increase of the pumping rate, the center of the interface moves toward the well. A critical pumping rate can be defined as the maximum pumping rate that can be applied to prevent the interface peak from penetrating into the well, i.e., the peak remains stable as long as the pumping rate does not exceed the critical pumping rate.

5.2 Approximate Analytical Solution

5.2.1 Groundwater Lens Interface Profile

For the conceptual model shown in Figure 2, the pumping rate is assumed low so that the upconing has not penetrated into the pumping well. Due to symmetry, the analytical model describes the half island as the whole domain. By neglecting the storage effect of water

expansion and aquifer compaction, i.e., the net water flux into the groundwater lens controls the lens shape and volume (Hantush, 1968), we have the continuity equation:

$$\frac{\partial q_x}{\partial x} + \frac{\partial q_z}{\partial z} = 0 \tag{64}$$

where x [L] is the distance from the center; z [L] is the vertical coordinate; q_x and q_z are specific or Darcy's velocities at x and z-direction, respectively.

We can integrate Eq. (64) along the z direction over the freshwater lens thickness and apply Leibnitz's rule:

$$\frac{\partial \left(\int_{-H}^{h} q_x dz \right)}{\partial x} - q_x(-H)\frac{\partial H}{\partial x} - q_x(h)\frac{\partial h}{\partial x} + q_z(h) - q_z(-H) = 0 \tag{65}$$

The flow rate at the vertical direction controls the change of the water table and interface thickness:

$$q_z(h) = \frac{\varepsilon dh}{dt} \tag{66}$$

$$q_z(-H) = -\frac{\varepsilon dH}{dt} \tag{67}$$

where ε [-] is the porosity.

Substituting Darcy's law $q_x = -K\frac{\partial h}{\partial x}$ and the Ghyben-Herzberg relationship, $h = \delta H$, into Eq. (65) and applying the linearization method of the Boussinesq equation (Hantush, 1968; Bear, 2012), the governing equation is derived as:

$$\frac{K\delta\bar{H}}{\varepsilon}\frac{\partial^2 H^2}{\partial x^2} = \frac{\partial H^2}{\partial t} \tag{68}$$

where t [T] is the time; $\delta = (\rho_s - \rho_f)/\rho_f$; ρ_s [M/L^3] and ρ_f [M/L^3] are seawater and freshwater density, respectively; $\bar{H}$ [L] is the average of the areal distribution of the depth. Eq. (68) implies that the system can be approximated as a linear system of the squared lens thickness, H^2.

According to Dupuit assumption and the assumption that the hydraulic head along a vertical plane is the average value between the water table and interface, the discharge Q through a vertical plane can be written as (Fetter 1972; Bear, 2012; Rathore et al., 2020):

$$Q = -K(h + H)\frac{\partial H}{\partial x} \tag{69}$$

We can rearrange Eq. (69) as:

$$Q = -K(\delta + 1)\delta\frac{\partial H^2}{2\partial x} \tag{70}$$

At $x = 0,$ the interpretation of pumping point is analogous to Eq. (70). The only difference is that we consider the flow from both sides of the vertical plane. Thus, at the pumping point, we have a Neumann boundary (Hantush 1968):

$$\frac{\partial H^2(0,t)}{\partial x} = \frac{-q}{\delta(1+\delta)K} \tag{71}$$

where q [L^2/T] is the specific pumping rate.

The sea level is assumed constant:

$$H^2(W,t) = 0 \tag{72}$$

The transient-state solution can be derived for Eq. (68) given the average depth, which is not needed for the steady state. The steady-state solution of H^2 can be obtained as:

$$H^2(x) = \frac{-q}{\delta(1+\delta)K}(x - W) \tag{73}$$

Eq. (73) provides the solution to the interface profile subject to groundwater pumping. For the impact of recharge, the steady state solution of the lens interface under a recharge rate ω is given by (Fetter 1972):

$$H^2(x) = \frac{\omega(W^2 - x^2)}{\delta(1+\delta)K} \tag{74}$$

Since H^2 is approximated by a linear system, Eq. (68), we can obtain the steady-state interface profile under both pumping and recharge by superposing Eq. (73) and Eq. (74):

$$H^2(x) = \frac{\omega(W^2 - x^2)}{\delta(1+\delta)K} + \frac{q}{\delta(1+\delta)K}(x - W) \tag{75}$$

5.2.2 Critical Pumping Rate

The above approximate solution assumes that the pumping well is located at the surface, i.e., the upconing peak can reach the top at the critical pumping rate. Thus, by setting $H = 0$ at $x = 0$ in Eq. (75), we can get the critical pumping rate for the well at the top at the center of the island:

$$q_{\max} = \omega W \tag{76}$$

which indicates that the maximum or critical pumping rate for a well located at the aquifer top is half of the total recharge rate.

For a pumping well penetrating into the aquifer, the saltwater can be prevented from entering the well if the steady-state interface elevation in the pumping state is lower than the location of the well screen. Thus, the critical pumping rate can be determined by specifying the vertical distance from the well screen to the bottom of the pre-pumping lens as the maximum allowed interface elevation. This method was applied in previous studies to obtain the critical pumping rate for a partially-penetrating well (Chandler and McWhorter, 1975). For the analytical modeling approach, the critical pumping rate can be calculated directly by setting the left side of Eq. (75) equal to the squared well depth at $x = 0$, i.e., $H^2(x = 0) = d^2$. Thus, we obtain:

$$q_{\max} = \omega W - \frac{\delta(1+\delta)Kd^2}{W} \tag{77}$$

Eq. (77) includes the case of well at the surface by letting $d = 0$.

The analytical solution also enables us to generalize the problem with the following dimensionless variables:

$$H^* = \frac{H}{W}, \quad \omega^* = \frac{\omega}{K}, \quad \bar{H}^* = \frac{\bar{H}}{W}, \; t^* = \frac{Kt}{W\varepsilon}, \; x^* = \frac{x}{W}, d^* = \frac{d}{W}, \; q^* = \frac{q}{KW} \tag{78}$$

Eq. (75) and Eq. (77) can be written as:

$$H^{*2}(x^*) = \frac{\omega^*\left(1 - x^{*2}\right)}{\delta(1+\delta)} + \frac{q^*}{\delta(1+\delta)}(x^* - 1) \tag{79}$$

$$q^* = \omega^* - \delta(1+\delta){d^*}^2 \tag{80}$$

Eq. (80) indicates that the dimensionless critical pumping rate is controlled by two parameters, the dimensionless recharge rate and the well penetrating depth.

5.3 Conclusion

This study addresses a simple but important question for groundwater resources management in coastal islands: how much freshwater can be withdrawn from a fresh groundwater lens in island aquifers? We present an idealized conceptual model with a single pumping well located at the center of a two-dimensional vertical cross section of a small strip island. An explicit analytical solution is derived to determine the critical pumping rate for groundwater withdrawal at different well penetration depth. The analytical solution indicates that the critical pumping rate linearly increases with the recharge rate and linearly decreases with the hydraulic conductivity and the squared well penetrating depth.

There are several limitations with the derived solution and findings. In addition to the simplified hydrogeological settings, such as homogeneous thick aquifer, vertical section, and uniform recharge, etc., the critical pumping rate from the approximate analytical solution may not guarantee the pumped water is pure freshwater due to the sharp interface assumption. In particular, for islands with thick variable-density transitional zones, it may be necessary to use the breakthrough concentrations in the pumping well to determine the critical pumping rate. In addition, we only consider a single pumping well. In the practical field, multiple wells are commonly used for pumping. This leads to another interesting problem: given a certain number of pumping wells, how should the wells be placed and

what pumping rates should be assigned? This is a typical optimization problem for determining optimal pumping strategies in offshore coastal aquifers for maximizing the total pumping rate and preventing seawater intrusion. But this optimization problem has not been solved in island aquifers with the consideration of interface upconing. We shall notice that the optimization problems in offshore and island aquifers are different because only the interface toe position at the aquifer bottom needs to be considered in offshore aquifers and it is not an upconing problem. Moreover, given the lens conceptual model shown in Figure 1, if the number of wells is not limited, we may expect that theoretically all freshwater lens volume can be pumped through a series of wells with decreasing pumping rates from the lens center to the boundary. The research is underway to extend the current study of a single pumping well to the optimization of multiple wells in small islands. Nonetheless, our solutions and study provide very useful insights into the behavior of interface upconing and the impact of hydrogeologic conditions on critical pumping rates in small strip islands.

CHAPTER 6. EXPERIMENTAL VALIDATION

This chapter, we use laboratory visualization experiments to validate theoretical analysis of Chapter 3 to Chapter 5.

6.1 Impact of Time-dependent Variable Recharge

We apply our low-pass filter analysis in Chapter 3 to Stoeckl and Houben's (2012) lab. In the lab experiments conducted by Stoeckl and Houben (2012), the lens had a rapid response to recharge change. Their lens decayed to almost original zero level within just hundreds of minutes. It is much shorter than the periodic time in the example of St. George Island but caused obvious change of the lens. In their experiments, they applied the recharge ω_0 = 1.152 m/day for T_0 = 250 minutes and then turned it off. Figure 18 shows the spectrum of this aperiodic recharge using Fourier transformation. According to frequency analysis in 3.4, the system will reject components with the frequency larger than 0.1 and entirely pass those smaller than break frequency. This spectrum has peak-magnitude components smaller than break frequency 0.004 and a large range of components between the break frequency and 0.1. The former will pass through the system entirely and the latter will pass the system with reduction. Therefore, this changing recharge is able to cause the lens to vary. This explains the rapid response of the lens to the recharge change.

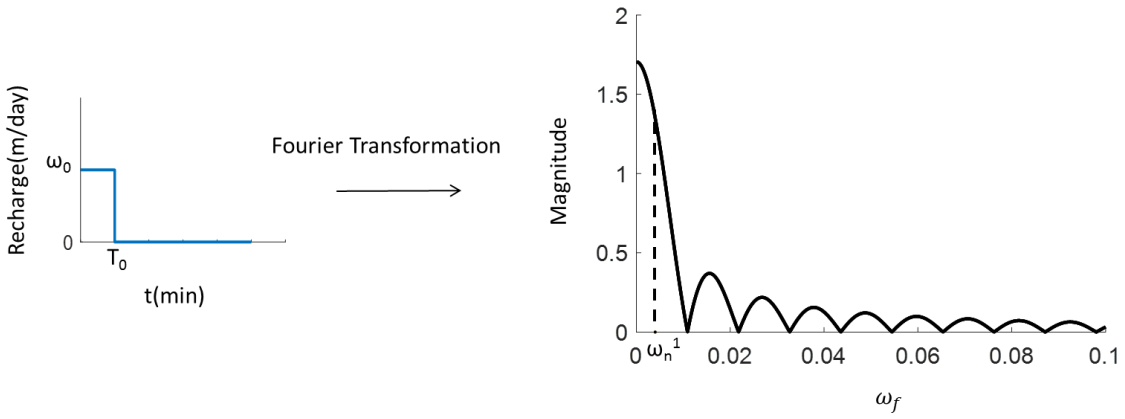

Figure 18. Recharge pattern in the lab experiment (Stoeckl and Houben, 2012) and corresponding spectrum with hydraulic conductivity 4.5×10^{-3} m/s, width 0.6m and porosity 0.39.

6.2 Impact of Spatially Variable Recharge

We conducted a laboratory experiment to verify the steady-state analytical solution of lens profile under spatially variable recharge in Chapter 4. In this experiment, an acrylic glass box of 60 cm length, 18 cm height and 1 cm width was used as a sand tank to simulate the cross-section of a strip island, with coarse sand filled to a height of 17 cm (Fig. 19(a)). The left and right reservoirs used to represent the seawater boundary were connected to the glass box through a 5 cm long channel and contained seawater with water level 15 cm above the tank bottom. Also, the two reservoirs were big enough to diminish seawater surface fluctuations and connected to each other to keep the water level equal for both sides. Surface recharge was supplied by a multi-channel peristaltic pump (Longerpump BT100-1L) through twelve freshwater dippers. The spatially variable recharge rate pattern was of Eq. (62): ω_1 = 0.2 cm/min, ω_2 = 0.6 cm/min, c = 30cm. The corresponding homogenous recharge rate is 0.4 cm/min over the whole domain. A density meter was used

to determine fresh and saline water densities, which were set to 998 and 1024.9 kg/m^3, respectively. The density meter also monitors the concentration of pumping water. A tracer dye was added to the saltwater for visualization, and the density was checked to ensure this led to no measurable change. All experiments were photographed at 10-minute intervals using a digital camera (Canon EOS 800D). (This part was conducted by Dr. Chunhui Lu's research group in Hohai University)

The comparison between laboratory and analytical solution is presented in Figure 19(b) and (c). The analytical solution matches well with experimental results despite some small difference near boundaries. This is mainly because experimental setup includes a freshwater outflow zone, which can generate a non-zero thickness of lens at the boundary.

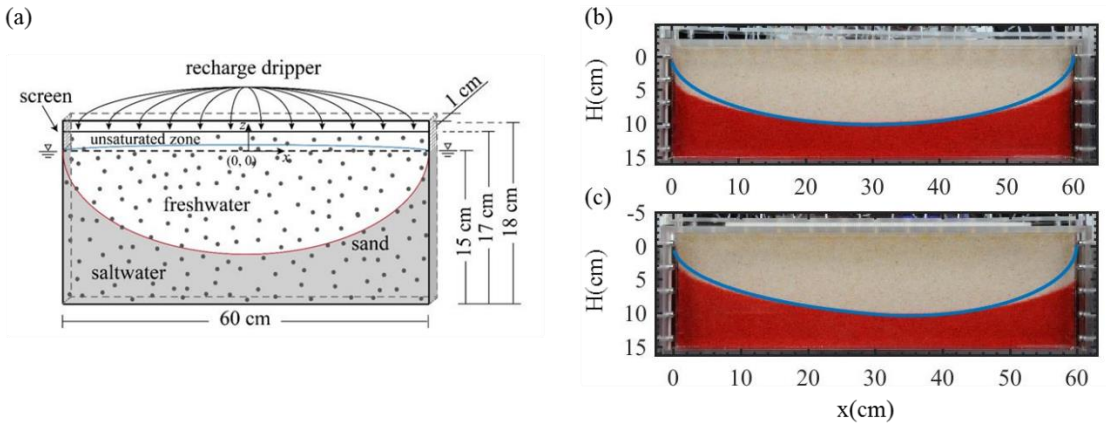

Figure 19. (a)Experimental Setup. (b) Comparison between laboratory and analytical solution for the homogeneous recharge of 0.4 cm/min over the whole domain. (c) spatially variable recharge pattern with recharge of 0.2 cm/min on the left half domain and 0.6 cm/min on the right half domain. Blue line is the analytical solution.

6.3 Critical Pumping Rate

We also conducted laboratory experiments to visualize the interface upconing in Chapter 5. Figure 20 shows the configuration parameters and real image of the experimental tank system. To avoid mixing between freshwater and saltwater, four drippers, at the rate of recharge rate, were arranged on each side to pump the mixture from the upper port. Surface recharge was supplied by a multi-channel peristaltic pump (Longerpump BT100-1L) through twelve freshwater dippers. Recharge rate were set to 0.12, 0.28, 0.56 cm/min, respectively, equal to 0.6, 1.4 and 2.8 mL/min per dipper. A stainless steel pipe with a diameter of 2 mm was inserted into the flow tank at the center to simulate the horizontal well, from the back to the front. The total length of the steel pipe was 2.5 cm, of which 1 cm was covered with small notches, and the rest was located outside the sandbox and connected to another peristaltic pump through a rubber tube at the back for well pumping. The steel pipe was placed at 0, 2.5 and 5 cm below sea level for different experiments. A density meter was used to determine fresh and saline water densities, which were set to 998 and 1024.9 kg/m^3, respectively. The density meter also monitors the concentration of pumping water. A tracer dye was added to the saltwater for visualization, and the density was checked to ensure this led to no measurable change. All experiments were photographed at 10-minute intervals using a digital camera (Canon EOS 800D).

Sands were filled uniformly in the tank. Several experiments were conducted in-situ to determine the hydraulic conductivity value. First, we keep the right side as inlet side of specified-flux Q, and the left side as an outlet side of specified-head h_{out}. After reaching the steady state, the head at the right side was recorded as h_{in}. Then, the K value can be calculated from:

$$K = \frac{4QW}{W_T(h_{in}^2 - h_{out}^2)} \tag{81}$$

where W and W_T are the half width and thickness of sand tank, equal to 30 cm and 1 cm respectively according to our experiment setup. Four sets of Q values were applied, and corresponding K values were estimated from the equation above. We adopted the arithmetic means, 200 cm/min, as the K value in both analytical solutions and numerical modelling. The porosity value was measured through the water saturation method (Fetter, 2018), and determined to be 0.38 (Yan et al., 2021).

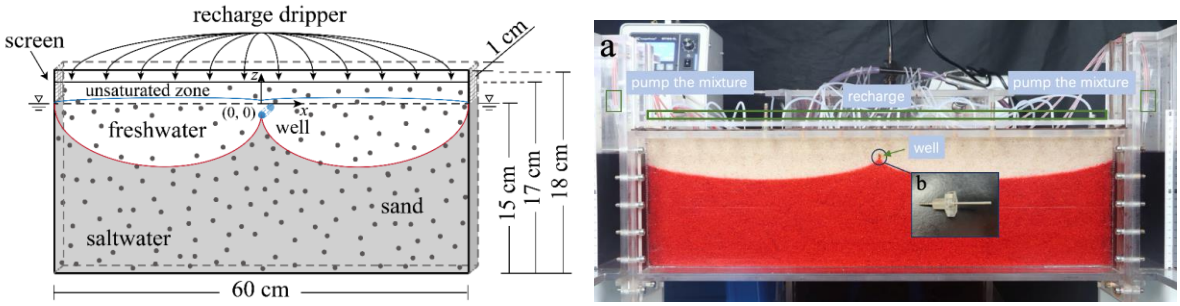

Figure 20**.** Sand tank configurations for laboratory visualization experiments.

Figure 21 compares the interface profiles given by Eq. (75) and the laboratory visualization experiments under the critical pumping rate determined by Eq. (77) for wells located at the tank top and partially penetrating into the tank media. Thin interfaces were created in the homogeneous sand (Abarca and Clement, 2009; Lu et al., 2013). All cases showed good agreement of interface profiles between experimental results and the approximate analytical solutions. We used three different recharge rates (Figures 21a – 21c) for the water withdrawal at the top of the tank. The volume of the freshwater lens or the interface thickness at the domain center increases with the recharge rate. Correspondingly, a higher water withdrawal rate can be achieved for a higher recharge rate. Given a constant recharge

rate, the total freshwater volume available for withdrawal is constant. However, the critical pumping rate decreases with the well penetration depth (Figures 21d – 21f), because the interface upconing peak is limited to the pumping depth.

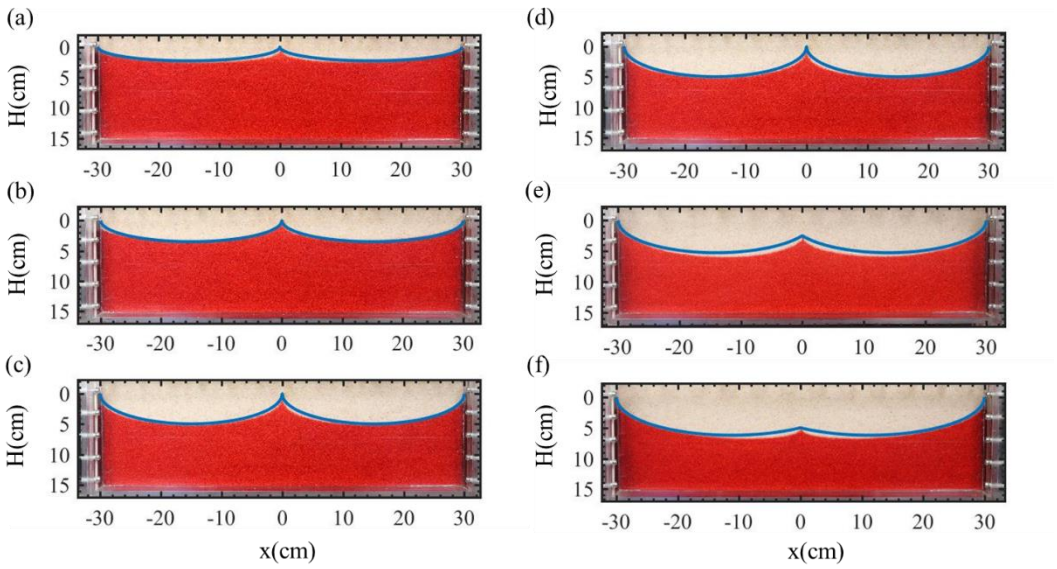

Figure 21. Comparison of steady-state interfaces between analytical solution and laboratory results under the critical pumping at the tank top for the recharge rate ω of (a) 0.12 cm/min, (b) 0.28 cm/min, and (c) 0.56 cm/min, and under the critical pumping rate for a constant recharge rate ω of 0.56 cm/min at the well depth d of (d) 0 cm, (e) 2.5 cm, and (f) 5 cm. The blue lines are analytical solutions. The hydraulic conductivity K is 200 cm/min. Half width W is 30cm.

CHAPTER 7. NUMERICAL INVESTIGATION

7.1 Impact of Time-dependent Variable Recharge

The approximate analytical solution from Chapter 3 is compared with a numerical model simulated by SEAWAT (Langevin et al., 2003), which couples variable-density flow and transport and requires to define diffusion and dispersion coefficients. The domain is divided into 600×150 grids with the fixed head on the two top corners. Each grid is of 1m×1m. The selection of 150m as height is to guarantee the domain in deep enough for lens development. Table 2 lists the domain geometric and hydrogeologic parameters (Bailey et al., 2013; Bailey et al., 2009; Ketabchi et al., 2014; Stoeckl and Houben, 2012), which are also used as the base case for numerical simulations in the next section.

Table 2. Hydrogeologic and geometric parameters used in the numerical model for validating the approximate analytical solution

Parameter	**Value**
Height	150 m
Width, $\boldsymbol{2W}$	600 m
Hydraulic conductivity, $\boldsymbol{K}$	10^{-3} m/s
Porosity, $\boldsymbol{\varepsilon}$	0.1
Dispersivity	1 m
Freshwater density	1000 kg/m^3
Seawater density	1025 kg/m^3

We simulate one recharge pattern consisted of five periods, shown in Figure 22(a). Each period is of 200 days. The approximate analytical solution is described by calculating the impulse response function, Eq. (26), and conducting the linear convolution, Eq. (25).

Numerical simulations yield a thin mixing zone due to small dispersion, which is not accounted for by the approximate analytical model. To address the discrepancy, researchers proposed to use the 50% concentration contour line in numerical simulation to represent the interface(Rathore et al., 2018; Reilly and Goodman, 1987). Figure 22(b) compares the groundwater lens 50% contour lines of numerical simulations and approximate analytical solutions. It clearly shows that the sharp interface predicted by the approximate analytical provides good approximation of the 50% concentration lines in numerical simulations. Their center thickness difference normalized by the numerical solution is 10.7%, 3.1%, 26%, 13.7% and 7% for these five subfigures. Although the approximate analytical solution may not provide accurate estimates of freshwater volume, if a high water quality threshold such as the normalized salinity less than 0.001 is adopted, it essentially characterizes the changing pattern of the lens profile, which can provide useful insights on the transient behavior of interface profile and lens volume in response to time-dependent recharge. In addition, we shall notice that numerical simulation of variable-density flow and transport is often computationally expensive, especially for a complex transient recharge pattern. For example, numerical modeling can only simulate discrete time-dependent recharge. When handling continuously changing recharge, numerical modeling needs to transform input to short discrete periods to approximate the continuous pattern, which makes the simulation cumbersome. However, both discrete and continuous, time-dependent recharge can be easily and fast implemented using analytical approach.

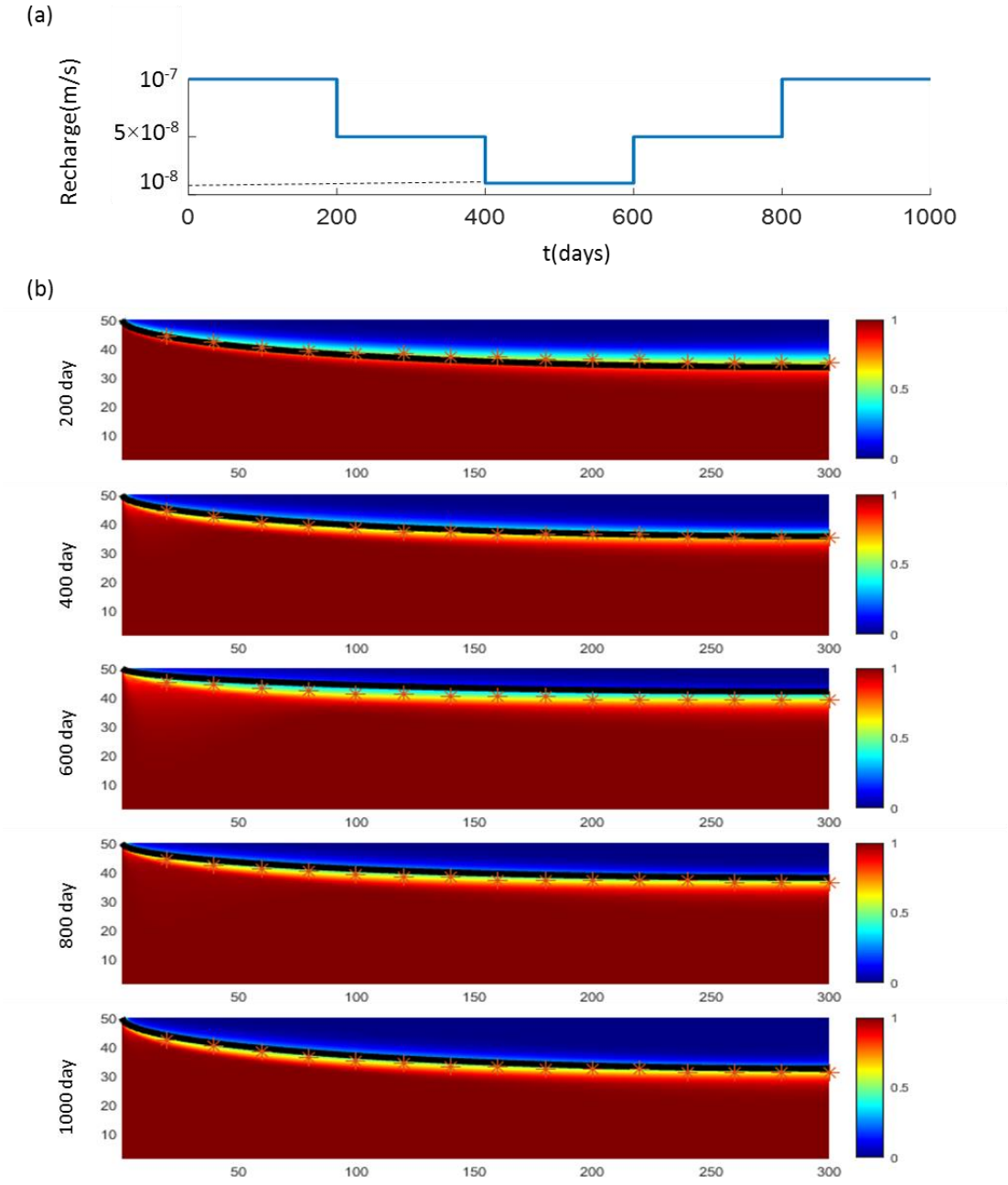

Figure 22. (a) Recharge pattern consisted of five periods. (b) Comparison of salinity distributions evaluated by numerical modeling and the sharp interface by the approximate analytical solution. The black solid lines are the approximate analytical solutions of interface. The red star is 50% concentration lines from numerical modeling. The color bar is from 0 to 1 representing the concentration from freshwater to seawater.

7.2 Impact of Spatially Variable Recharge

A numerical simulation was conducted by SEAWAT (Langevin et al., 2003) to validate both derived transient and steady analytical solution from Chapter 4. We simulated an island with an enhanced-recharge area at the domain center, which can be caused by a lake or an artificial recharge trench (Bouwer, 2002, Bouchez et al., 2016; Tu et al., 2011). Table 3 lists the typical hydrogeologic and geometric parameters (Alrashidi and Bailey, 2019; Chui and Terry, 2015; Ketabchi et al., 2014). This domain is 600 grid × 150 grid and the size of each grid is 1m×1m. Two top corners are set as fixed head. The domain height is 150m to guarantee the full development of lens and only 50m of domain is shown in Figure 23 and Figure 24 for a clearer presentation.

Figure 23 shows the comparison between numerical and transient analytical solution Eq. (46), and their center thickness difference normalized by the numerical solution is 4.7%, 1.3%, 2.3% and 4.4% for four subfigures in Figure 23. Figure 24 compares the steady solutions Eq. (52) with different recharge rates. Their center thickness difference normalized by the numerical solution is 7%, 7% and 5% for three subfigures in Figure 24. Numerical simulations produce thin transition zones between freshwater and seawater in numerical simulation due to dispersion. We also show the 50% concentration contour lines to compare with the analytical solution (Rathore et al., 2018; Reilly and Goodman, 1987). Both transient and steady-state cases demonstrate that the analytical solution provides excellent approximation of the transitional zone.

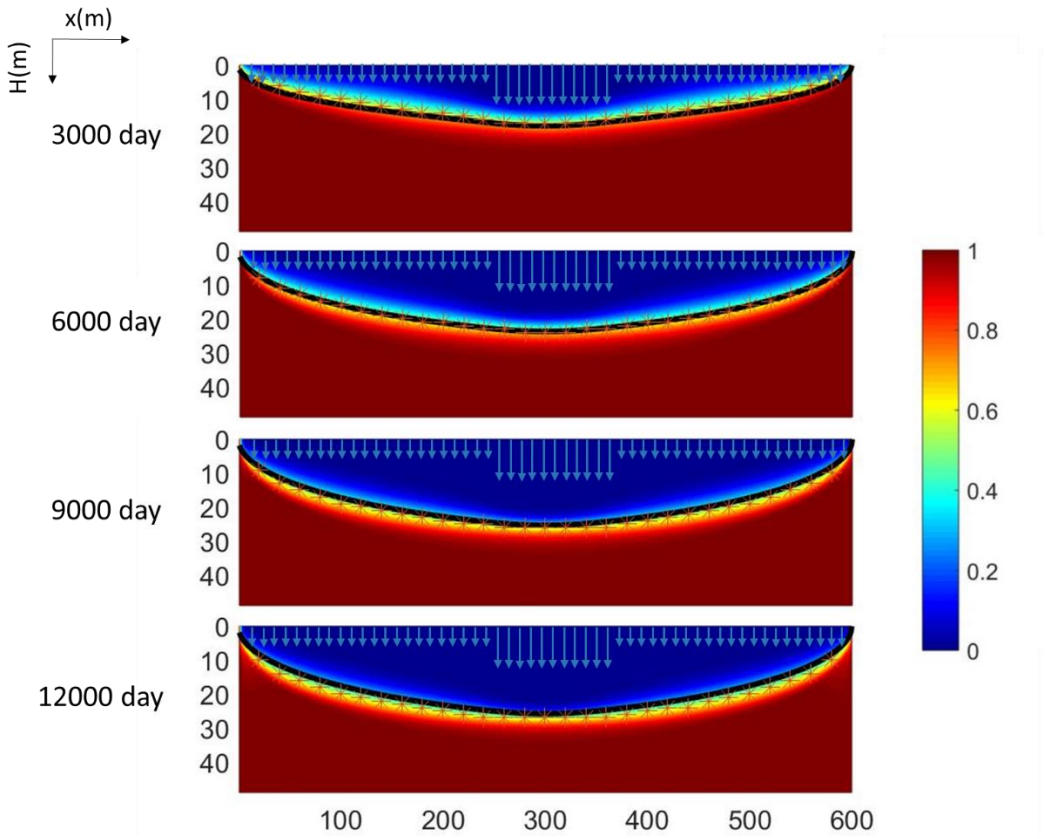

Figure 23. Comparison between numerical simulation and transient analytical solution. Black line is the analytical solution. Red star is the 50% concentration line of numerical simulation. The recharge is intensified over the center region of 100m. The color bar is from 0 to 1 representing the concentration from freshwater to seawater.

Table 3. Hydrogeologic and geometric parameters used in the numerical model for validating the analytical solution

Parameter	**Value**
Height	150 m
Width, $\boldsymbol{W}$	600 m
Recharge, **ω(x)** for figure 18	$\begin{cases}\omega_1 = 1\times10^{-8} m/s, & \text{x} < 250\text{m and x} > 350\text{m} \\ \omega_2 = 4\times10^{-8} m/s, & 250\text{m} \le \text{x} \le 350\text{m}\end{cases}$
Recharge, **ω(x)** for figure 19	$\begin{cases}\omega_1 = 1\times10^{-8} m/s, & \text{x} < 250\text{m and x} > 350\text{m} \\ \omega_2, & 250\text{m} \le \text{x} \le 350\text{m}\end{cases}$
(a)$\boldsymbol{\omega_2 = 2\times10^{-8} m/s}$	(b)$\omega_2 = 4\times10^{-8} m/s$ (c)$\omega_2 = 8\times10^{-8} m/s$
Hydraulic conductivity, $\boldsymbol{K}$	10^{-4} m/s
Porosity, $\boldsymbol{\varepsilon}$	0.3
Dispersivity	1 m
Freshwater density	1000 kg/m^3
Seawater density	1025 kg/m^3

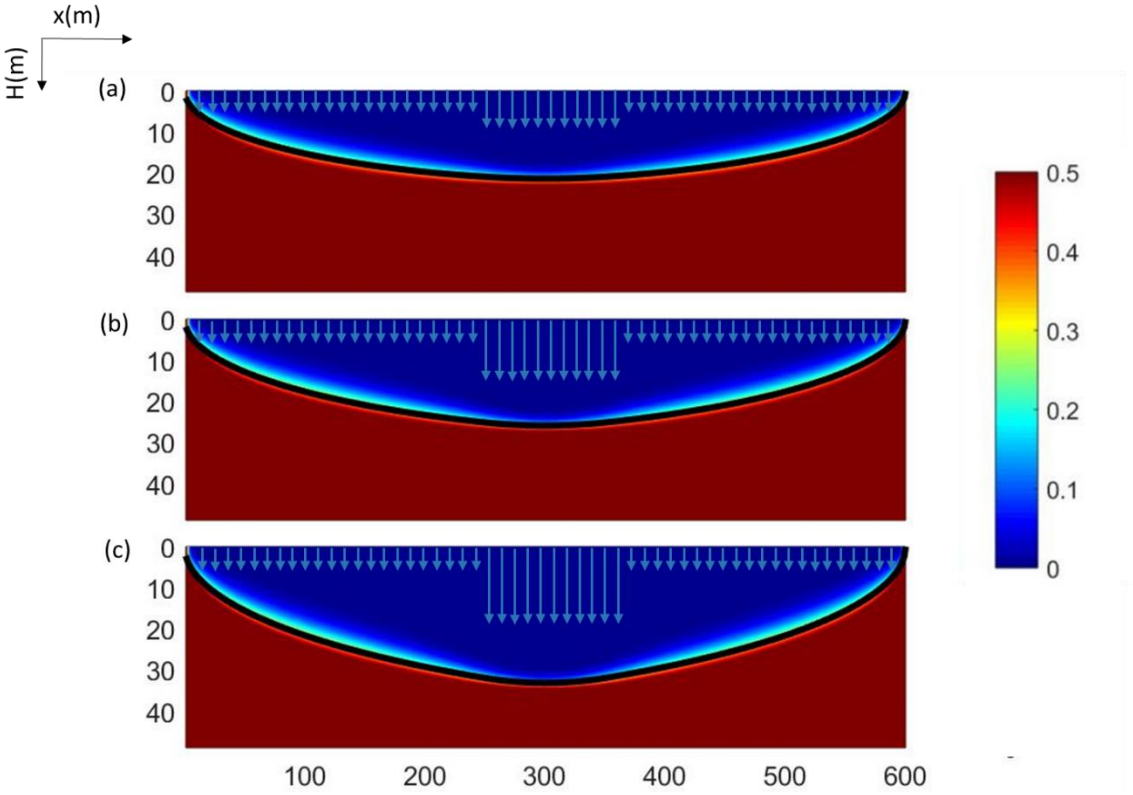

Figure 24. Comparison between numerical simulation and steady analytical solution. Black line is the analytical solution. The color-bar is from 0 to 0.5. The red edge along the transition zone is the 50% concentration line. The recharge over the center region becomes higher from (a) to (c). The color bar is from 0 to 1 representing the concentration from freshwater to seawater.

7.3 Critical Pumping Rate

7.3.1 Numerical Simulation

The approximate analytical solution from Chapter 5 is also validated by field-scale numerical cases simulated using SEAWAT (Langevin et al., 2003), which combines MODFLOW and MT3DMS to simulate variable-density flow. Table 4 lists typical

hydrogeologic and geometric parameters for a base field-scale numerical model. Recharge rates and well penetrating depths are varied to investigate the sensitivity. Each grid of the 600m×150m domain is 1m×1m. We compare the magnitude of critical pumping rates and the corresponding upconing interface profiles in the case of various recharge rates and well depths for numerical simulations and analytical solutions in the dimensionless form in the next section. We shall notice that it is not convenient to estimate the critical pumping rate by numerical modeling. Because the pumping rate needs to be predefined for numerical simulations, one can only try different pumping rates and visualize the concentration distributions or obtain the concentration profile at the pumping well to determine the maximum pumping rate that can maintain a stable interface without penetrating into the well. We use 1% as the salt concentration threshold to obtain the critical pumping rate in the numerical model. One may define other threshold values, which may yield similar behavior for thin lens interfaces.

Table 4. Hydrogeologic and geometric parameters used in the numerical model for validating the approximate analytical solution

Parameter	**Value**
Height	150 m
Width, $\boldsymbol{2W}$	600 m
Hydraulic conductivity, $\boldsymbol{K}$	10^{-4} m/s
Porosity, $\boldsymbol{\varepsilon}$	0.1
Longitudinal Dispersivity	0.01 m
Freshwater density	1000 kg/m^3
Seawater density	1025 kg/m^3

Figure 25(a) shows the field-scale numerical simulation results at the critical pumping rates for the recharge rate ω^* at 10^{-4}, 5×10^{-4}, and 10^{-3} for the pumping well located at the top of the aquifer. Symbols represent the contour lines of 1% salt concentration normalized by the seawater concentration for numerical simulations. The interface profiles given by the approximate analytical solution Eq. (79) match numerical simulations in all cases. The lens volume difference normalized by numerical simulation is 13.1%, 1.5% and 1.2% for three curves in Figure(a). In general, a higher recharge rate leads to a deeper interface, indicating a larger freshwater volume stored in the aquifer. Moreover, the upconing peak under the critical condition is located just below the well, implying a critical interface rise ratio of 1. The interface rise ratio is defined as the interface upconing height normalized by the distance between the well screen and the original lens profile. In infinite or semi-infinite horizontally flow domain without the vertical recharge, the critical rise ratio was found

around 0.25 to 0.9 (Bower et al., 1999; Motz, 1992; Werner et al., 2009). The difference is that the constant recharge of the lens from the top inhibits the upward movement of the interface and leads to a more stable interface than the cases with the recharge flow from side boundaries.

Figure 25(b) compares the analytical solution and 1% concentration contour lines in the numerical simulation for partially penetrating wells. The lens is assumed to be in a steady state before pumping. The critical pumping rate q^* is 8×10^{-4} and 5×10^{-4} for the dimensionless well depth d^* at 0.09 and 0.14, respectively. The critical pumping rate is reduced when the well penetrates deeper because a deeper well leads to a smaller allowed interface upconing. Figure 25 clearly shows that the analytical solution provides excellent approximation of the numerical solution for different recharge rates and penetrating wells. The lens volume difference normalized by numerical simulation is 3.9%, 3.5% and 2.6% for three curves in Figure(b).

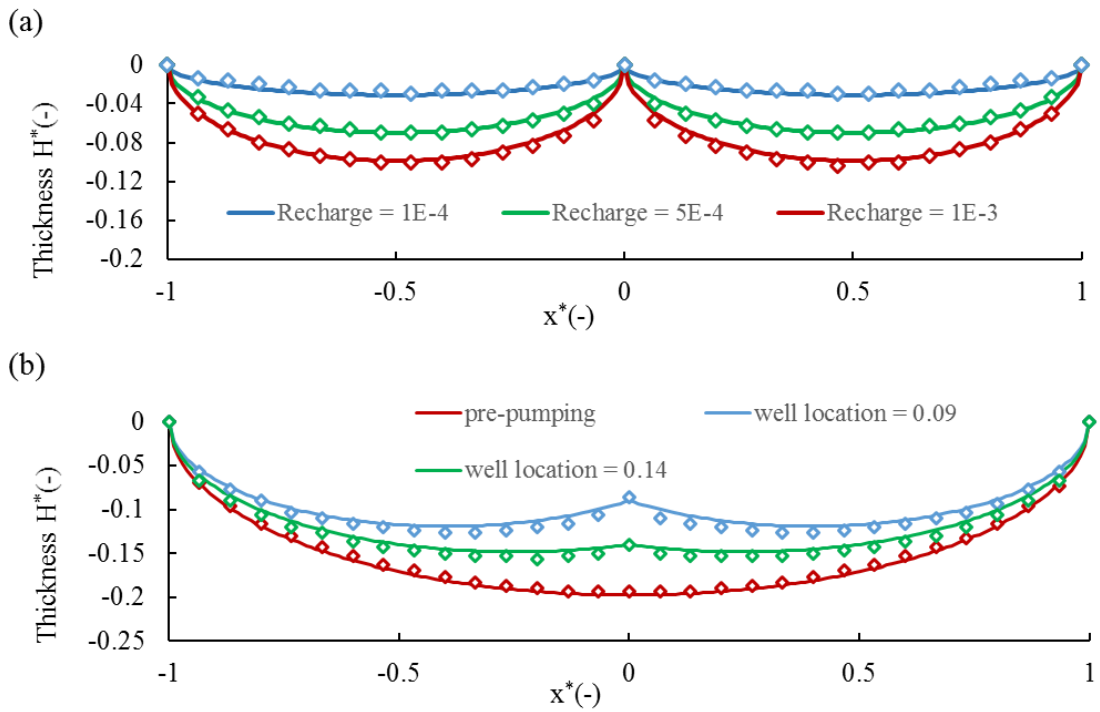

Figure 25. (a) Comparison of steady-state interfaces between analytical solution and 1% isochlor from the numerical simulation at the critical pumping rate for recharges ω^* of 10^{-4}, 5×10^{-4} and 10^{-3}. (b) Comparison between analytical solution and 1% concentration contour lines from the numerical simulation with a recharge rate ω^* of 10^{-3} and the steady-state interface under the critical pumping rate for dimensionless well depths d^* of 0.09 and 0.14. The dash lines are analytical solutions and symbols are numerical simulations.

7.3.2 Effects of Recharge Rate and Well Penetration Depth

Eqs. (77) and (80) provide simple first-order relationships between the critical pumping rate and hydrogeological and well parameters. That is, the critical pumping rate q^* linearly increases with the recharge rate and linearly decreases with the squared well penetration depth. Figure 26 shows that first-order relationship are well confirmed by the numerical simulations, especially at high recharge rates. The reason is that the salt concentration at

the pumping well is more likely to be affected by the transition zone between freshwater and seawater when the lens thickness becomes thinner under a lower recharge rate.

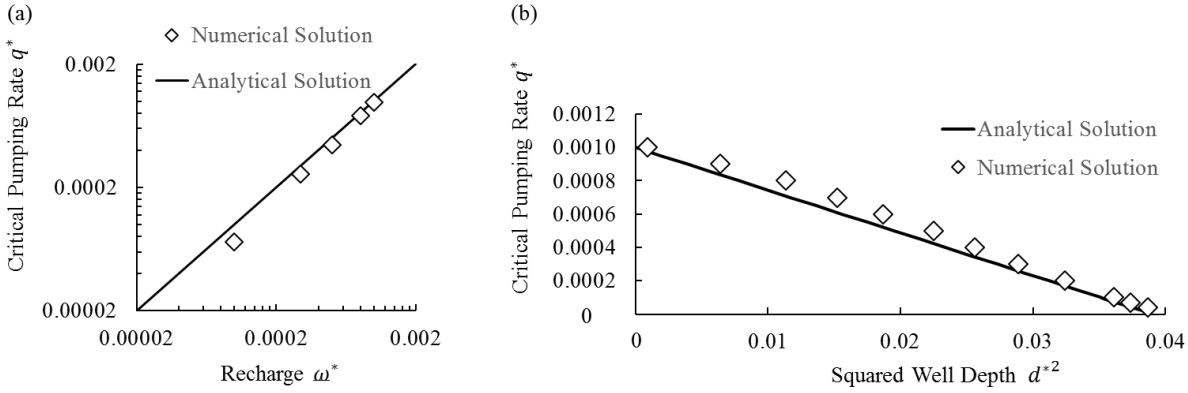

Figure 26. Sensitivity analysis of the critical pumping rate q^* in terms of the recharger rate ω^* and penetration depth d^*. (a) Linear relationship between q^* and ω^* for the pumping well located at the top, $d^* = 0$. (b) Linear relationship between q^* and squared well depth d^{*2} for the recharge rate ω^* of 10^{-3}.

7.3.3 Effects of Hydraulic Conductivity

Eq. (77) indicates that the critical pumping rate decreases linearly with the hydraulic conductivity. Thus, the recharge rate and hydraulic conductivity have opposite impact on the critical pumping rate. Such opposite impact was also observed in previous studies (Greskowiak et al., 2013; Ketabchi et al., 2014; Vacher, 1988). Another interesting observation given by Eq. (77) is that the critical pumping rate is independent of hydraulic conductivity if the pumping is applied at the aquifer top, i.e., $d = 0$. This case is common for a shallow well in a relatively thick groundwater lens. To verify this finding, we consider three cases for the well located at the top:

Case1: $\omega = 10^{-7}\frac{m}{s},\ K = 10^{-3}\frac{m}{s},\ \omega^* = 10^{-4}$

Case2: $\omega = 10^{-8}\frac{m}{s},\ K = 10^{-4}\frac{m}{s},\ \omega^* = 10^{-4}$

Case3: $\omega = 10^{-7}\frac{m}{s},\ K = 10^{-4}\frac{m}{s},\ \omega^* = 10^{-3}$

Eq. (79) shows that the lens interface under the critical pumping rate only depends on ω^*. This is verified by the interface profiles under the critical pumping rates shown in Figure 27, where Cases 1 and 2 have the same ω^* (from different combination of ω and K) and almost overlapped interface profiles, and Case 3 with a larger ω^* produces a thicker lens than Case 1 or Case 2's lens. It also demonstrates that using the ratio between recharge rate and hydraulic conductivity as the dimensionless form of ω^* is valid. Thus, Cases 1 and 2 have the same dimensionless critical pumping rate, q^*, which, as a result of the different recharge rate, yields the actual pumping rates with an order of magnitude difference. Moreover, Cases 1 and 3 have different hydraulic conductivity, i.e., 10^{-3} m/s and 10^{-4} m/s, but the same actually pumping rate in the numerical simulations, validating the conclusion from Eq. (77) that the magnitude of hydraulic conductivity has no impact on the actual critical pumping rate for a well located at the top.

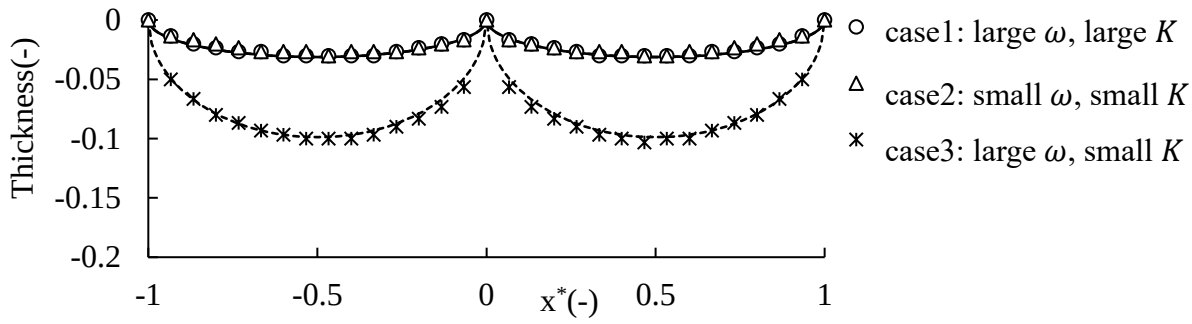

Figure 27. Effects of hydraulic conductivity on the critical pumping rate by analytical and numerical simulations. Comparison of steady-state interfaces between the analytical solution and 1% isochlor from the numerical simulation under the critical pumping rate. The dash lines are analytical solutions and symbols are numerical simulations.

CHAPTER 8. IMPACT OF LONG-TERM SEA LEVEL RISE AND PERIODIC TIDE ON FRESH GROUNDWATER LENS DEVELOPMENT

Due to climate change, the global sea level is rising faster than before, and it is predicted to continue to accelerate in the future (Chen et al., 2017; Nerem et al., 2018; Vu et al., 2018). Freshwater lenses in small islands face great threat because of the constantly rising sea level. A pure sea level rise without seawater intrusion or inundation has been proved to have slight influence on freshwater lens on small islands (Ketabchi et al., 2014). That is, if a two-dimensional vertical cross section of the aquifer is considered as the conceptual model, the increase of the sea level at the boundaries without intrusion into the inland has slight impact on the lens shape and volume. However, the freshwater lens volume can be significantly decreased once seawater intrusion occurs because the islands size is reduced under inundation and lens contained within the island's body shrinks greatly.

In the real field, the existence of low-lying areas, such as river channels or tidal creeks, leads to nonuniform coastal lines. In this chapter, we designed a strip island with a low-lying depression which is a typical topography in the coastal area of an island. In this type of terrain, rising sea levels can easily lead to seawater intrusion.

8.1 Conceptual Model

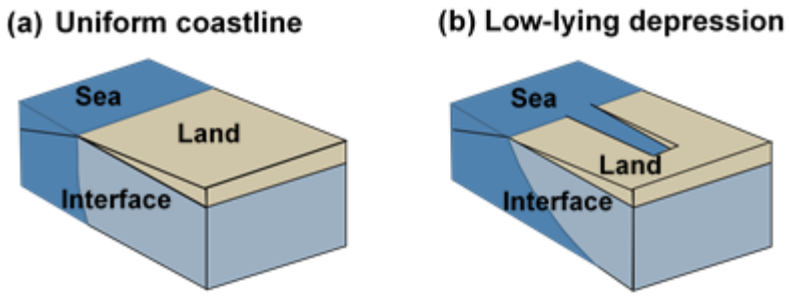

Figure 28. Simplified and idealized 3-D conceptual models of a strip island. (a) uniform coastline; (b) coastline with a low-lying depression encountering a sea level elevation.

Figure 28 shows the 3-D conceptual model for both uniform and nonuniform coastlines. The uniform coastline model can be simplified to a two-dimensional vertical cross section model. For the nonuniform model, the island is assumed symmetric with respect to the low-lying depression. The original sea level is lower than the elevation of the low-lying depression. In such a situation, there is no seawater intrusion for the whole island and thus the freshwater lens interface shown in the front cross section is constant along the coast, i.e., the nonuniform model can be simplified to the uniform model. However, a slight sea level rise can lead to seawater inundation into the low-lying depression, resulting in a decreasing freshwater volume stored in the island. In the following, we use numerical models to study two kinds of sea level rise: (1) long-term sea level rise, in which seawater enters the depression and stays for a long time; and (2) periodic tides, in which seawater enters and retreats in a periodic form with a short period.

8.2 Numerical Simulation: Base Case

8.2.1 Numerical Setting

The model is simulated by SEAWAT along with MODFLOW and MT3DMS, which describes the variable-density flow and solute transport. The size of the domain is 1000m×1000m×60m and the low lying depression is in the middle of the island with a size of 500m ×100m×9m, as shown in Figure 29 and Figure 30. The whole domain is uniformly discretized into grids of 10m×10m×3m. The head is set fixed along the coastal line to represent the sea level. A constant recharge is applied on the surface of the domain to serve as the freshwater supply of the lens. Original freshwater lens is firstly obtained with no seawater intrusion. We apply a higher sea level to the steady original freshwater lens, which cause seawater to invade the depression. The top surface of the depression is set as a constant seawater concentration boundary corresponding to the intruding seawater and the concentration boundary is off when seawater retreats.

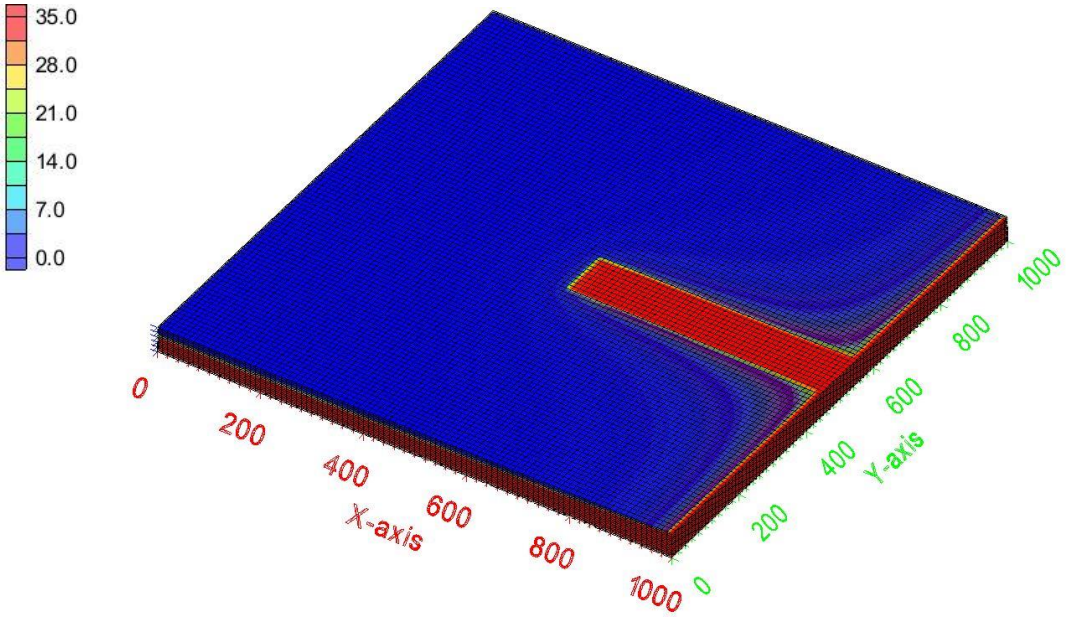

Figure 29. Oblique view of numerical simulation setup. The color bar is from 0 to 35 kg/m^3 salty concentration.

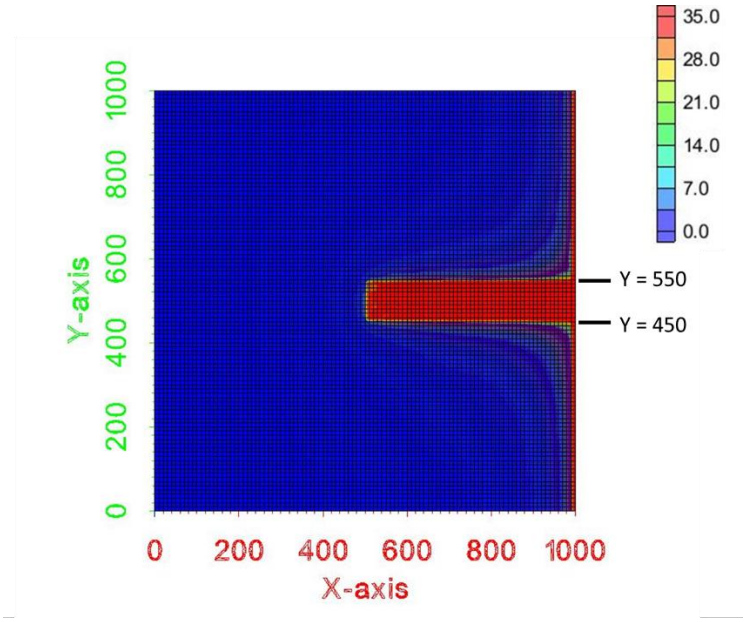

Figure 30. Top view of numerical simulation setup. The color bar is from 0 to 35 kg/m^3 salty concentration.

The geohydrological parameters for the base case of a long-term sea level rise and tides are summarized in Table 5. The tide cycle length is chosen as 14 days to represent spring tides and neap tides components. Under the 14-day cycle pattern, seawater is on the top of the depression for 7 days and away from the depression for the other 7 days.

Table 5. Hydrogeologic and geometric parameters used in the numerical model

Parameter	**Value**
Height	60 m
Width	1000 m
Length	1000 m
Recharge	10^{-8} m/s
Hydraulic conductivity, $\boldsymbol{K}$	10^{-3} m/s
Porosity, $\boldsymbol{\varepsilon}$	0.1
Dispersivity	1 m
Tide cycle length	14 day
Freshwater density	1000 kg/m^3
Seawater density	1025 kg/m^3

8.2.2 Comparison between the Long-term Sea Level Rise Case and Periodic Tide Case

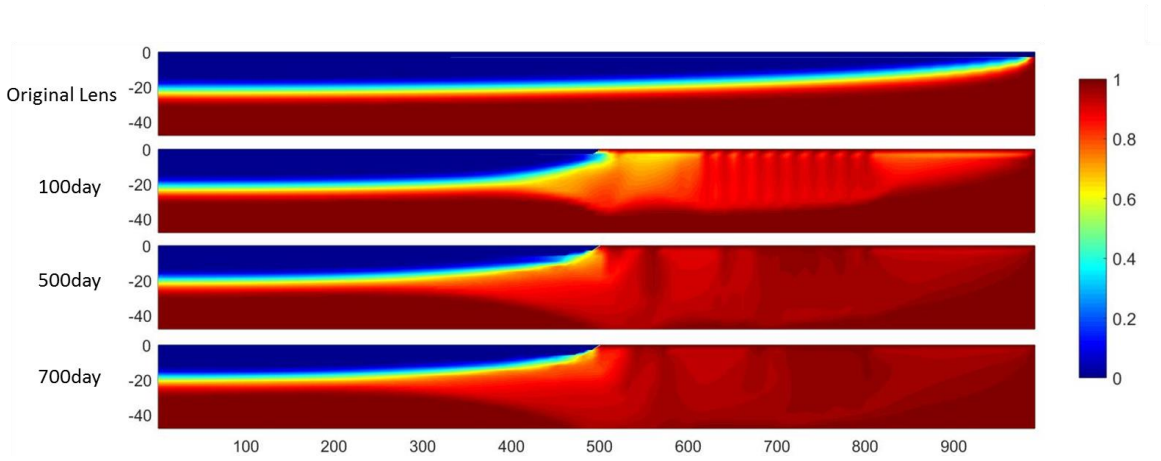

Figure 31. Cross section along y = 500m under a long-term sea level rise. The color bar is from 0 to 1 representing the concentration from freshwater to seawater.

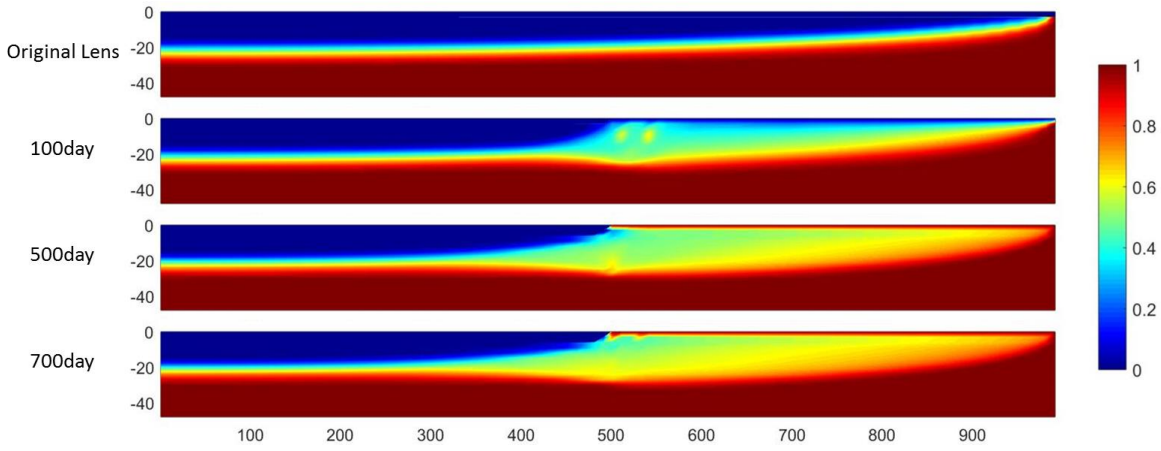

Figure 32.Cross section along y = 500m under a 14-day cycle length periodic tide. The color bar is from 0 to 1 representing the concentration from freshwater to seawater.

Figures 31 and 32 show the cross section along y = 500m (the middle line of the low-lying depression) under a long-term sea level rise and a 14-day periodic tide. Both lenses reach to the steady state at about 700 days. Steady lenses shrink to half length of the original size due to seawater intrusion. The salinity distribution under the depression is different for two

cases. For long-term sea level rise, the area is almost filled with seawater, and periodic tides cause the appearance of density fingers and thick mixing zones. The density fingers are commonly seen in Elder's problem where denser fluid on the top of light fluid provokes the occurrence of free convection. Our system is regarded as a mixed convection system which contains both hydraulic-conductivity-induced forced convection and density-difference-induced free convection (Ward et al., 2007). In our case of long-term sea level rise, forced convection dominants the system, thus eliminating the density fingers. The interesting thing is that the amount of potable freshwater is identical for two cases despite the difference of salinity distribution under the depression, i.e., thicker mixing zones. From the perspective of the amount of usable freshwater, these two cases can be considered equivalent. That is, periodic tides can be considered as static seawater intrusion because the lens decreases according to the farthest reachable point of seawater.

8.2.3 Influence Zone

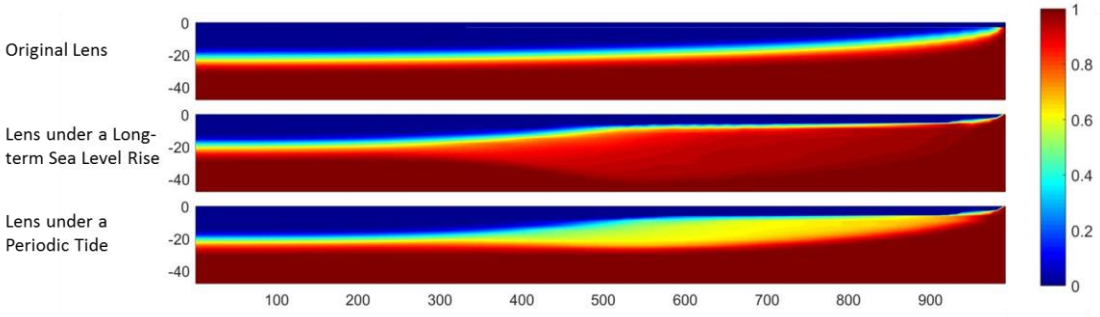

Figure 33. Cross section along y = 400m of the original lens, under a long-term sea level rise and under a 14-day cycle length periodic tide (steady state). The color bar is from 0 to 1 representing the concentration from freshwater to seawater.

The depression invaded by seawater not only affects freshwater lens directly under it but also affects nearby regions. We define the influence zone as the zone from the boundary of the depression to the point where freshwater lens volume is not affected. Figure 33 shows the cross section along y = 400m near the depression (from y = 450m to y = 550m) for two cases at late times. The lens volume under a sea level rise (long-term or periodic) is decreased compared with the original lens, indicating that the area of influence of sea level rise is larger than its own seawater intrusion area. Detailed discussion on the influence zone for different parameters will be presented in next part. Analogous to Figure 32, a long-term sea level rise and periodic tide have similar effects on the drinkable freshwater volume.

8.3 Sensitivity Analysis

8.3.1 Effect of Extent of Sea-level Rise

We plot the normalized freshwater lens volume of the cross sections from the depression to the domain boundary in Figure 34 to investigate the influence zone under different extent of sea level rise. The extent of sea level rise is indicated by the area of the seawater intrusion. L_s represents the distance that sea water enters the island and W_s represents the length of the coastal line submerged by seawater. L_s and W_s are normalized by the width of the domain 1000m. In Figure 34(a), L_s has significant effect on freshwater lens volume. When seawater intrudes half of the domain (L_s = 0.5), freshwater lens volume for cross sections along the inundated coastal line decreases to less than 50% of original volume. Moreover, when L_s = 0.4 and 0.5, the volume of the freshwater lens along the entire coastline decreases, indicating the influence zone of seawater intrusion covers the whole domain which is much larger than the area of seawater intrusion. Figure 34(b) shows how

the inundated coastal line (W_s) affects the influence zone. It clearly demonstrates that the increasing tendency of volume away from the depression keeps constant for varying length of inundated coastal line, indicating that the fixed-length (L_s) seawater intrusion has similar impact on the influence zone.

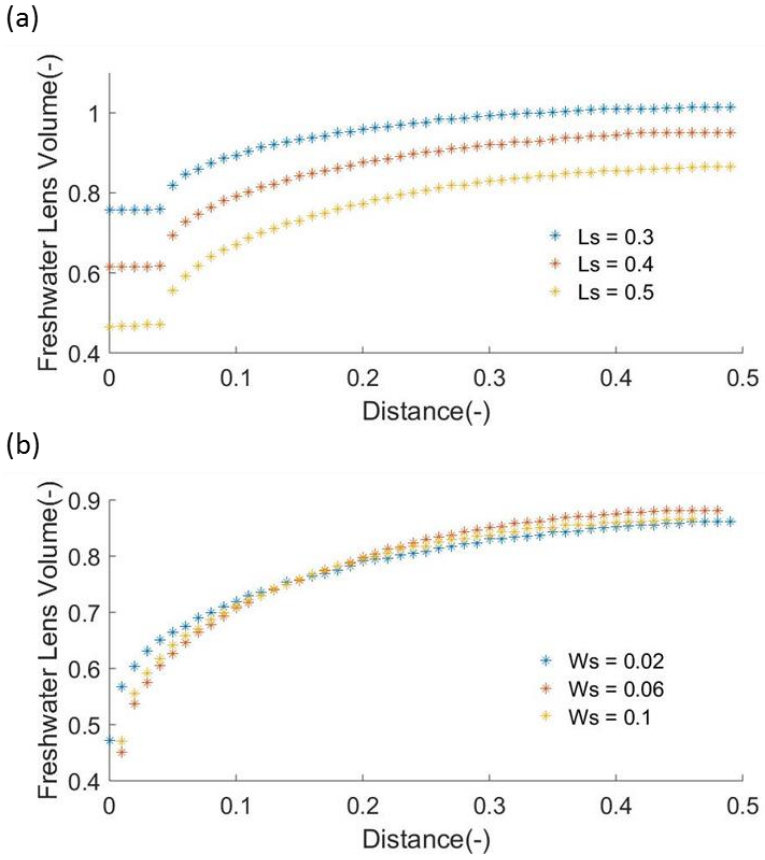

Figure 34. Freshwater lens volume normalized by the original unaffected lens volume along cross sections (a)from the center of the depression to the domain boundary for L_s of seawater intrusion area. W_s is fixed as 0.1; (b)from the edge of the depression to the domain boundary for different W_s of seawater intrusion area. L_s is fixed as 0.5. (L_s represents the distance that sea water enters the island and W_s represents the length of the coastal line submerged by seawater.)

8.3.2 Effect of Recharge and Hydraulic Conductivity

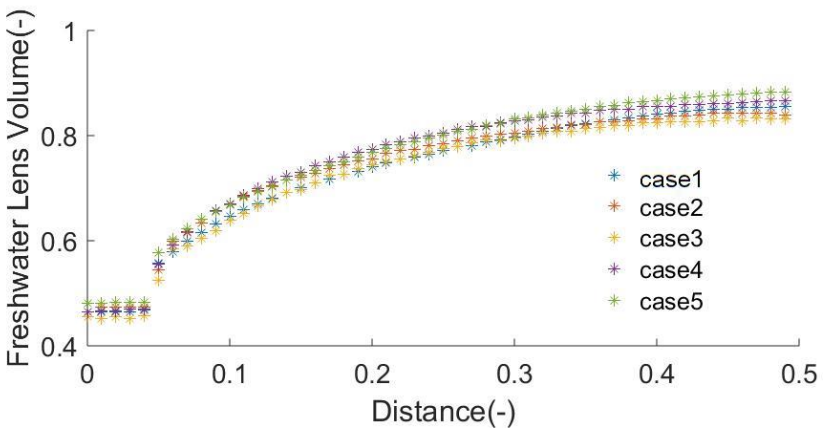

Figure 35. Freshwater lens volume normalized by the original unaffected lens volume along cross sections from the center of the depression to the domain boundary for different normalized recharge rates ω^*.

As the replenishment of freshwater lens, recharge is the most important one among numerous factors affecting freshwater lens on small islands. We investigate how islands of different recharge respond to seawater intrusion. Recharge rate and hydraulic conductivity have opposite effects on freshwater lens therefore here recharge rate is normalized by hydraulic conductivity to better represent the condition of the island. Figure 35 shows the proportion of the affected freshwater lens volume under seawater intrusion to the original unaffected volume remains constant for varying normalized recharge rates from different combinations of hydraulic conductivity and recharge rates in Table 6.

Table 6. Different combinations of hydraulic conductivity and recharge rate for Figure 35

	Normalized Recharge Rate	**Hydraulic Conductivity(m/day)**	**Recharge Rate(m/day)**
Case 1	5×10^{-5}	86.4	0.00432
Case 2	5×10^{-6}	8.64	0.0000432
Case 3	5×10^{-6}	86.4	0.000432
Case 4	10^{-5}	86.4	0.000864
Case 5	5×10^{-5}	8.64	0.000432

8.4 Extent of Influence Zone

From the sensitivity analysis, we can conclude that the intruding distance of sea water into the island, L_s, determines the impact of seawater intrusion. We simulate an entire island with a preferential flooding path of seawater intrusion from one side to investigate the relationship between the extent of influence zone and the intruding distance, L_s. The extent of the influence zone is defined as the distance between the cross sections where the freshwater lens volume is 95% of the original volume. The extent of the influence zone and L_s are normalized by the width of the island. Figure 36 shows the extent of the influence zone along the coastline approximately linearly increases with L_s. According to the definition, the influence zone starts to increase when the intruding length is greater than about 0.05, represented by the x-intercept.

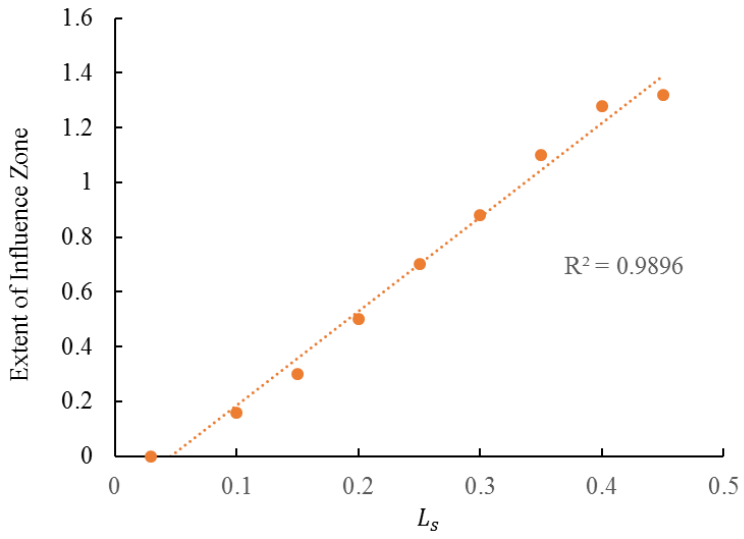

Figure 36. Relationship between the extent of influence zone along the coastal line and the intruding distance of seawater into the island through the low-lying depression, L_s.

8.5 Multiple Seawater Intrusion Path

Figure 37 shows the condition of the freshwater lens in a domain with two preferential intruding paths through low-lying 0.02 (20m)-width channels. We consider a dominant path with L_s = 0.5(500m) in the middle of the domain (y = 0.5). The other is less influential, far from the center and short in length. In Figure 36(a), the secondary path is of L_s = 0.3 at y = 0.1, 0.25 and 0.45, respectively, and in Figure 36(b), it is of L_s= 0.05, 0.3 and 0.5 at y = 0.4. Figure 37 shows that the secondary path has less impact on the freshwater lens when it is shorter or closer to the dominant one. We can only consider dominant path of seawater intrusion and ignore the short path (L_s = 0.5) or the path close to the dominant path (located in y= 0.45) in this specified case, which saves model time and improve efficiency.

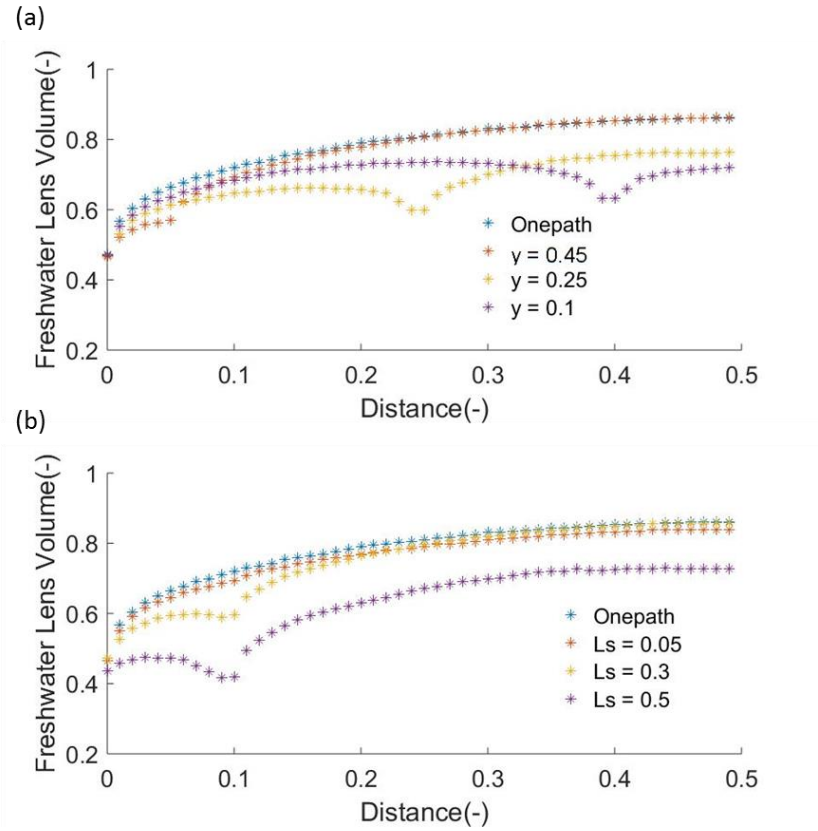

Figure 37. Normalized freshwater lens volume along cross sections from the center of the depression to the domain boundary with two 0.02(20m)-width paths of seawater intrusion. One is in the middle of the domain(y = 0.5) with L_s = 0.5. The other is (a)in y = 0.1, 0.25 and 0.45 with L_s = 0.3 (b) in y = 0.4 with L_s = 0.05, 0.3 and 0.5.

8.6 Conclusion

In this chapter, we designed a 3-D strip island model with a low-lying depression which allow a preferential path for seawater intrusion from a slight sea level rise. Two kinds of sea level rise are considered: long-term sea level rise and short-term periodic tides. Results show that these two kinds of sea level rise have similar impact on the freshwater volume within the lens, while there is a difference in salinity distribution for the two cases.

Seawater intrusion not only decreases the lens volume, but also influences nearby regions. The lateral extent of influence zone can be much larger than the seawater intrusion area though the preferential path. Sensitivity analysis shows that the length of the inundated coastal line, hydraulic conductivity and recharge rate have no influence on the ratio of the affected freshwater volume to the original amount while intruding distance into the land has a significant influence on the freshwater lens volume. We define the influence length and find that it is linearly dependent on the intruding distance through the preferential low-lying depression. Moreover, in our specified simulation, the dominant path of seawater intrusion is the most important while the short path (L_s = 0.05) and the path close to the dominant path (located in y= 0.45) can be ignored, which greatly enhances modeling efficiency. More systematic work is underway to quantify the importance of each seawater intrusion path.

CHAPTER 9. FIELD INVESTIGATION FOR ST. GEORGE ISLAND

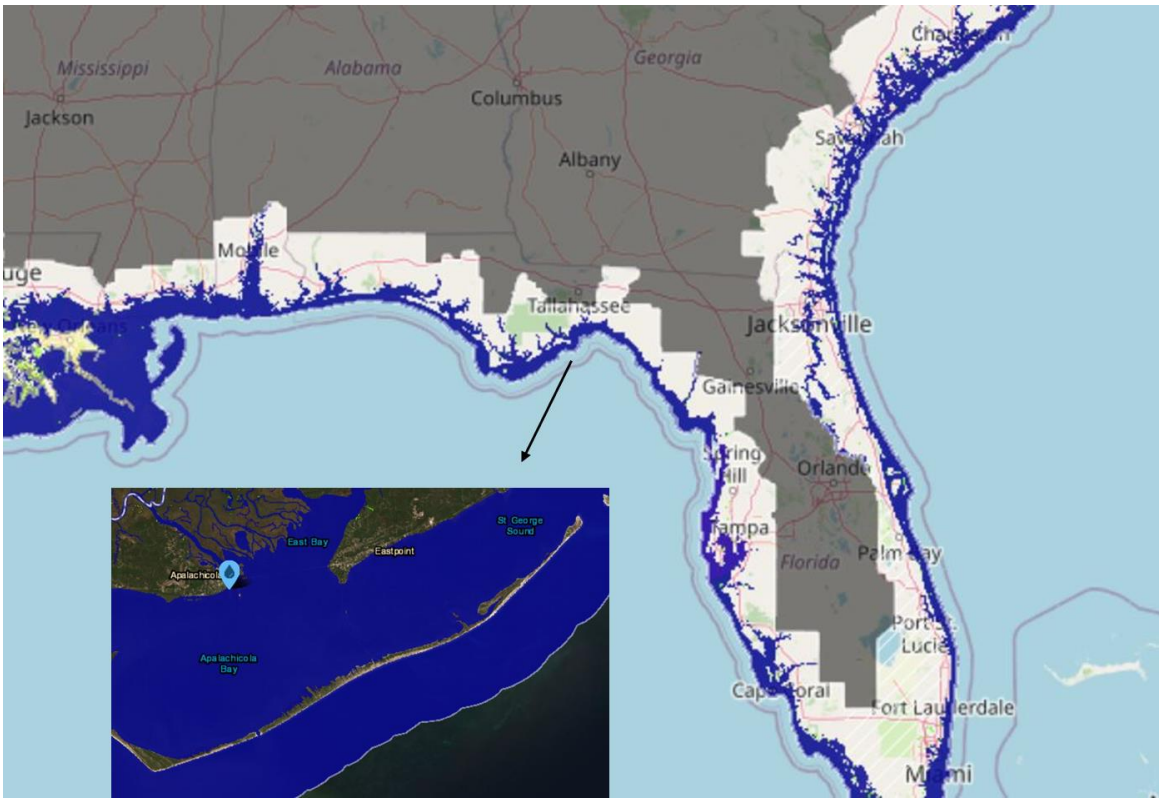

Figure 38. Map of St. George Island in Florida, USA. (All base maps in this chapter is from https://coast.noaa.gov/slr/#/layer/slr/0/-9451441.003877427/3459220.2081564707/14/satellite/none/0.8/2050/interHigh/midAccretion

St. George island is located in Florida, USA. It is of a strip shape e.g., its length is much longer than its width, as shown in Figure 38, which satisfies the 2-D assumption in our model. A 14km state park is located in the eastern island. Other parts of this island has been heavily developed, leading to a potential threat to local freshwater supply (Schneider and

Kruse, 2006). We apply our previous theoretical analysis to St. George island to investigate the impact of tine-dependent recharge, spatial variable recharge and sea-level rise on their freshwater lens development, and predict its potential available freshwater volume, which provides valuable insights into their freshwater management.

9.1 Impact of Time-dependent Recharge

The low-pass filter analysis based on the impulse response of the lens thickness is applied to analyze the field case reported for St. George (Schneider and Kruse, 2006). We calculated the monthly recharge (Recharge = Rainfall – Interception - Evapotranspiration) based on the method provided in their study. The average monthly rainfall (data is retrieved from Florida Climate Center from 1933 to 2014) was reduced to 85% to represent the effect of interception. Evapotranspiration is a fixed fraction of potential evapotranspiration computed from the Thornthwaite equation. Schneider and Kruse show the total potential evapotranspiration is 1m for one year. We distributed 1m to each month according to the relationship between monthly temperature (data is retrieved from Florida Climate Center from 1933 to 2014) and potential evapotranspiration in Thornthwaite equation. Figure 39a shows the average monthly recharge from 1933 to 2014.

We assume the recharge pattern is a yearly periodic function, i.e., the monthly pattern is constant for each year. The spectrum of the recharge rate is shown in Figure 39b. As discussed above, components with frequency higher than 0.1 will be rejected. Thus, except the average point, all other periodic components were blocked out. Therefore, the lens showed no fluctuation and remained almost constant as the average recharge profile. This analysis is consistent to the field investigation (Schneider and Kruse, 2006), in which it

was found that the groundwater lens had no response to significant seasonal recharge variations on St. George Island. The lens on this island remained constant for many years, and the short-cycle periodic recharge did not affect the lens. More realistically, rainfall varied each day and led to more frequent varying recharge inputs. However, the periodic components of such inputs were entirely rejected by the system. Thus, it is reasonable to use the average recharge rate to estimate the groundwater lens profile and volume. The time scale of changing recharge at this island is about at least ten years to cause obvious fluctuation of freshwater lens according to our estimation based on parameters of the island. Figure 39 (c) shows 10-year average annual precipitation from 1933 to 2016. It has minor fluctuations which can not lead to obvious fluctuation of lens thickness.

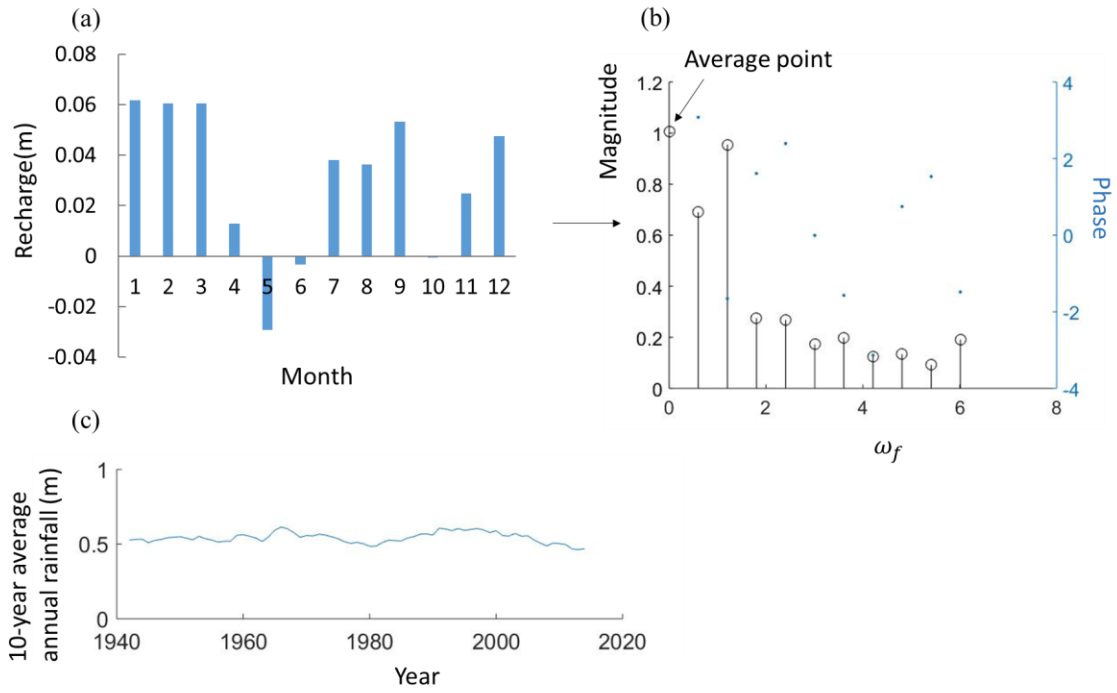

Figure 39. Recharge at St. George Island in Florida, USA (a) Average monthly recharge (1933 - 2014); (b) corresponding recharge spectrum with hydraulic conductivity 1.16×10^{-4} m/s, width 2000m and porosity 0.35; (c) 10-year average annual precipitation from 1933 to 2016.

9.2 Impact of Spatially Variable Recharge

The land use type in St. George island is variable. There is a 14km state park, which is consisted of mostly beaches and dunes, on the eastern part. A restoration project has been conducted in this state park by building vegetation census and transplanting species with high restoration potential (https://www.bio.fsu.edu/~miller/StGeorge/restoration_methods.htm). Central part in the St. George island has been heavily developed. Restaurant, bars and homes are densely distributed throughout this portion(Schneider and Kruse, 2006). Therefor recharge is

spatially variable on this whole island. Evaporation is enhanced on a highly vegetated area, leading to a reduction of recharge. In the following Figure 40(a), the recharge is spatially heterogeneously distributed along A-A and B-B cross section due to vegetated area on the north side. The vegetated area is about 40% of the extent of the island along A-A and 60% along B-B. We assume the average yearly recharge amount is 0.36m and the average yearly evaporation amount is 0.8m over the whole island. Thus, the area without vegetation recharge rate is of (0.36m+0.8m)/1 year = 1.16m/year and the vegetated area recharge rate is (1.16m×0.4-0.8m)/0.4/1 year= -0.84m/year along A-A cross section. Figure 40(b) shows the freshwater lens shape under the uniform recharge, and along A-A, B-B cross sections. It is obvious that the spatially heterogeneous recharge caused by the vegetated area leads to a reduction of lens volume under vegetated area, which results in a greatly asymmetry lens shape. In such a case, it is not accurate to use the average uniform recharge to estimate the freshwater lens interface and volume.

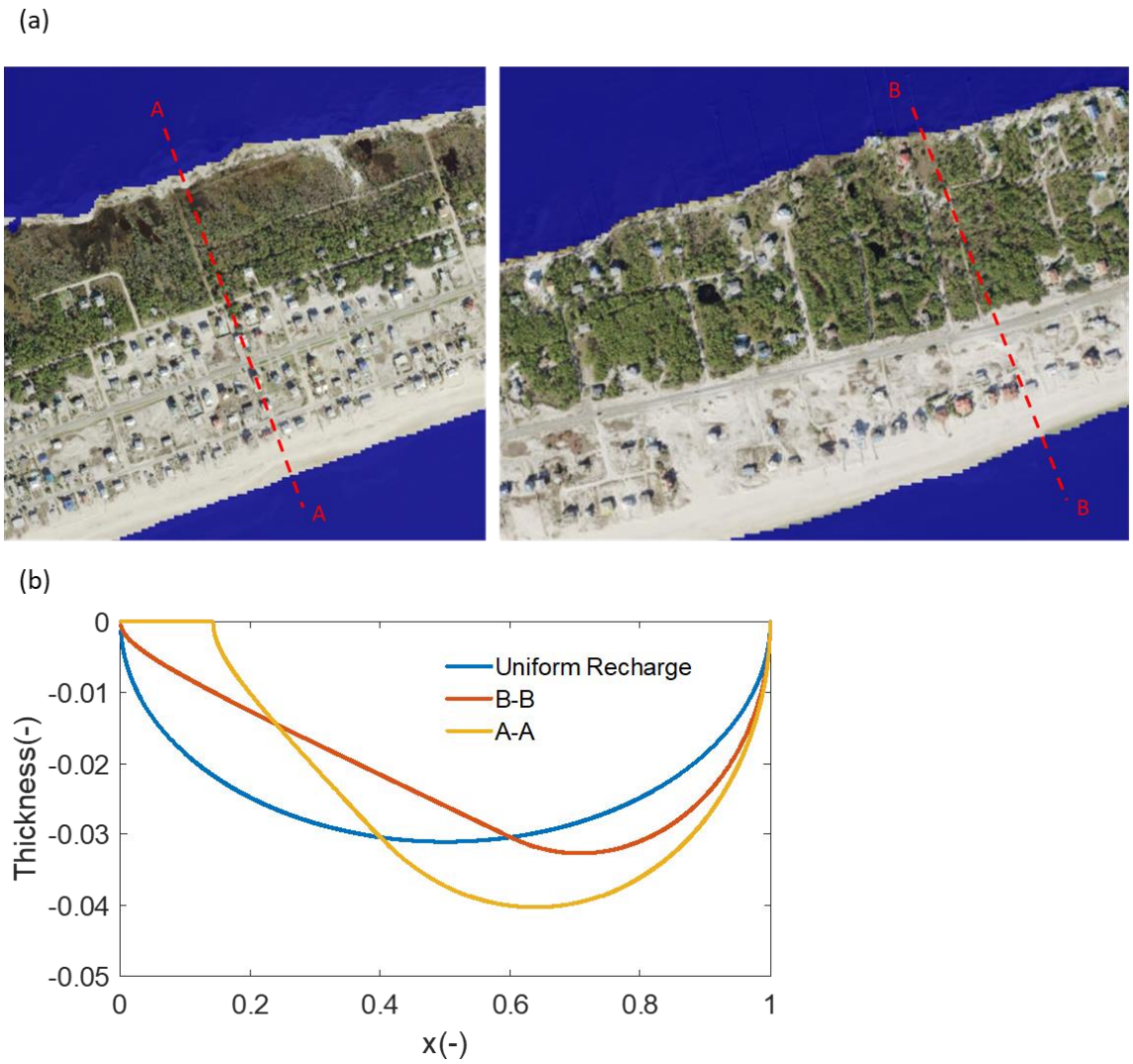

Figure 40. (a) Map of two cross sections with large vegetated areas in St. George island; (b) freshwater lens under uniform recharge and along A-A, B-B cross sections.

9.3 Freshwater Critical Pumping Volume in St. George Island

From Eq. (77) in Chapter 5, we found that the maximum pumping rate of a well located at the aquifer top is not affected by hydraulic conductivity and can theoretically reach 50% of the total recharge in our idealized model. That is, we can have the maximum pumping efficiency, 50% of the recharge amount, by installed shallow wells along the center line of

the freshwater lens, and a pumping rate greater than half of the recharge is not sustainable. One may use this information as simple guidance for groundwater withdrawal. For example, St. George island can extract about several millions of cubic meters of freshwater per year from the lens based on hydrogeological conditions and precipitation rates in the island. According to records, in 1998, residents on St. George island consumed about 0.6 million cubic meter freshwater(Schneider and Kruse, 2006), indicating the available freshwater resource is adequate for local island resident once they use proper pumping strategies, i.e., to use shallow wells and install wells at the center of the freshwater lens at a pumping rate lower than the critical value.

9.4 Sea-level Rise

As discussed in Chapter 8, a preferential path of seawater intrusion is more common than the inundation of the whole coastline. As shown in Figure 41, seawater has intruded into land through multiple paths. Seawater intrusion along each path can influence a large zone. According to our numerical model in Chapter 8, the hydraulic conductivity and recharge would not affect the percentage of reduced freshwater volume to the original volume. The percentage only depends on the ratio of the length of seawater intruding the island to the width of the whole land. The red circle in Figure 41 shows that seawater intrudes about one quarter of the width of the island. According to Figure 36, the extent of influence zone along the coastal line is 0.7 of the whole island width, as plotted as the yellow rectangle in Figure 41. Additionally, this single path of seawater intrusion can cause a reduction of the lens freshwater volume by approximately 10% under the influence zone.

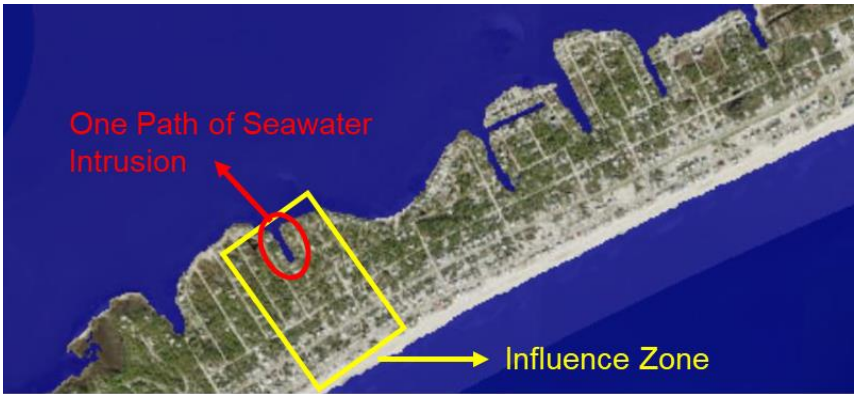

Figure 41. Map of one-path seawater intrusion and its influence zone in St. George island.

9.5 Summary

In summary, the freshwater lens in St. George island is resistant to the time-dependent recharge. It is reasonable to use the constant average recharge to estimate the lens behavior. However, the vegetated area on the north side of the island leads to a spatially heterogeneous recharge, which causes a greatly asymmetric interface of freshwater lens. Therefore, it cannot be represented by a spatially uniform recharge. The available freshwater volume in this island is about several millions cubic meter per year, which provides important guidance for local freshwater strategies designer. The major concern to St. George island is the seawater intrusion caused by sea-level rise. Instead of the inundation of the whole coastal line, single path of seawater intrusion is more common but still has a great influence.

CHAPTER 10. FUTURE WORK

10.1 Future Work

10.1.1 Freshwater-seawater Mixing Zone

We approximate the mixing zone between freshwater and seawater in freshwater lens as a sharp interface. This approach is valid when the extent of the mixing zone is thin compared with the thickness of the whole aquifer. More methods and tools are needed to evaluate how a wide mixing zone influences the lens behaviour.

10.1.2 Development of Freshwater Lens in Heterogeneous Aquifer

This thesis has studied the development of freshwater lens in a homogenous aquifer. Heterogenous aquifers would greatly influence the lens shape and volume in small islands. For example, a low-permeability zone can act as a barrier impeding the development of freshwater lens. It is critical to investigate how heterogeneity influences the behaviour of lens.

10.1.3 Optimization of Multiple Wells in Small Islands

Chapter 5 in this thesis studied the critical pumping rate of the single well in the small island. In the real field investigation, multiple well are applied to optimize the usage of freshwater from lens. The condition of multiple wells can be described by superposing Green function, Eq. (61), which can be considered as the freshwater-seawater interface under the pumping of a single well. The study of multiple wells is greatly complex

compared with the scenario of single well because we need to consider many parameters including the number of wells, the location of wells and pumping rates of wells.

10.1.4 Circular Small Islands

We assume the island is of a strip shape in this study. Circular shape is also a common geometry of real islands. The analytical solution can be extended to circular small islands. The difference is that circular small islands have different coordinate system in the analytical approach. The problem is still two dimensional.

10.1.5 Fully Bounded Rectangular Small Islands

Besides strip and circular geometry, rectangle small islands with fully bounded boundaries also deserve our attention. This geometry complicates the problem conceptualization by increasing the dimension to 3-D. The superposition is also complicated due to the exitances of four boundaries.

10.1.6 Effect of Nonlinearity

The development of lens thickness square is approximated by a linear system in our study. We used a constant $\bar{H}$ to represent the variable H in the governing equation to linearize the process. $\bar{H}$ is approximated as the areal average depth over a period. The linearity is valid in our current research scope. More examination is needed to validate the linearization if it is applied to fields with hydrogeologic parameters in wider ranges. For example, the sharp interface may not provide enough information of a large mixing zone caused by a high dispersion. In such a case, coupled flow and transport becomes nonlinear, and concentration distributions must be considered and specific concentration contour lines

may be defined to quantify the lens shape and volume. In addition, for multiple driving factors, we may use a dynamic linear system to describe the development of the lens profiles, i.e., the transfer function is not constant. Other possible approaches include the identification of different approximate linear terms, i.e., the lens thickness H (Bear, 2012).

10.1.7 Vertical Discharge in Freshwater Lens

Vertical discharge in freshwater lens cannot be ignored when dense seawater overlies light freshwater, which often occurs after storms or seawater level rise induced inundation. It triggers density-driven flow, which is involved in many natural and engineered hydrogeologic processes. Typical examples also include saltwater seepage from salt lakes, leachates with high contaminant concentrations from waste disposal sites and carbon sequestration in saline aquifers (Frind, 1982; Han et al., 2010; Huyakorn et al., 1987). Buoyancy forces arising in such fluid systems with density gradients can induce free convection and trigger gravitational instabilities as the form of fingers (Simmons, 2005), which travel much longer distances and faster than diffusive fluids. As a result, hydrodynamic mixing can be greatly time (Simmons, 2005; Simmons et al., 2001). To the best of our knowledge, there is no study on free convection in porous media caused by a limited-time dense solute source. In free-convection systems with a continuous source, plume fingers are triggered by hydraulic instabilities and then grow with time. As a result, steady states are rarely likely to reach in such systems in an open domain. Van et al., (2009) found three different long-term solutions for the classical Elder problem using a constant concentration boundary, indicating a highly unstable free convection system. By contrast, when the solute-loading is terminated for a limited-term source, fingering instability is expected to be reduced by spreading and dilution, potentially leading to a stable system at

late time. It remains unknown how the stable system develops from unstable fingering and how to characterize and quantify the system evolution behaviour and timescale. Below shows two different plume structures of steady state systems with a limit ed-term source:

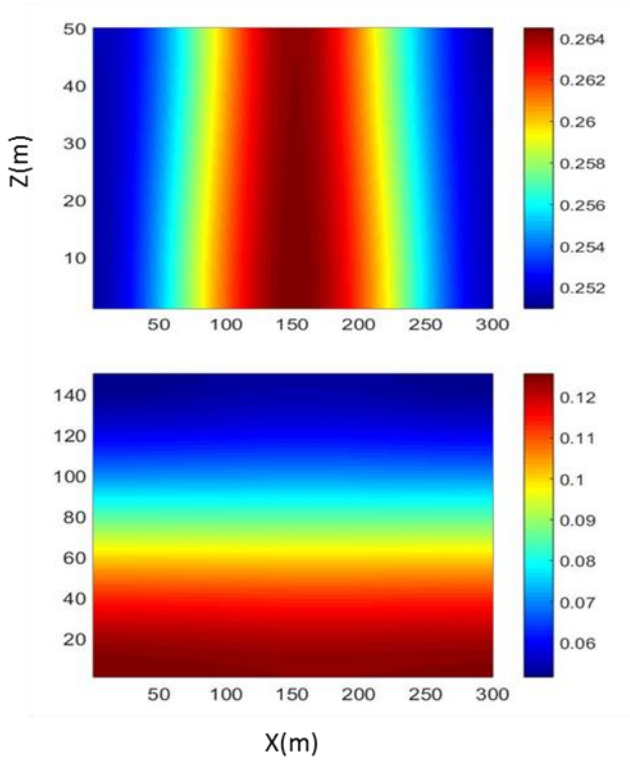

Figure 42. Steady-state plume structures of Elder problem with limited-term source. The color bar is from 0 to 1 representing the concentration from freshwater to seawater.

10.2 Conclusions

This thesis research investigated the development of freshwater lens under climate change in small islands using analytical solutions, numerical models and experiment work. The main conclusions include:

1. Numerical modeling shows the assumption of an average constant recharge rate may be valid for simulating groundwater lens profiles and volumes for transient recharge patterns with short periods such as daily rainfall. The mechanism is fundamentally demonstrated by frequency analysis. The development of freshwater lens under transient recharge can be fitted into a low-pass filter system on the frequency domain. Such a filter entirely passes sine-wave recharge components with frequency smaller than the break frequency, while attenuates those higher than the break frequency, yielding smoother fluctuations on lens thickness and volume than the recharge pattern.
2. A Green's function is derived based on the analytical solution to quantify the spatial effect of impulse recharge. For the steady-state lens profile corresponding to a constant point recharge, the recharge exerts the strongest influence on the squared lens thickness at the recharge location and decreases linearly away from the recharge location, resulting in a triangle function for the profile of squared lens thickness. Moreover, the point recharge at the domain center has the greatest influence over the whole domain than point recharge applied at other locations. The lens volume tends to have larger variances for recharge rates with higher variances and longer correlation lengths.
3. A simple formula of the critical pumping rate is provided as a function of hydrogeologic parameters, including the recharge rate, densities, hydraulic conductivity and well penetrating depth. It shows that the critical pumping rate increases linearly with the recharge rate and decreases linearly with the hydraulic conductivity and the squared well penetrating depth. Results indicate that the

maximum pumping rate can be as high as 50% of the total recharge for a well located at the top of the domain center, confirmed by our laboratory visualization experiments and numerical simulations.

4. Considering a preferential flooding path, long-term sea level rise and periodic tides have similar effect on the freshwater lens volume while there is a difference in salinity distribution for two cases. Seawater intrusion not only decreases the lens volume due to vertical migration, but also influence the aquifer along the coastline. The extent of influence zone can be much larger than the seawater intrusion area. The effect on the influence zone remains constant for seawater intrusions for islands with varying length of inundated coastal line and different recharge rate.

REFERENCES

Abarca, E. and Clement, T.P., 2009. A novel approach for characterizing the mixing zone of a saltwater wedge. Geophysical Research Letters, 36(6).

Abd-Elhamid, H., Javadi, A., 2011. Impact of sea level rise and over-pumping on seawater intrusion in coastal aquifers. Journal of Water and Climate Change, 2(1): 19-28.

Abdoulhalik, A., Ahmed, A.A., 2018. Transient investigation of saltwater upconing in laboratory-scale coastal aquifer. Estuarine, Coastal and Shelf Science, 214: 149-160.

Alrashidi, M.S., Bailey, R.T., 2019. Estimating groundwater recharge for a freshwater lens in an arid region: Formative and stability assessment. Hydrological Processes.

Alsumaiei, A.A., Bailey, R.T., 2018. Quantifying threats to groundwater resources in the R epublic of M aldives Part I: Future rainfall patterns and sea-level rise. Hydrological processes, 32(9): 1137-1153.

Asghar, M.N., Prathapar, S.A., Shafique, M., 2002. Extracting relatively-fresh groundwater from aquifers underlain by salty groundwater. Agricultural Water Management, 52(2): 119-137.

Ataie-Ashtiani, B., Werner, A.D., Simmons, C.T., Morgan, L.K., Lu, C., 2013. How important is the impact of land-surface inundation on seawater intrusion caused by sea-level rise? Hydrogeology Journal, 21(7): 1673-1677.

Bailey, R.T., Jenson, J., Olsen, A., 2009. Numerical modeling of atoll island hydrogeology. Groundwater, 47(2): 184-196.

Bailey, R., Jenson, J., Taboroši, D., 2013. Estimating the freshwater-lens thickness of atoll islands in the Federated States of Micronesia. Hydrogeology Journal, 21(2): 441-457.

Barkey, B.L., Bailey, R.T., 2017. Estimating the impact of drought on groundwater resources of the Marshall Islands. Water, 9(1): 41.

Bear, J., 2012. Hydraulics of groundwater. Courier Corporation.

Bedekar, V.S., Memari, S.S., Clement, T.P., 2019. Investigation of transient freshwater storage in island aquifers. Journal of contaminant hydrology, 221: 98-107.

Bergquist, M., Nilsson, A., Schultz, P., 2019. Experiencing a severe weather event increases concern about climate change. Frontiers in psychology, 10: 220.

Bouwer, H., 2002. Artificial recharge of groundwater: hydrogeology and engineering. Hydrogeology journal, 10(1): 121-142.

Bouchez, C. et al., 2016. Hydrological, chemical, and isotopic budgets of Lake Chad: a quantitative assessment of evaporation, transpiration and infiltration fluxes.

Bower, J., Motz, L., Durden, D., 1999. Analytical solution for determining the critical condition of saltwater upconing in a leaky artesian aquifer. Journal of Hydrology, 221(1-2): 43-54.

Bricker, S., Hughes, A., 2007. Impacts of climate change on small island hydrogeology—a literature review. British Geological Survey, Groundwater Science Programme Open Report OR/09/025.

Bryan, E., Meredith, K.T., Baker, A., Post, V.E., Andersen, M.S., 2016. Island groundwater resources, impacts of abstraction and a drying climate: Rottnest Island, Western Australia. Journal of Hydrology, 542: 704-718.

Campbell, J., Barnett, J., 2010. Climate change and small island states: power, knowledge and the South Pacific. Routledge.

Chandler, R., McWhorter, D., 1975. Upconing of the salt‐water‐fresh‐water interface beneath a pumping well. Groundwater, 13(4): 354-359.

Chen, X. et al., 2017. The increasing rate of global mean sea-level rise during 1993–2014. Nature Climate Change, 7(7): 492-495.

Chui, T.F.M., Terry, J.P., 2012. Modeling fresh water lens damage and recovery on atolls after storm-wave washover. Groundwater, 50(3): 412-420.

Chui, T.F.M., Terry, J.P., 2013. Influence of sea-level rise on freshwater lenses of different atoll island sizes and lens resilience to storm-induced salinization. Journal of Hydrology, 502: 18-26.

Chui, T.F.M., Terry, J.P., 2015. Groundwater salinisation on atoll islands after storm-surge flooding: modelling the influence of central topographic depressions. Water and Environment Journal, 29(3): 430-438.

Comte, J.C., Banton, O., Join, J.L., Cabioch, G., 2010. Evaluation of effective groundwater recharge of freshwater lens in small islands by the combined modeling of geoelectrical data and water heads. Water Resources Research, 46(6).

Dagan, G., Bear, J., 1968. Solving the problem of local interface upconing in a coastal aquifer by the method of small perturbations. Journal of hydraulic research, 6(1): 15-44.

Dagan, G., Zeitoun, D., 1998. Free-surface flow toward a well and interface upconing in stratified aquifers of random conductivity. Water resources research, 34(11): 3191-3196.

Dai, A., Zhao, T., Chen, J., 2018. Climate change and drought: A precipitation and evaporation perspective. Current Climate Change Reports, 4(3): 301-312.

Dose, E.J. et al., 2014. Experiments and modeling of freshwater lenses in layered aquifers: steady state interface geometry. Journal of hydrology, 509: 621-630.

FALKLAND, A., Custodio, E., 1991. Hydrology and water resources of small islands: a practical guide: a contribution to the International Hydrological Programme. Studies and reports in hydrology, 49: i-xiii.

Fetter Jr, C., 1972. Position of the saline water interface beneath oceanic islands. Water Resources Research, 8(5): 1307-1315.

Fetter, C.W., 2018. Applied hydrogeology. Waveland Press.

Florida Climate Center. https://climatecenter.fsu.edu/climate-data-access-tools/downloadable-data.

Frind, E.O., 1982. Simulation of long-term transient density-dependent transport in groundwater. Advances in water Resources, 5(2): 73-88.

Greskowiak, J., Röper, T., Post, V.E., 2013. Closed‐Form Approximations for Two‐Dimensional Groundwater Age Patterns in a Fresh Water Lens. Groundwater, 51(4): 629-634.

Guo, W., Langevin, C.D., 2002. User's guide to SEAWAT; a computer program for simulation of three-dimensional variable-density ground-water flow.

Haberman, R., 2003. Applied partial differential equations.

Han, W.S., Lee, S.Y., Lu, C., McPherson, B.J., 2010. Effects of permeability on CO2 trapping mechanisms and buoyancy‐driven CO2 migration in saline formations. Water Resources Research, 46(7).

Hantush, M.S., 1964. Hydraulics of wells. Advances in hydroscience, 1: 281-432.

Hantush, M.S., 1967. Growth and decay of groundwater-mounds in response to uniform percolation. Water Resources Research, 3(1): 227-234.

Hantush, M.S., 1968. Unsteady movement of fresh water in thick unconfined saline aquifers. Hydrological Sciences Journal, 13(2): 40-60.

Hsiang, S. et al., 2017. Estimating economic damage from climate change in the United States. Science, 356(6345): 1362-1369.

Huizer, S., Radermacher, M., De Vries, S., Oude Essink, G.H., Bierkens, M.F., 2018. Impact of coastal forcing and groundwater recharge on the growth of a fresh groundwater lens in a mega-scale beach nourishment. Hydrology and Earth System Sciences, 22(2): 1065-1080.

Huyakorn, P.S., Andersen, P.F., Mercer, J.W., White Jr, H.O., 1987. Saltwater intrusion in aquifers: Development and testing of a three‐dimensional finite element model. Water Resources Research, 23(2): 293-312.

Ketabchi, H., Mahmoodzadeh, D., Ataie-Ashtiani, B., Werner, A.D., Simmons, C.T., 2014. Sea-level rise impact on fresh groundwater lenses in two-layer small islands. Hydrological processes, 28(24): 5938-5953.

Langevin, C.D., Shoemaker, W.B., Guo, W., 2003. Modflow-2000, the US geological survey modular ground-water model--documentation of the SEAWAT-2000 version with the variable-density flow process (VDF) and the integrated MT3DMS transport process (IMT). 2331-1258.

Lu, C. et al., 2019. A proof-of-concept study of using a less permeable slice along the shoreline to increase fresh groundwater storage of oceanic islands: Analytical and experimental validation. Water Resources Research, 55(8): 6450-6463.

Lu, C., Kitanidis, P.K., Luo, J., 2009. Effects of kinetic mass transfer and transient flow conditions on widening mixing zones in coastal aquifers. Water Resources Research, 45(12).

Lu, C., Chen, Y., Zhang, C., & Luo, J., 2013. Steady-state freshwater–seawater mixing zone in stratified coastal aquifers. Journal of Hydrology, 505, 24-34.

Lu, C., Luo, J., 2014. Groundwater pumping in head-controlled coastal systems: The role of lateral boundaries in quantifying the interface toe location and maximum pumping rate. Journal of Hydrology, 512: 147-156.

Ma, T.S., Sophocleous, M., Yu, Y.-S., Buddemeier, R., 1997. Modeling saltwater upconing in a freshwater aquifer in south-central Kansas. Journal of Hydrology, 201(1-4): 120-137.

Masterson, J.P., Garabedian, S.P., 2007. Effects of sea‐level rise on ground water flow in a coastal aquifer system. Groundwater, 45(2): 209-217.

Motevalli, A., Moradi, H.R., Javadi, S., 2018. A Comprehensive evaluation of groundwater vulnerability to saltwater up-coning and sea water intrusion in a coastal aquifer (case study: Ghaemshahr-juybar aquifer). Journal of hydrology, 557: 753-773.

Motz, L.H., 1992. Salt-water upconing in an aquifer overlain by a leaky confining bed. Groundwater, 30(2): 192-198.

Mukherjee, S., Mishra, A., Trenberth, K.E., 2018. Climate change and drought: a perspective on drought indices. Current Climate Change Reports, 4(2): 145-163.

Muskat, M., 1938. The flow of homogeneous fluids through porous media. Soil Science, 46(2): 169.

Nerem, R.S. et al., 2018. Climate-change–driven accelerated sea-level rise detected in the altimeter era. Proceedings of the national academy of sciences, 115(9): 2022-2025.

Ohba, M., Sugimoto, S., 2019. Differences in climate change impacts between weather patterns: possible effects on spatial heterogeneous changes in future extreme rainfall. Climate Dynamics, 52(7): 4177-4191.

Oppenheim, A.V., Willsky, A.S., Nawab, S., 1996. Signals and Systems (Prentice-Hall signal processing series).

Oswald, S.E., Scheidegger, M.B., Kinzelbach, W., 2002. Time-dependent measurement of strongly density-dependent flow in a porous medium via nuclear magnetic resonance imaging. Transport in Porous Media, 47(2): 169-193.

Pelling, M., Uitto, J.I., 2001. Small island developing states: natural disaster vulnerability and global change. Global Environmental Change Part B: Environmental Hazards, 3(2): 49-62.

Post, V.E., Bosserelle, A.L., Galvis, S.C., Sinclair, P.J., Werner, A.D., 2018. On the resilience of small-island freshwater lenses: Evidence of the long-term impacts of groundwater abstraction on Bonriki Island, Kiribati. Journal of hydrology, 564: 133-148.

Post, V.E., Galvis, S.C., Sinclair, P.J., Werner, A.D., 2019. Evaluation of management scenarios for potable water supply using script-based numerical groundwater models of a freshwater lens. Journal of Hydrology, 571: 843-855.

Post, V.E., Houben, G.J., 2017. Density-driven vertical transport of saltwater through the freshwater lens on the island of Baltrum (Germany) following the 1962 storm flood. Journal of Hydrology, 551: 689-702.

Rathore, S.S., Zhao, Y., Lu, C., Luo, J., 2018. Defining the effect of stratification in coastal aquifers using a new parameter. Water Resources Research, 54(9): 5948-5957.

Rathore, S. S., Y. Tang, C. Lu, and J. Luo., 2020. A simplified equation of approximate interface profile in stratified coastal aquifers, Journal of Hydrology, 580, 124249.

Reilly, T., Goodman, A., 1987. Analysis of saltwater upconing beneath a pumping well. Journal of Hydrology, 89(3-4): 169-204.

Rubin, H., Pinder, G.F., 1977. Approximate analysis of upconing. Advances in Water Resources, 1(2): 97-101.

Schneider, J.C., Kruse, S.E., 2006. Assessing selected natural and anthropogenic impacts on freshwater lens morphology on small barrier Islands: Dog Island and St. George Island, Florida, USA. Hydrogeology journal, 14(1-2): 131-145.

Simmons, C.T., 2005. Variable density groundwater flow: From current challenges to future possibilities. Hydrogeology Journal, 13(1): 116-119.

Simmons, C.T., Fenstemaker, T.R., Sharp Jr, J.M., 2001. Variable-density groundwater flow and solute transport in heterogeneous porous media: approaches, resolutions and future challenges. Journal of contaminant hydrology, 52(1-4): 245-275.

Srikanthan, R., McMahon, T., 2001. Stochastic generation of annual, monthly and daily climate data: A review. Hydrology and Earth System Sciences Discussions, 5(4): 653-670.

Stoeckl, L., Houben, G., 2012. Flow dynamics and age stratification of freshwater lenses: Experiments and modeling. Journal of hydrology, 458: 9-15.

Stoeckl, L., Houben, G.J., Dose, E.J., 2015. Experiments and modeling of flow processes in freshwater lenses in layered island aquifers: Analysis of age stratification, travel times and interface propagation. Journal of Hydrology, 529: 159-168.

Stoeckl, L., Walther, M., Graf, T., 2016. A new numerical benchmark of a freshwater lens. Water Resources Research, 52(4): 2474-2489.

Strack, O., 1972. Some cases of interface flow towards drains. Journal of Engineering Mathematics, 6(2): 175-191.

Strack, O., 1976. A single‐potential solution for regional interface problems in coastal aquifers. Water Resources Research, 12(6): 1165-1174.

Sulzbacher, H. et al., 2012. Numerical modelling of climate change impacts on freshwater lenses on the North Sea Island of Borkum using hydrological and geophysical methods. Hydrology & Earth System Sciences, 16(10).

Tang, Y., Rathore, S.S., Lu, C., Luo, J., 2020. Development of groundwater lens for transient recharge in strip islands. Journal of Hydrology, 590: 125209.

Terry, J.P., Falkland, A.C., 2010. Responses of atoll freshwater lenses to storm-surge overwash in the Northern Cook Islands. Hydrogeology Journal, 18(3): 749-759.

Terry, J.P., Chui, T.F.M., 2012. Evaluating the fate of freshwater lenses on atoll islands after eustatic sea-level rise and cyclone-driven inundation: A modelling approach. Global and Planetary Change, 88: 76-84.

Tu, Y.-C., Ting, C.-S., Tsai, H.-T., Chen, J.-W., Lee, C.-H., 2011. Dynamic analysis of the infiltration rate of artificial recharge of groundwater: a case study of Wanglong Lake, Pingtung, Taiwan. Environmental Earth Sciences, 63(1): 77-85.

Vacher, H., 1988. Dupuit-Ghyben-Herzberg analysis of strip-island lenses. Geological Society of America Bulletin, 100(4): 580-591.

Van Reeuwijk, M., Mathias, S.A., Simmons, C.T., Ward, J.D., 2009. Insights from a pseudospectral approach to the Elder problem. Water Resources Research, 45(4).

Voss, C.I., Provost, A.M., 2002. SUTRA: A model for 2D or 3D saturated-unsaturated, variable-density ground-water flow with solute or energy transport.

Vu, D., Yamada, T., Ishidaira, H., 2018. Assessing the impact of sea level rise due to climate change on seawater intrusion in Mekong Delta, Vietnam. Water Science and Technology, 77(6): 1632-1639.

Ward, J.D., Simmons, C.T., Dillon, P.J., 2007. A theoretical analysis of mixed convection in aquifer storage and recovery: how important are density effects? Journal of Hydrology, 343(3-4): 169-186.

Werner, A.D., Jakovovic, D., Simmons, C.T., 2009. Experimental observations of saltwater up-coning. Journal of Hydrology, 373(1-2): 230-241.

Werner, A.D., Sharp, H.K., Galvis, S.C., Post, V.E., Sinclair, P., 2017. Hydrogeology and management of freshwater lenses on atoll islands: Review of current knowledge and research needs. Journal of Hydrology, 551: 819-844.

Werner, A.D., Simmons, C.T., 2009. Impact of sea‐level rise on sea water intrusion in coastal aquifers. Groundwater, 47(2): 197-204.

Wirojanagud, P., Charbeneau, R.J., 1985. Saltwater upconing in unconfined aquifers. Journal of Hydraulic Engineering, 111(3): 417-434.

Yan, M., Lu, C., Werner, A.D., Luo, J., Analytical, experimental and numerical investigation of partially penetrating barriers for expanding island freshwater lenses. Water Resources Research: e2020WR028386.

Zhang, H., Hocking, G., 1996. Withdrawal of layered fluid through a line sink in a porous medium. The ANZIAM Journal, 38(2): 240-254.

Zhang, H., Hocking, G.C., Seymour, B., 2009. Critical and supercritical withdrawal from a two-layer fluid through a line sink in a partially bounded aquifer. Advances in water resources, 32(12): 1703-1710.

Zhou, Q., Bear, J., Bensabat, J., 2005. Saltwater upconing and decay beneath a well pumping above an interface zone. Transport in Porous Media, 61(3): 337-363.